CONE PENETRATION TEST IN UNSATURATED SOIL WITH MATRIC SUCTION MEASUREMENTS

A Thesis Submitted to the College of

Graduate and Postdoctoral Studies

In Partial Fulfillment of the Requirements

For the Degree of Master of Science

In the Department of Civil, Geological and Environmental Engineering

University of Saskatchewan

Saskatoon

By

WONG, JONATHAN MAN-HEI

PERMISSION TO USE

In presenting this thesis/dissertation in partial fulfillment of the requirements for a Postgraduate degree from the University of Saskatchewan, I agree that the Libraries of this University may make it freely available for inspection. I further agree that permission for copying of this thesis/dissertation in any manner, in whole or in part, for scholarly purposes may be granted by Dr. Dave E. Elwood who supervised my thesis/dissertation work or, in their absence, by the Head of the Department or the Dean of the College in which my thesis work was done. It is understood that any copying or publication or use of this thesis/dissertation or parts thereof for financial gain shall not be allowed without my written permission. It is also understood that due recognition shall be given to me and to the University of Saskatchewan in any scholarly use which may be made of any material in my thesis/dissertation.

Requests for permission to copy or to make other uses of materials in this thesis/dissertation in whole or part should be addressed to:

Head of the Department of Civil, Geological and Environmental Engineering
University of Saskatchewan
57 Campus Drive
Saskatoon, Saskatchewan, Canada S7N 5B4
Canada

OR

Dean
College of Graduate and Postdoctoral Studies
University of Saskatchewan
Room 116 Thorvaldson Building
110 Science Place
Saskatoon, Saskatchewan, Canada S7N 5A2

ABSTRACT

This research consists of two main studies. In the first half of this dissertation, the research findings regarding the use of 3D scanner for shrinkage limit testing of soils are presented; the second half of this dissertation presents the findings related to the chamber tests conducted which measures the matric suction of the unsaturated soil during cone penetration tests.

Part I: Shrinkage curve Evaluation using a 3D scanner

A procedure is proposed for conducting shrinkage limit tests using a 3D scanner. Shrinkage limit tests were conducted on 13 different soils of various plasticity. Shrinkage curves for each material were obtained by curve fitting a shrinkage model to the measured dataset. Using linear regression analysis, an empirical correlation was developed to reasonably relate parameter c_{sh} from the shrinkage model to the ratio of the plastic and liquid limits. The shrinkage curves produced based on the model have an average difference of ~1.2% in terms of measured void ratio and predicted void ratio. The method was demonstrated to be robust for materials of low, medium, and high plasticity. The proposed methodology also presents a means of estimating a shrinkage curve in its entirety based solely on the volume of an air-dried sample, the specific gravity and Atterberg limits of the specimen. This effectively reduces the amount of work needed to derive the shrinkage curve and could potentially reduce the time for a shrinkage limit test by half or more.

Part II: Cone Penetration Testing in Unsaturated Silt with Matric Suction measurements

Most empirical correlations used to interpret cone penetration test (CPT) results have been developed from and for saturated soils, so the applicability of CPTs to unsaturated soils remains in question. This paper presents experimental results for CPTs conducted in a chamber instrumented with four rapid-response tensiometers and filled with an unsaturated silt: one test with silt at one water content and three tests with two layers of silt at different water contents (drier layer overlying the wetter layer). Two pore pressure dissipation (PPD) tests were conducted after 400 to 500 mm penetration in each layer. Negative pore-water pressures (matric suction) were monitored during advancement of the cone and the PPD tests; cone resistance, sleeve friction, and pore-water pressure were also recorded. CPT results indicate the built-in pore-water pressure transducer cannot provide useful information regarding pore pressure and hydraulic properties of the unsaturated soil. Hence, tensiometers ought to be used to obtain pore pressure measurements during and after penetration. Tensiometer readings can also be used to characterize the unsaturated soil in terms of the *in situ* soil water characteristic curve (SWCC), unsaturated hydraulic conductivity, *in situ* pore-water pressure profile, and *in situ* effective stress. Existing empirical correlations used to interpret the results of PPD tests and soil behaviour type (SBT) are reviewed. Using a spherical cavity expansion solution, a method is proposed to estimate the frictional parameters of the unsaturated silt.

ACKNOWLEDGEMENTS

First, I would like to express my sincere gratitude to my advisor Prof. Dave Elwood for the continuous support, the guidance and the tough love. Dr. Elwood grants the freedom to explore, but at the same time pointed me to the right direction when I am lost. Without his immense knowledge, his patience, and his almost-supernatural ability to cite literatures from memory, this thesis would not have been completed.

I would also like to extent my appreciation to the sponsors of this research: Dr. Delwyn Fredlund and ConeTec for their input and support.

My gratitude also goes to the encouragements and inputs from my academic committee, internal and external: Prof. Grant Ferguson, Prof. Chris Hawkes and Prof. Bing Si.

I thank my fellow “lab-rats”, Bryce Marcotte, Jacob Hartl, Haley Cunningham, Jon Osback and Minh Nguyen for the friendly chirps, the many coffee-runs, the jokes and the occasional liquid lunches we have had together in the past two and a half years. These memories and friendships are probably the only thing I will remember 10, 20 years from now.

I can never thank Mr. Adam Hammerlindl enough for his help. He is the MacGyver of our lab and the Mickey Goldmill to us lab rats. Without Adam giving me THE helping hand at time of frustrations; or inspiring me when I am at another hopeless dead end, this thesis could never have been written; nor will I be able to keep all 10 fingers. Thank you, Adam!

I also have to thank my family - my parents Simon and Evelyn and my partner-in-crime Sue-Len. Thank you for cheering me up during stressful days and putting up with my occasional nervous break-downs and temper tantrums. Your love for me is THE best thing that ever happened to me, I love you all.

TABLE OF CONTENTS

LIST OF FIGURES

LIST OF TABLES

Chapter 1. Introduction

1.1 Background

The Cone Penetration Test (CPT) is an in-situ testing method used to determine the geotechnical properties of soil. It is conducted by pushing an instrumented metallic cone into the ground at a fixed advancement rate (Figure 1- 1). The purpose of the CPT was to standardize soil testing in-situ and provide a degree of reliability not otherwise provided by the Standard Penetration Test (SPT).

During advancement, a tip load cell and friction sleeve load cell installed on the cone records the resistance of the soil parallel and perpendicular to the surface of the cone (termed “cone resistance” and “sleeve friction” respectively). Most cones are also equipped with a pore pressure transducer to monitor the pore-water pressure with depth as well. When the cone has advanced to the target depth, penetration is terminated to carry out a pore-water pressure dissipation (PPD) test. PPD test results are used to locate the in-situ water level within cohesionless soils; or to determine consolidation parameters of fine grained to cohesive soils.

Over the years, empirical equations have been developed to correlate the CPT soundings to some commonly used physical properties of soils, such as shear strength, friction angle and soil behaviour type, hydraulic conductivity, etc. These correlations allow geotechnical engineers to estimate the soil strength and soil type of the subsurface continuously with depth. However, CPT interpretations are only accurate if the soil is fully saturated for two major reasons:

Firstly, most empirical equations are developed based on recorded soil response of lab experiments and in-situ tests under saturated conditions. Hence, their applicability to unsaturated soils is unknown and requires a detailed investigation.

Secondly, to date, there are no attachments that will allow a piezocone to accurately measure negative pore-water pressure of unsaturated soils. Despite most pore pressure transducers being able to record vacuum pressure, the measurements are often inaccurate due to desaturation of porous stone (Campanella & Robertson, 1988). Unsaturated soils tend to cause porous stones to desaturate quickly after insertion due to hydraulic gradient.

Testing of unsaturated soils often involve the use of high-air-entry-value (HAEV) ceramics as a porous stone. A HAEV porous stone prevents intrusion of pore-air while allowing for free flow of pore-water. Tensiometers are water columns equipped with a vacuum pressure transducer and a HAEV porous stone. With the use of tensiometers, measuring pore pressure response during CPT test in unsaturated soils becomes possible.

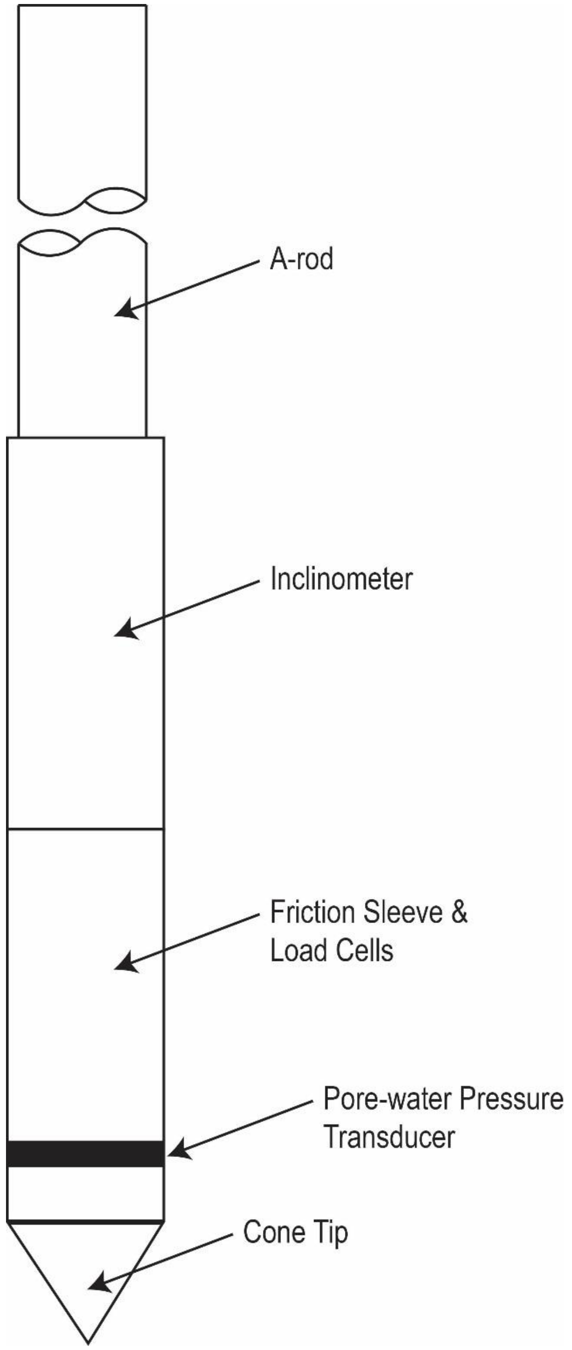

Figure 1- 1: Typical Schematic for Cone Penetrometers

1.2 Research Objective

The objective of this research is to extend the application of the CPT to unsaturated soils by, first, investigating the practicality of using tensiometers to measure pore pressure during a CPT sounding; second, examining the applicability of the existing empirical correlations using theories of unsaturated soil mechanics.

The experiments were conducted by advancing a piezocone with pore-water pressure measurements (CPTu) into a silt chamber, during which, cone resistance, sleeve friction and pore-water pressures were recorded. Four jet-fill type rapid-response tensiometers were installed inside the chamber to record the change of negative pore-water pressures (matric suction) during and after cone penetration. Once the piezocone reached the target depth, penetration was halted. Immediately thereafter, pore pressure dissipation (PPD) test was conducted.

The silt used in the chamber tests were characterized through series of saturated and unsaturated soil testing. The obtained parameters were compared to those estimated using CPT soundings from the chamber tests.

1.3 Scope of work

The research was conducted within the laboratory and consists of two parts. First, a physical characterization of the red silt used in the experiments was obtained. The characterization consisted the following evaluations:

- Unit weight;
- Specific Gravity;
- Grain Size Distribution;
- Soil-Water Characteristic Curve (SWCC);
- Shrinkage Curve;
- Consolidation Parameters (One-dimensional/ Isotropic);
- Hydraulic Conductivity (Saturated and Unsaturated); &
- Saturated and Unsaturated Shear Strength profile

Fredlund & Houston (2013) stated that since SWCCs did not account for volume change during sample desaturation, they ought to be coupled with a shrinkage test to obtain the true Air Entry Value (AEV).

In this research, shrinkage tests were conducted using a 3D scanner which utilizes LiDAR (Light Detection and Ranging) technology to generate 3D digital images of individual soil samples. This work was focused on developing an efficient method for determining the complete shrinkage curve, thereby streamlining laboratory shrinkage tests. Further research was also carried out to study the physical meaning of the curve fitting parameter c_{sh} of the shrinkage curve equation, as published in Fredlund et al. (2002). c_{sh} was determined for a wide range of soils with varying plasticities. The values of c_{sh} were plotted with respect to the plasticity of the soil to determine a representative equation to predict c_{sh} from standard Atterberg limits testing.

The second part of the research was carried out by performing a PPD test in an instrumented chamber that was filled with compacted red silt. As shown in Figure 1- 2 the chamber (1.5 m tall and 0.9 m diameter) was instrumented with 4 rapid response tensiometers. These tensiometers were installed at various depths to capture the matric suction generated around a cone. The chamber was filled with red silt with a specific water content by mass during each experiment. In total, the calibration chamber test was repeated five times at seven different water contents. A piezocone (NOVA cone), courtesy of ConeTec, was pushed into the chamber at an advancement rate of 2 centimeters per second (ASTM D-5778). The advancement was halted when the cone reaches the target depth to perform a PPD test.

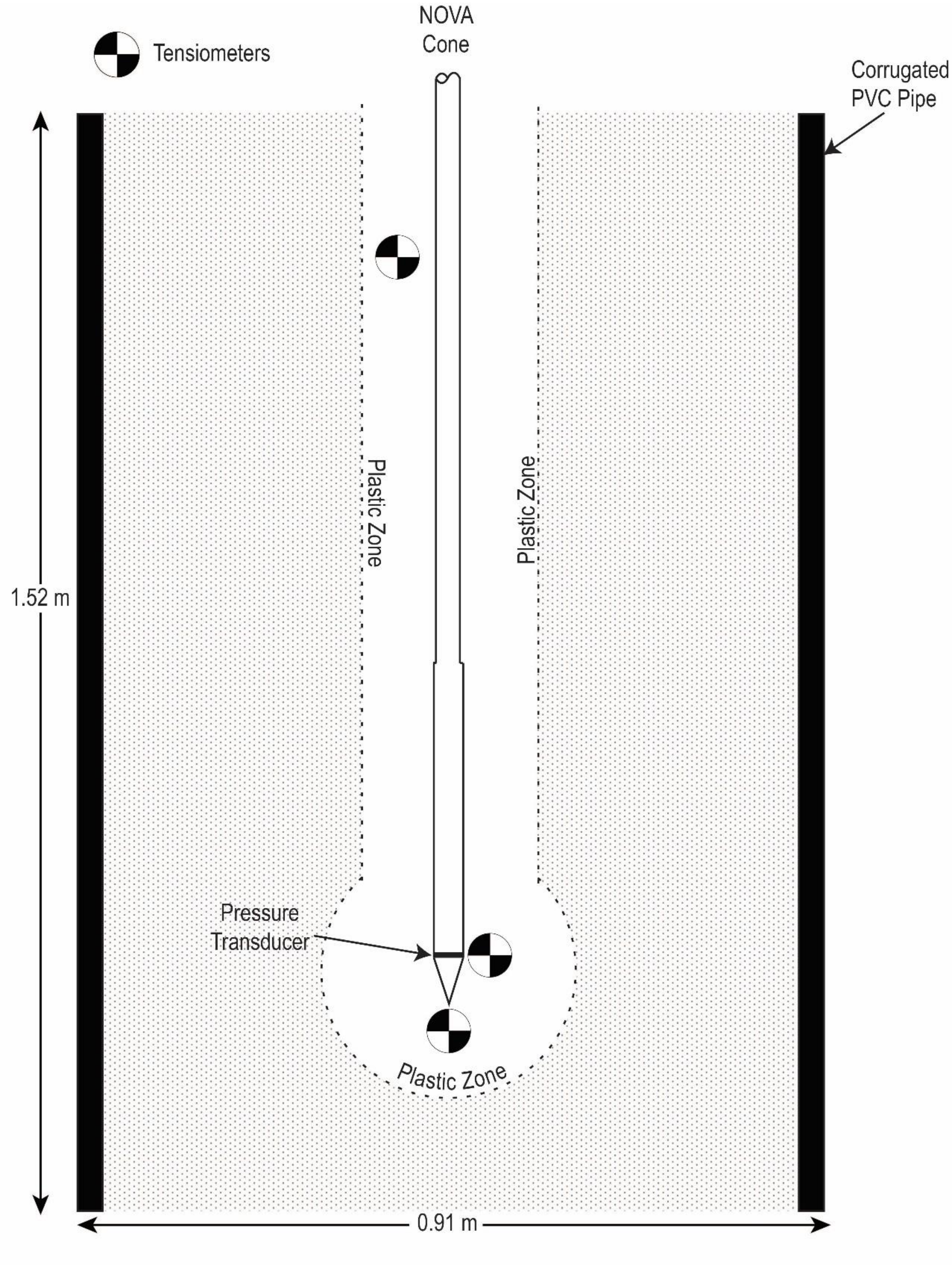

Figure 1- 2: CPT in instrumented chamber (Not to scale)

1.4 Thesis Outline

This thesis consists of two manuscripts. One has been accepted while the second has been submitted. Both were submitted to highly regarded, peer reviewed journals. In addition, two shorter papers have also been published in other conference proceedings (refer to the cover page of the specific chapter). The manuscripts were included in Chapter 2 and 4 of this thesis. The data and research findings will be presented as follows:

Chapter 2: Use of a 3D scanner for shrinkage curve tests

Chapter 3: Red silt material characterization

Chapter 4: Cone Penetration Testing in Unsaturated Silt with Matric Suction Measurements

Chapter 5: Closing Remarks

References

ASTM, D. (2000). Standard Test Method for Performing Electronic Friction Cone and Piezocone Penetration Testing of Soils. ASTM D-5778.

Campanella, R., & Robertson, P. (1988). Current status of the piezocone test. In Proc. 1st Int. Symp. on Penetration Testing, 1, 93-116.

Fredlund, D., & Houston, S. (2013). Interpretation of soil-water characteristic curves when volume change occurs as soil suction is changed. Proceedings, 1st Pan-American conference on unsaturated soils., 1, pp. 15-31. Cartagena de Indias, Columbia.

Fredlund, M.D.; Wilson, G.W.; Fredlund, D.G. (2002). Representation and estimation of the shrinkage curve. Third International Conference on Unsaturated Soils, 145-149.

CHAPTER 2. Use of a 3D scanner for shrinkage curve tests

by Jonathan M. Wong[1], David Elwood[2] and Delwyn G. Fredlund[3]

[1] MSc Candidate, Department of Civil, Geological and Environmental Engineering, University of Saskatchewan, Saskatoon, SK, Canada S7N 5B4. jmw932@mail.usask.ca

[2] Assistant Professor, Department of Civil, Geological and Environmental Engineering, University of Saskatchewan, Saskatoon, SK, Canada S7N 5B4. david.elwood@usask.ca

[3] Geotechnical Engineering Specialist, Golder Associates, 1721 - 8th St E, Saskatoon, SK, Canada S7H 0T4. delwyn.fredlund@gmail.com

Corresponding author
David Elwood
Department of Civil, Geological and Environmental Engineering, University of Saskatchewan
Saskatoon, Saskatchewan, Canada
S7N 5A9
Email: david.elwood@usask.ca
Tel: +1 (306) 966-3246

2.1 Preface

All work reported in this chapter, including design of the experimental program, implementation of the experiments, review of the literature, development of the theoretical framework, analysis and discussion of the results and writing of the text, has been carried out by the MSc. student. As supervisor, Dr. David Elwood reviewed all parts of the work.

A version of this chapter has been published with the following citations:

1. Wong, J. M., Elwood, D., & Fredlund, D. G. (2017, October). “Shrinkage Curve Evaluation Using a 3D Scanner”. In *GeoOttawa* (p. 8p).
2. Wong, J. M., Elwood, D., & Fredlund, D. G. (2018) " Use of a 3D scanner for shrinkage curve tests." *Canadian Geotechnical Journal* (In the process of publication).

This chapter may or may not contain additional details found in the published manuscripts.

2.2 Introduction

A soil matrix typically consists of three primary phases: the solid phase (soil particles), the water phase, and the air phase. The volume of water being removed from, or added to, a soil matrix does not necessarily equal the change in overall volume since changes in the soil structure also play a significant role (Haines, 1923). The relationship between the soil water content (at and below saturation) and its void ratio is known as the shrinkage curve. The shrinkage curve is particularly important for designing lightweight structures, such as soil cover systems, road pavements, and rail beds. Differential displacements (heave or settlement) in the presence or absence of water can result in damage to the structure, or cracking of the soil mass.

A continuous shrinkage curve equation is obtained by curve-fitting a shrinkage model to discrete measurements of void ratio and gravimetric water content obtained by performing a shrinkage limit test. The equation commonly used to fit the shrinkage data in geotechnical engineering was first proposed by Fredlund et al. (2002):

$$e(w_i) = a_{sh}\left[\left(\frac{w_i}{b_{sh}}\right)^{c_{sh}} + 1\right]^{1/c_{sh}} \qquad [2.1]$$

where,

a_{sh} is the minimum void ratio, b_{sh} is the slope of the line of tangency ($b_{sh} = \frac{a_{sh}S}{G_s}$); c_{sh} is a curve fitting parameter that determines the curvature of the shrinkage curve, w_i is the gravimetric water content, and $e(w_i)$ is the void ratio of the soil mass at any selected gravimetric water content w_i.

This shrinkage curve model has three parameters. Parameters a_{sh} and b_{sh} each have a physical meaning related to the shrinkage of the soil during drying. However, no physical meaning has been ascribed to parameter c_{sh}, other than it being related to the curvature of a shrinkage curve. If parameter c_{sh} can be related to plasticity of the soil, then shrinkage curves can be better estimated.

Historically, shrinkage limit tests were conducted using mercury displacement, but this method was withdrawn without replacement in 2008 due to health and safety concerns (ASTM D427-04). Many methods have since been developed, including the wax-dip method (Prakash et al., 2009), the photogrammetry method (Li et al., 2015) and direct measurement. These tests, however, either require a skilled hand to execute or assumptions to interpret the results. For example, the wax-dip method (ASTM D4943-08) is a destructive test that involves the preparation of multiple batches of soil samples at various water contents. The samples are dipped into molten wax to preserve the water content during mass-volume measurements. The test assumes that the difference in water content is the only factor affecting the volume of the soil specimen; however, this is hardly the case as sample preparation is an influencing factor. In 2017 April, the wax-dip method was also withdrawn without replacement due to it being out-dated (ASTM D4943-08).

Three-dimensional (3D) scanners have been proposed for measuring the volume of a soil sample at any water content (Wong et al., 2017). A major advantage of applying remote sensing technology (such as 3D scanners or photogrammetry) to shrinkage limit tests is that it results in minimal disturbance of the soil sample without compromising accuracy. The objective of this paper is to illustrate the use of a 3D scanner for shrinkage limit tests and propose a test procedure for obtaining the shrinkage curve. The scanning procedure provides a means of measuring the entire shrinkage curve based solely on the volume of an air-dried sample, the specific gravity and the Atterberg limits of the specimen. This effectively reduces the amount of work needed to determine the shrinkage curve.

2.3 Methodology

2.3.1 *Working Principle*

A 3D scanner utilizes “Light Detection and Ranging”, (LiDAR) technology and computer imaging to reconstruct a colored three-dimensional object. The 3D scan involves placing an object on a turntable at a fixed distance from the 3D scanner (Figure 2-1). The turntable is connected to the scanner and is programmed to rotate the sample following completion of a given scan. Sample rotation is required to obtain a complete 3D image of the test specimen.

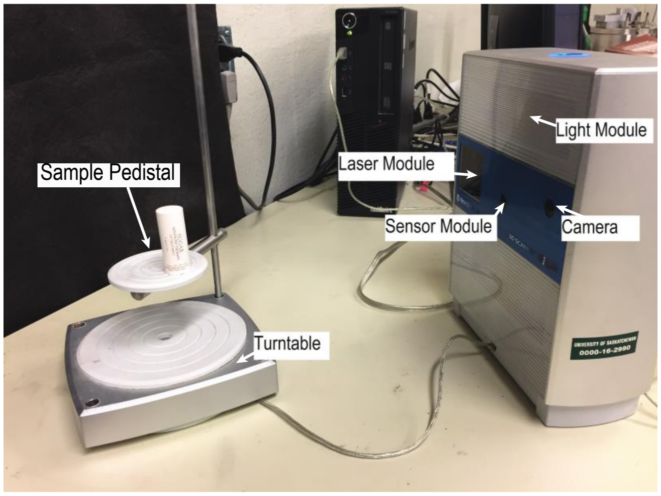

Figure 2- 1: 3D Scanner and Set-up.

The 3D scanner then uses a computer-imaging program to differentiate between the scanned object and the background. The camera takes a picture of the object during and after illumination by the light module. The processing unit compares the two images, and flags the pixels that have a significant change in light intensity (Figure 2-2). The colors of these flagged pixels are assigned to a corresponding point in a “point cloud”, thereby reducing the number of objects that need to be trimmed to obtain the sample volume. This procedure is in contrast to conventional LiDAR scanning where the results are filtered based on the time of return, and therefore the distance from the scanner.

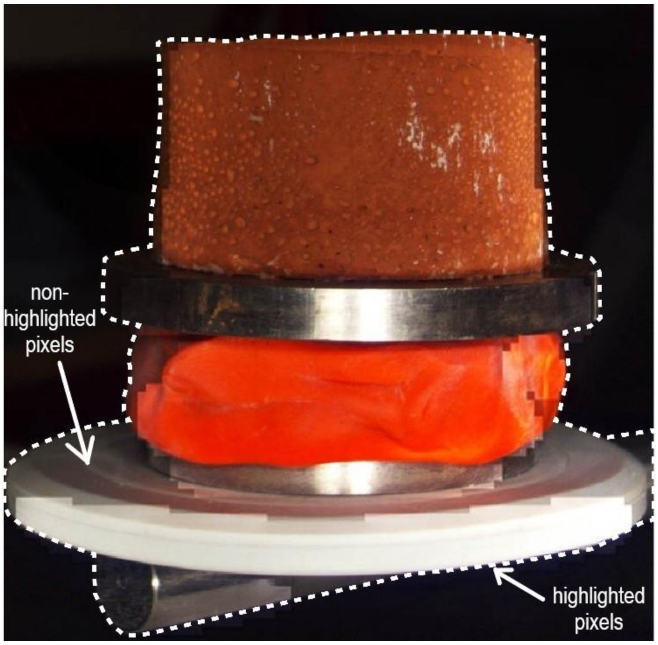

Figure 2- 2: Flagged and Non-flagged Pixels.

The laser module emits a series of laser points to the object upon completion of the imaging process. The sensor picks up the laser points that are reflected off the surface, and calculates the distance between the scanner and the object based on the time between when the light is emitted and returned to the scanner. Multiple 3D coordinates (point cloud) are generated simultaneously as the laser points scan across a surface continuously.

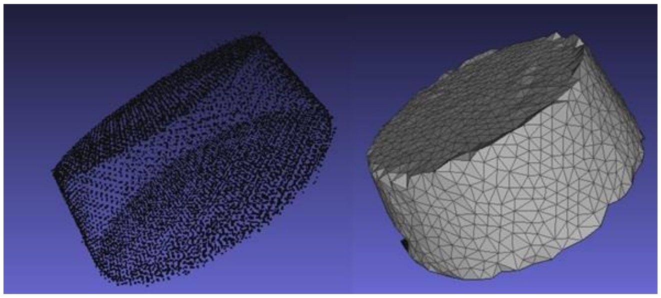

Figure 2- 3: Point Cloud (left) and Mesh (right) of Metallic Puck.

Once the surface of the object has been scanned, the turntable rotates the object until a new surface faces the scanner. This surface is scanned by repeating the previous procedure. The 3D coordinates of different faces are joined (“stitched”) together to form a 3D point cloud (a set of 3D coordinates) based on the surface topography and the overlaps of images (Figure 2-3). The density of the point cloud can be adjusted for different situations by setting the scanning resolution prior to scanning. A high-density point cloud (i.e., more than 11 points per mm^2), allows more surficial details to be captured but requires more processing time and computation power than a lower density meshed volume.

When scanning is complete, the 3D point cloud must be further edited prior to being used for the calculation of the overall volume. The edits require the trimming of any background details that may have been scanned despite the image processing described above. Following trimming of the erroneously captured points, the object is then transformed into a water-tight surface mesh (Figure 2-3) based on the point cloud using any conventional meshing software package.

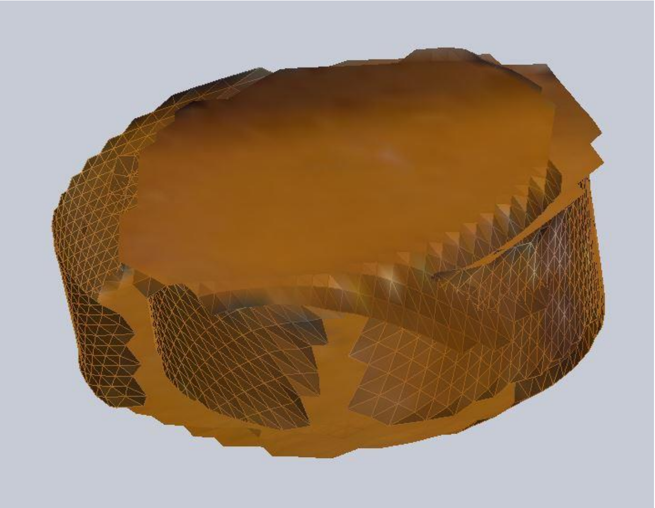

Figure 2- 4: Deformed Scan due to Holes.

The volume of the object can only be computed if the mesh is watertight. Any holes or voids in the mesh will result in an inaccurate calculation of the object volume. The missing data surfaces can subsequently affect the stitching process, and result in a deformed point cloud (Figure 2-4). The scanner requires a clear line of sight to the sample surface to avoid the presence of “holes” in the associated point cloud that result from missing data points or hidden surfaces, and therefore the shape and orientation of the soil sample must be considered. Flat surfaces that are parallel to the travel direction of the lasers are often a major contribution to holes and should be avoided. Shapes without a flat top surface, such as bullet shape, should be adopted instead (Figure 2-5).

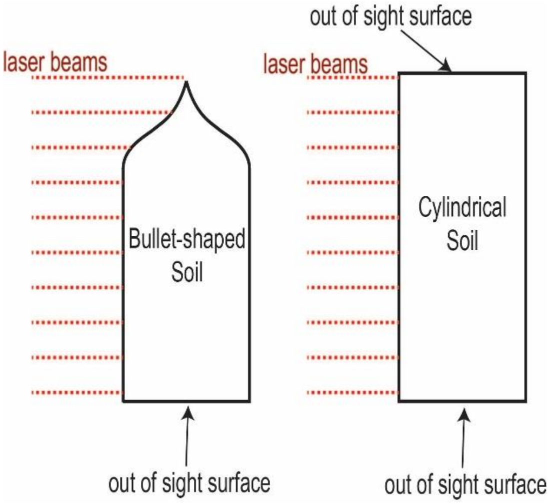

Figure 2- 5: Effectiveness of Scan for Different Shapes.

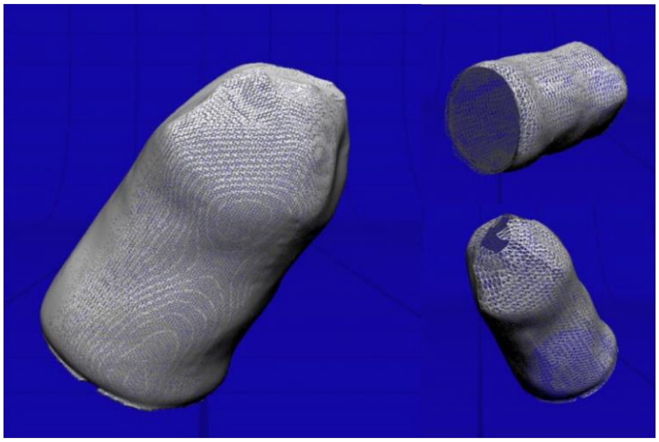

Figure 2- 6: Holes and Patched Area due to Line of Sight Errors.

Despite efforts to maintain a clear line of sight, some sample surfaces are inevitably out of sight, such as the tip and the bottom of the object (Figure 2-6). Small holes (e.g., at the tip), can be patched with a smooth flat surface during the meshing process. The “patch” is generated by averaging the orientation of the micro-surfaces around the holes. Bigger holes, such as the one at the bottom of the object, can be patched with a fabricated surface of specified orientation. The patched surface is only accurate if the base of the soil sample is indeed flat and smooth. Therefore, samples must be prepared in a manner that ensures good contact with the revolving baseplate.

2.3.2 Calibration

A calibration study was conducted to determine the accuracy of volumes obtained using the 3D scanner.

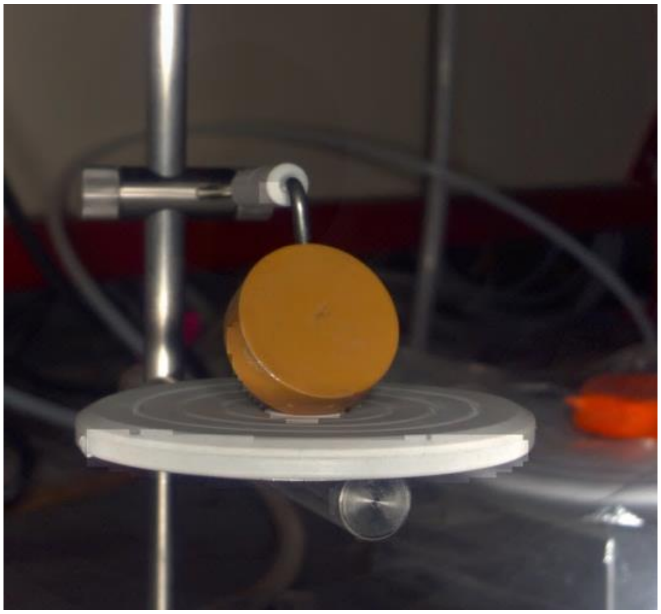

Figure 2- 7: Metallic Puck

The 3D scanner was used to measure the volume of a metallic puck (Figure 2-7) with an average diameter of 30.05 mm, height of 10.12 mm, and total volume of 7173.3 mm^3. The metallic puck was painted to simulate the color of soil samples to be scanned as part of the main study. The puck was scanned at different mounted positions a total of 12 times. The average scanned volume (± standard deviation) of the puck was 7820 (± 123.28) mm^3, corresponding to a difference of +9.02% with respect to the actual volume. These results indicate the scanner can provide consistent volume measurements but lacks in overall accuracy. Therefore, before or after a shrinkage limit test is completed, an object with known volume and similar dimensions to that of the soil specimen should be scanned. A calibration factor, α, is then obtained using the relationship

$$\text{Calibration Factor } (\alpha) = \frac{\text{Scanned volume}}{\text{True volume}} \qquad [2.2]$$

The calibration factor can then be applied to the scan results of the soil sample to determine a more accurate volume. The procedure can be repeated at different water contents to obtain the shrinkage curve.

2.3.3 3D Scanning Procedure

The proposed procedure for conducting a shrinkage limit test using a 3D scanner involves five steps; namely, scanner calibration, sample preparation, mass measurements, volume measurements, and drying. The scanner must first be calibrated for accurate volume measurements, as described above, by scanning a solid non-reflective object of similar volume to the soil sample. This allows the determination of the calibration factor (Eq. 2.2). Second, a soil sample with an initial water content between the plastic and liquid limits is recommended for a shrinkage limit test. The soil specimen is molded into a preferred shape for scanning. The specimen is placed on the platform where it remains until all scanning is complete. Third, the 3D scan normally takes 15 to 20 minutes and the water content might change during the scanning process (e.g., due to evaporation). Therefore, the mass of the sample should be measured twice (once prior to scanning and once immediately after scanning) to obtain an average gravimetric water content that represents the water content of the sample during 3D scanning. Fourth, the platform in contact with the soil sample is placed on top of the turntable and the desired resolution selected (e.g., 11 points per mm^2). Upon completion, the background information of the scan is trimmed, leaving only the point cloud. Meshing software is used to generate a watertight mesh from the point cloud and any existing “holes” are patched. The mesh is then exported for volume calculation. Once the mass of the soil sample is measured after 3D scanning, the sample can be left to air dry prior to taking the next mass and volume measurements. Steps three and four are repeated until the volume of the soil sample no longer significantly changes. The soil sample is then oven-dried for 24 h before measuring its dry mass and minimum volume.

Once the mass and volume measurements of the entire shrinkage curve have been obtained, the calibration factor (Eq. 2.2) must be applied to the volume measurements. The specific gravity of the soil (ASTM D854-14) is used to calculate the corresponding void ratios. Gravimetric water content and the void ratio of the soil sample are then calculated from the corrected volume measurements. The dataset can then be fitted with the shrinkage curve equation (Eq. 2.1).

2.4 Results and Discussion

The 3D scanner was used to obtain shrinkage curves for a wide range of soil samples (Table 2-1). The primary purpose of the shrinkage curve measurements was to determine whether a physical meaning of the c_{sh} variable could be related to the material characteristics. The materials selected were chosen based on their Atterberg limits with the intent of covering a wide range of plasticity values. The properties of the materials were either obtained from published literature or physically measured in the laboratory; namely Atterberg limits (ASTM D4318-17), specific gravity (ASTM D854-14), and particle size (ASTM D7928-17). Shrinkage data for the materials were obtained using the 3D scanner procedure. The shrinkage curve data was then fitted with the shrinkage curve equation (Eq. 2.1). The c_{sh} variable was the only unknown.

Table 2- 1: Sample materials and properties thereof for shrinkage curves

Material	Specific gravity	Clay fraction (%)	Atterberg limits		Shrinkage Equation Parameters		
			Liquid limit (%)	Plastic limit (%)	a_{sh}	b_{sh}	c_{sh}
Red silt	2.71	17	48	40	1.03	0.34	15.0
Kaolinite	2.6	52.4	59	36	0.36	0.14	9.0
Bentonite	2.53	83	751	100	6.05	1.95	2.5
Regina clay[a]	2.84	59	75	25	0.49	0.16	4.4
Tailings box 2[b]	2.45	60	55	30	0.35	0.14	6.0
Tailings box 11[b]	2.45	60	38	15	0.35	0.14	6.0
Kenya black clay[c]	2.7	Not stated	65	25	0.39	0.14	5.0
60/40 kaolinite/bentonite	2.62	64.8	329	25	0.64	0.27	3.1
Leda clay	2.63	78.5	60	36	0.51	0.19	9.1
50/50 kaolinite/red silt	2.96	43	50	36	0.66	0.19	12.1
Edmonton till[d]	2.7	56.5	35	15	0.59	0.22	5.5
Battleford till	2.73	36	29	18	0.43	0.15	7.4
Clavet silt	2.75	30.5	34	25	0.81	0.27	10.0
Silty clay[e]	2.72	Not stated	40	27	0.64	0.23	8.5
Heavy clay[e]	2.8	Not stated	92	26	0.47	0.15	4.0
London clay[a]	2.75	29.6	77	29	0.38	0.14	5.0
30/70 London clay/sand[a]	2.67	16.1	24	18	0.45	0.16	13.9
L40S-SC, 28%[a][1]	2.7	28	43	22	0.42	0.14	7.0
Janga clay[a]	2.75	40.8	73	28	0.36	0.14	4.9
Boom clay[a]	2.71	39.2	56	29	0.45	0.16	5.5
L00S, 45.38%[a][1]	2.75	45.38	89	32	0.42	0.15	4.4
L20S, 39.35%[a][1]	2.73	39.35	73	29	0.44	0.15	4.1
L30S, 37.57%[a][1]	2.71	37.57	65	26	0.47	0.16	4.4
L40S, 32.01%[a][1]	2.7	32.01	43	22	0.51	0.18	5.2
L60S - PP, 24.76%[a][1]	2.75	24.76	36	19	0.64	0.21	7.4
Blue clay[a]	2.75	36.79	63	27	0.60	0.21	6.3
HD bentonite[a]	2.8	48.93	402	45	0.55	0.18	3.0

[a] Zhang 2016; [b] Fredlund et al. 2011; [c] Dagg & Russam 1966; [d] Elwood et al. 2015; [e] Russam, 1958

---

[1] The materials have been only designated by the test name and percentage of clay fraction. A specific clay mineral or site source has not been provided.

Shrinkage curves can be divided into three phases according to Haines (1923). The phases are: normal shrinkage, residual shrinkage, and zero shrinkage. In the normal shrinkage phase, the soil is fully saturated, and its overall volume change equals the volume of water removed or added. Soil volume change is directly proportional to the water volume change until the water content of the soil drops below its plastic limit (Fredlund et al., 2011; Marinho, 2013), at which point it enters the residual shrinkage phase. Soils in the residual shrinkage phase are unsaturated. In this phase, the overall volume change of the soil is less than the change in the volume of water. Soil samples in the zero shrinkage phase are also unsaturated, and have no overall volume change despite the removal or addition of pore-water. The beginning of zero shrinkage phase is marked by the shrinkage limit, which is defined as "the water content below which further loss of water by evaporation does not result in a reduction of volume" (Peck and Terzaghi, 1948, p. 33). The three parameters in Eq. 2.1 (a_{sh}, b_{sh}, and c_{sh}) respectively represent the y-axis intercept upon complete drying of the sample; the slope of the initial saturation line (i.e., typically taken as the slope of the change in void ratio beyond the plastic limit), and the curvature of a shrinkage curve that transitions from a dry soil. The three parameters each represent the geometry of a segment of the shrinkage curve within the zero, normal, and residual shrinkage phases, respectively.

Haines (1923) and Fredlund et al. (2002) suggested a physical property that could be used to quantify the geometry of a shrinkage curve through to the residual shrinkage phase (c_{sh}). Haines (1923) suggested that the volume change through the residual shrinkage phase is related to the clay particle-water interactions within the sample. Fredlund et al. (2002) report a difference in c_{sh} values when soil samples are of different plasticity. The term clay activity (activity hereafter) introduced by Skempton (1953) attempted to combine the effect of clay fraction and plasticity:

$$\text{Activity} = \frac{\text{Plasticity Index}}{\text{Clay Fraction}} \qquad [2.3]$$

Where, plasticity index is the difference between the liquid limit (LL, %) and plastic limit (PL, %), and the clay fraction is the mass of clay particles within a soil sample (%).

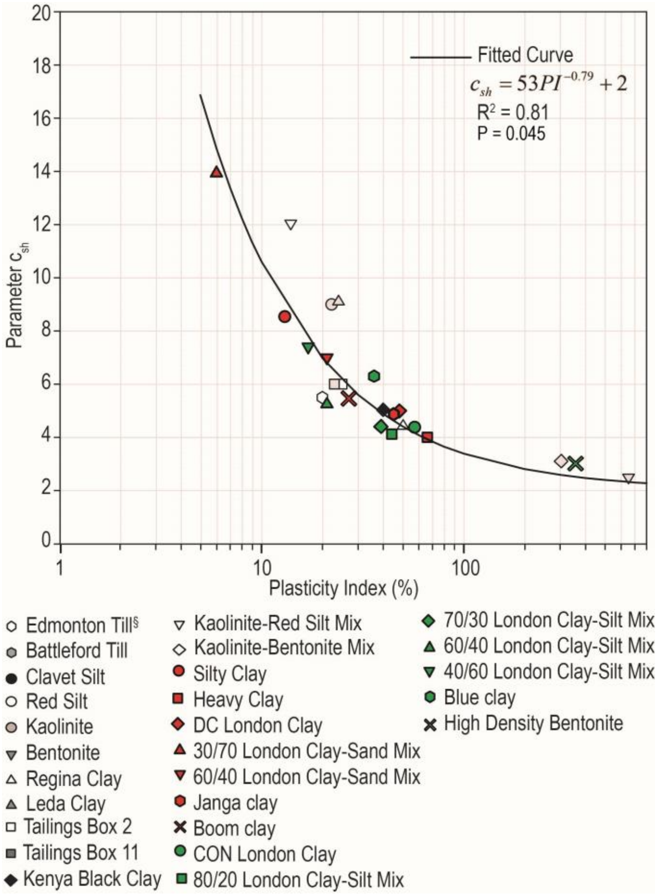

Figure 2- 8: Relationship between csh and Log Plasticity Index

A plot of c_{sh} vs. activity showed no consistent relationship. Atterberg limits, in particular the plasticity index, vary with clay content for soils with a clay fraction of 30% or higher (Seed et al. 1964; Polidori 2007). Plots of c_{sh} with respect to the plastic limit, liquid limit, and plasticity index showed the independence of c_{sh} in the low range of these plasticity variables. However, a power-function relationship was observed when c_{sh} was plotted against the plasticity index on a semi-log scale (Figure 2-8). Despite a low coefficient of determination was less than 90% ($R^2 = 0.81$), there is a high statistical significance between the two parameters, c_{sh} and plasticity, with a P value of (4.5%). The general trend of the curve shows an inverse relationship between c_{sh} and plasticity.

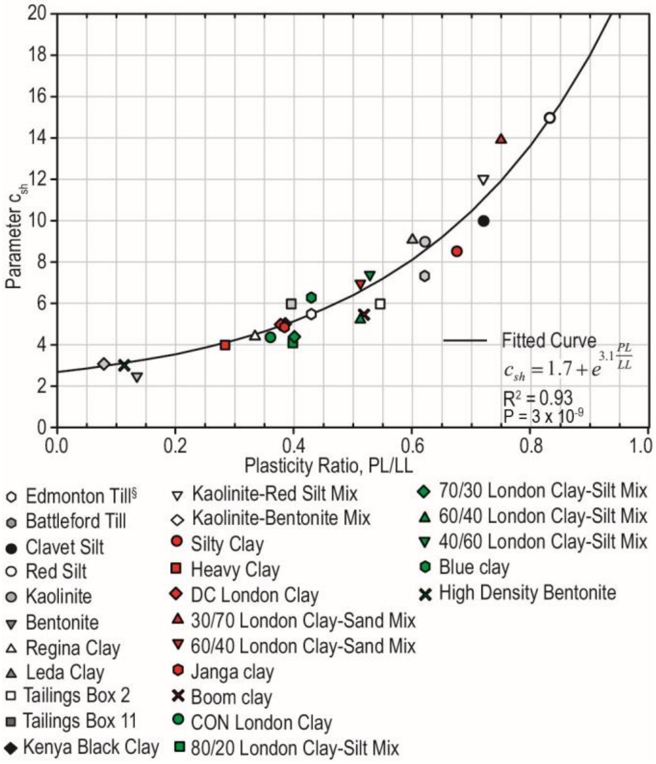

Figure 2- 9: Relationship between csh and Plasticity Ratio

A non-asymptotic relationship with higher R^2 values was obtained when the data was plotted as c_{sh} versus the ratio of the plastic and liquid limits (hereafter referred to as plasticity ratio) (Figure 2-9) The plasticity ratio has physical meaning in that a plasticity ratio of 0 indicates a high plasticity soil and 1 indicates a completely non-plastic soil. An empirical equation is obtained using a linear regression analysis that relates c_{sh} to the plasticity ratio:

$$c_{sh} = 1.7 + e^{3.1\frac{PL}{LL}} \qquad [2.4]$$

Shrinkage curves created using the c_{sh} values estimated from Eq. 2.4 were compared to those obtained through linear regression curve-fitting. The shrinkage curves produced based on Eq. 2.4 resulted in an average difference of ~1.2% in terms of void ratio (measured vs. predicted) and a maximum error of 6% when predicting the void ratio of extremely high plastic material (i.e., bentonite with a plasticity ratio near 0). Figure 2-10 to Figure 2-12 illustrate the quality of the estimated curves for materials of low, medium, and high plasticity.

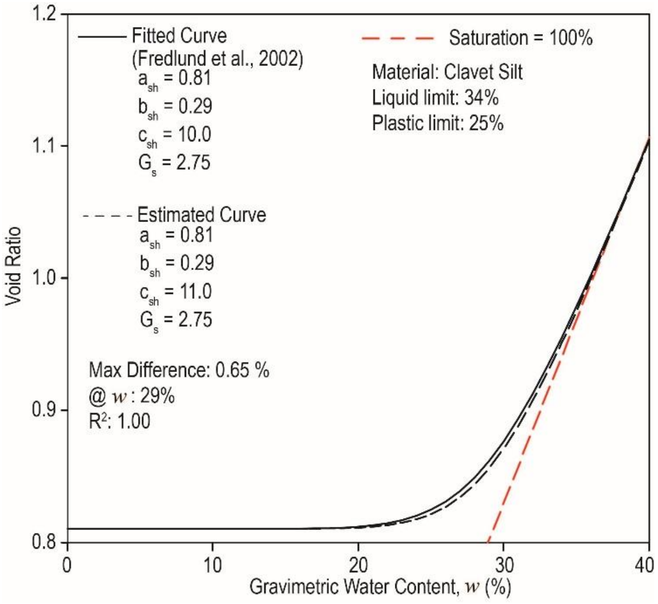

Figure 2- 10: Estimated Shrinkage Curve for a Low Plasticity Soil.

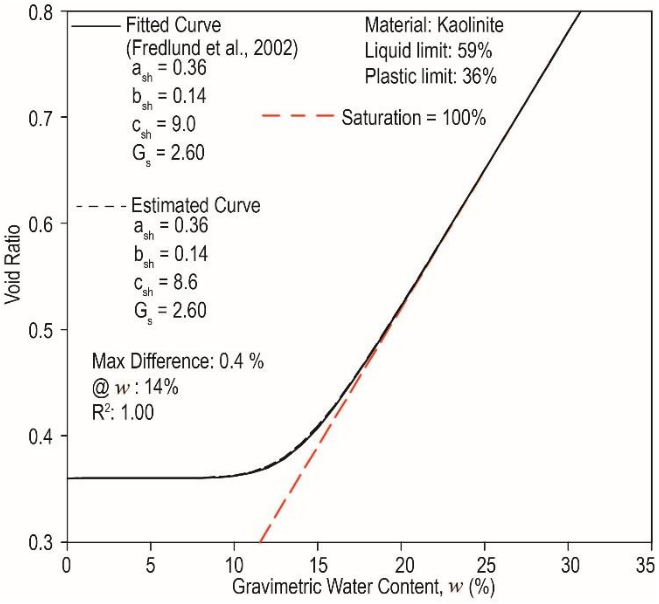

Figure 2- 11: Estimated Shrinkage Curve for a Medium Plasticity Soil.

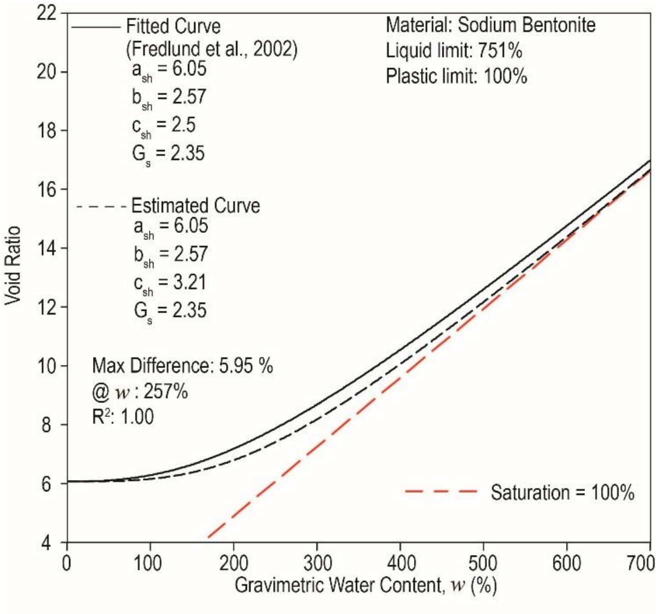

Figure 2- 12: Estimated Shrinkage Curve for a High Plasticity Soil.

2.5 Conclusions

This paper proposed a procedure for conducting shrinkage limit tests using a 3D scanner. Shrinkage limit tests were conducted on 27 different soils of various plasticity using the proposed procedure with shrinkage curves for these materials obtained by curve fitting a shrinkage model to measured datasets. Using a linear regression analysis, an empirical correlation was developed to reasonably relate parameter c_{sh} from the shrinkage model to the ratio of the plastic and liquid limits.

The proposed empirical equation effectively streamlines the process associated with obtaining a shrinkage limit test. Shrinkage limit tests usually require 24 to 48 hours of repetitive scanning and weighing. With the proposed empirical equation, the repetitive scanning and weighing cycles might be replaced by using the Atterberg limits and a single 3D scanning to obtain the minimum void ratio of a dried soil sample. Once the specific gravity of the soil is obtained, parameters a_{sh},

b_{sh}, and c_{sh} (and, thus, the entire shrinkage curve) can be estimated. This procedure considerably reduces the time required to obtain a shrinkage curve.

References

ASTM D427-04. 2004. Test Method for Shrinkage Factors of Soils by the Mercury Method (Withdrawn 2008), ASTM International, West Conshohocken, PA, 2004, www.astm.org

ASTM D4943-08. 2008. Standard Test Method for Shrinkage Factors of Soils by the Wax Method (Withdrawn 2017), ASTM International, West Conshohocken, PA, 2008, www.astm.org

ASTM D854-14. 2014. Standard Test Methods for Specific Gravity of Soil Solids by Water Pycnometer, ASTM International, West Conshohocken, PA, 2014, www.astm.org

ASTM D4318-17. 2017. Standard Test Methods for Liquid Limit, Plastic Limit, and Plasticity Index of Soils, ASTM International, West Conshohocken, PA, 2017, www.astm.org

ASTM D7928-17. 2017. Standard Test Method for Particle-Size Distribution (Gradation) of Fine-Grained Soils Using the Sedimentation (Hydrometer) Analysis, ASTM International, West Conshohocken, PA, 2017, www.astm.org

Bronswijk, J. 1988. Modeling of water balance, cracking and subsidence of clay soils. Journal of Hydrology, **97**: 199-212.

Dagg, M., and Russam, K. 1966. The relation between soil shrinkage and the development of surface cracks in an experimental road in Kenya. Road Research Laboratory, Harmondsworth. pp. 11-13.

Elwood, D., Martin, C.D., Fredlund, D., and Wilson, G.W. 2015. Volumetric changes and point of saturation around a pressuremeter probe used in unsaturated soils. ASCE Journal of Geotechnical and Geoenvironmental Engineering, **141**(11).

Fredlund, D., and Zhang, F. 2013. Combination of shrinkage curve and soil-water characteristic curves for soils that undergo volume change as soil suction is increased. *In* Proceedings of the 18th International Conference on Soil Mechanics and Geotechnical Engineering, Paris, France, September 2013, French Society for Soil Mechanics and Geotechnical Engineering (CFMS), Paris, France. **1**: 1109-1112.

Fredlund, D.G., Stone, J., Stianson, J., and Sedgwick, A. 2011. Determination of water storage and permeability functions for oil sands tailings. *In* Proceedings of Tailings and Mine Waste Conference, Vancouver, BC, November 7-9.

Fredlund, M.D., Wilson, G.W., and Fredlund, D.G. 2002. Representation and estimation of the shrinkage curve. *In* Proceedings of the Third International Conference on Unsaturated Soils, Recife, Brazil, 10-13 March 2002, pp. 145-149.

Haines, W. 1923. The volume-changes associated with variations of water content in soil. Journal of Agricultural Science, **13**: 296-310.

Li, L., Zhang, X., Chen, G., and Lytton, R. 2015. Measuring unsaturated soil deformations during triaxial testing using a photogrammetry-based method. Canadian Geotechnical Journal **52**: 1-18.

Marinho, F.A.M. 1994. Shrinkage behaviour of some plastic soils. PhD dissertation. University of London.

Marinho, F.A.M. 2013. Undrained shear of plastic soils under suction. *In* Multiphysical Testing of Soils and Shales: 45-55.

Peck, R., and Terzaghi, K. 1948. Consistency of remolded soils. *In* Soil mechanics in engineering practice. *Edited by* K. Terzaghi. John Wiley & Sons, Hoboken, NJ. pp. 32-34.

Polidori, E. 2007. Relationship between the Atterberg limits and clay content. Soils and Foundations, **47**(5): 887-896.

Prakash, K., Sridhara, A., Baba, J.A., and Thejas, H.K. 2009. Determination of shrinkage limit of fine-grained soils by wax method. Geotechnical Testing Journal, **32**(1): 1-4.

Seed, H., Woodward, R., and Lundgren, R. 1964. Fundamental aspects of the Atterberg limits. Journal of Soil Mechanics and Foundation Division, Americal Society of Civil Engineers, **90**(SM6): 75-105.

Skempton, A. 1953. Soil mechanics in relation to geology. Proceedings of the Yorkshire Geological Society, **1**(29): 33-62.

Wong, J., Elwood, D. and Fredlund D. 2017. Shrinkage Curve Evaluation using a 3D scanner. Proceedings of GeoOttawa2017, Canadian Geotechnical Society, **1**(235): 1-8.

Zhang, F. 2016. Unsatruated Soil Property Functions for High Volume Change Materials. PhD Dissertation. University of Alberta.

Chapter 3. Material Characterization

3.1 Introduction

As mentioned in Chapter 1, a silt material was used in the chamber test. A silt-type material was chosen for this research because of its problematic nature (highly erodible and brittle behavior) to construction. The silty material (denoted as the “red silt” in the following sections) originates from the South Saskatchewan River. It is a residual material produced by the filtration process at the drinking water treatment plant in Saskatoon. As its name suggests, the red silt possesses a reddish hue when dried. Characterization of the red silt was obtained as a result of the following evaluations:

- Specific Gravity;
- Grain Size Distribution;
- Atterberg Limits;
- Soil-Water Characteristic Curve (SWCC);
- Shrinkage Curve;
- Consolidation Parameters (One-dimensional/ Isotropic);
- Hydraulic Conductivity (Saturated and Unsaturated); &
- Saturated and Unsaturated Shear Strength profile

The following sections of this chapter will briefly discuss the methodologies involved in each test and their results.

3.2 Specific Gravity

Specific gravity tests were conducted as per ASTM D854. Pycnometers were used to measure the mass and volume of a deaired soil-water mixture of known water volume. The specific gravity (density of solids) were calculated. The averaged specific gravity of the red silt is 2.71.

3.3 Grain Size Distribution

Prior to testing, the red silt was mechanically sieved using a sieve with aperture size of 200 microns to remove unwanted materials such as metal shavings and wood chips. The particles that pass through the 200-micron-sieve were collected and used for characterization. A hydrometer test was the conducted on the sieved material to analyse the clay and silt portion therein. Hydrometer tests were conducted by following the procedures outlined in ASTM D7928. The grain size distribution curve is presented as Figure 3- 1:

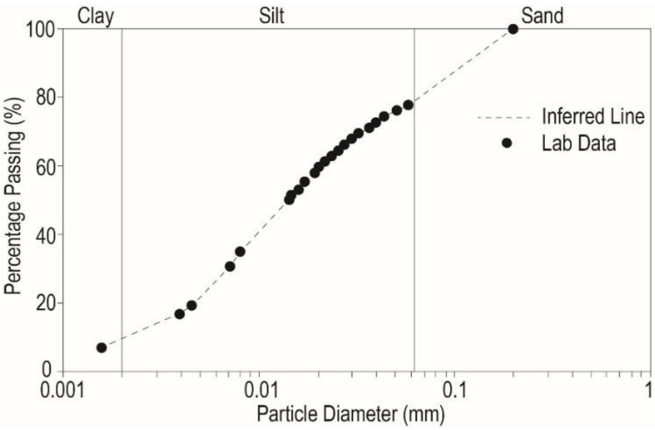

Figure 3- 1: Grain Size Distribution

The result indicates a soil composition, by mass, of 9% clay; 68% silt; 23% very fine sand for the sieved red silt.

3.4 Atterberg Limits

Atterberg Tests were conducted on red silt samples as per ASTM D4318 to obtain its liquid limit, plastic limit and plasticity index. Six Atterberg limit tests were conducted. The liquid limt ranges from 47% to 49%, averaging at 48%; the plastic limit ranges between 39% and 41%, averaging at 40%. This results in an averaged plasticity index of 8%. Using Casagrande’s Chart, the red silt is classified as a medium- to low-plasticity silt (MI).

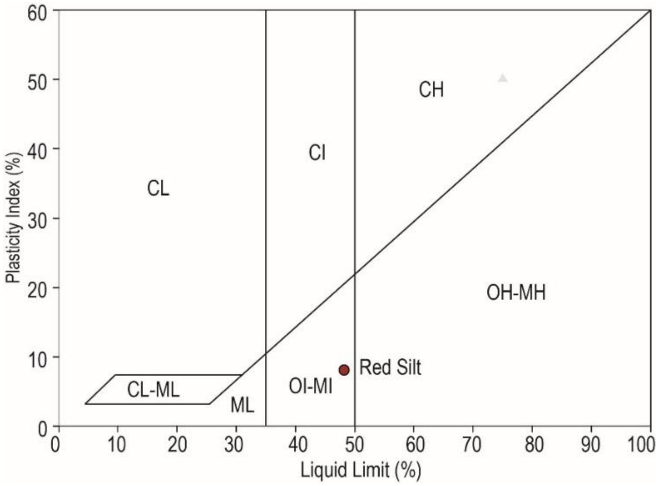

Figure 3- 2: Plasticity of Red Silt and Classification

3.5 Shrinkage Curve

The procedure for conducting a shrinkage test using a 3D scanner has been outlined in Chapter 2. A shrinkage test was conducted on the red silt with the use of a 3D scanner. The collected data set was curve fitted using the shrinkage curve equation proposed by Fredlund et al. (2002) (Eq. 3.1).

$$e\left(w\right)=a_{sh}\left[\left(w/b_{sh}\right)^{c_{sh}}+1\right]^{1/c_{sh}} \quad [3.1]$$

Where, a_{sh} denotes the minimum void ratio; b_{sh}, slope of the line of tangency; c_{sh}, curvature of the shrinkage curve; w, gravimetric water content; $e(w)$, void ratio of soil mass at gravimetric water content w.

The shrinkage curve of the red silt and the corresponding curve-fitting parameters are presented in Figure 3- 3.

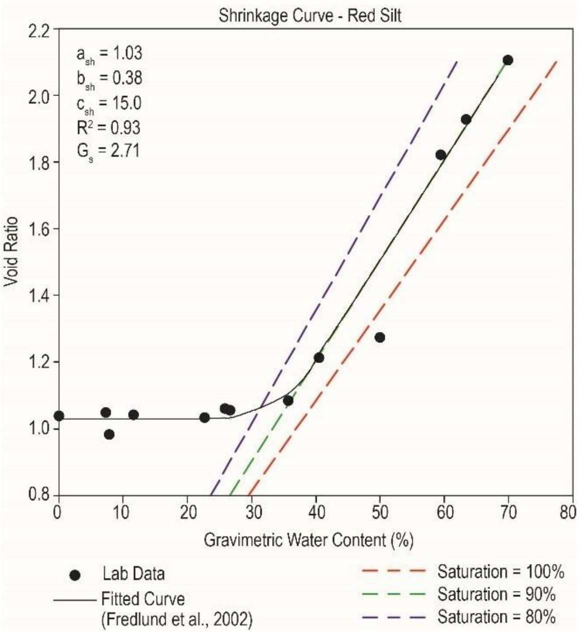

Figure 3- 3: Red Silt Shrinkage Curve

3.6 Soil-Water Characteristic Curve

A Soil-Water Characteristic Curve (denoted as "SWCC" in the following context) is a graph describing the retained water content within a soil sample under an applied matric suction. A typical SWCC possesses a reflected sigmoidal curve (Figure 3- 4).

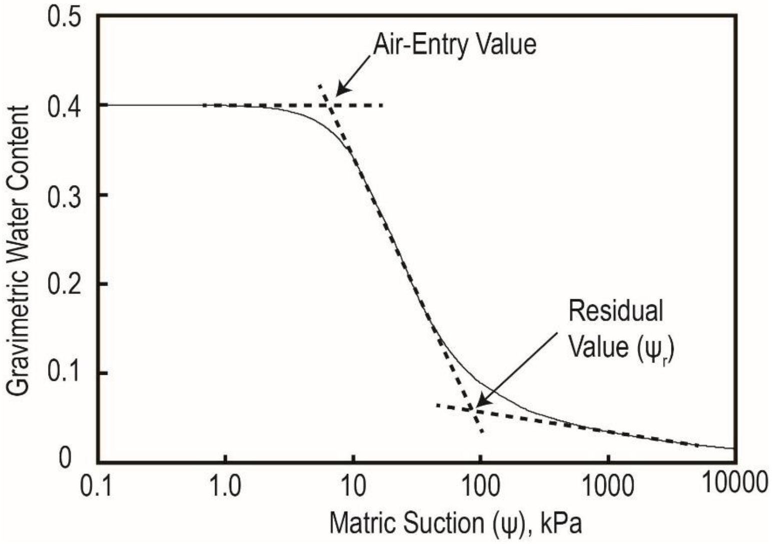

Figure 3- 4: A typical w-SWCC

At low matric suctions, the water content of the soil stays relatively constant. Once air-entry value (AEV) has been exceeded, the suction exceeds the surface tension of the water content within the pore space and air starts to intrude to the pore space. The water content continues to drop rapidly until the soil suction reaches a residual value; at which, further increase of suction has insignificant effect on the overall water content.

Often, SWCCs are interpreted by plotting gravimetric water content (*w*) against matric suction (*w*-SWCC); or by plotting volumetric water content (θ) against matric suction (θ-SWCC). These graphs could potentially result in an inaccurate estimation of AEV since the interpretations assume a constant volume of soil sample despite being pressurized (Fredlund & Houston, 2013). In the same publication, Fredlund & Houston proposed obtaining the air entry value by plotting a soil sample's instantaneous degree of saturation (S) against matric suction by combining a shrinkage curve with a *w*- or *θ*-SWCC using (Eq. 3.2) and (Eq. 3.3). The plot of degree of saturation against matric suction that combines shrinkage curve with *w*- or *θ*-SWCC is denoted as S-SWCC.

$$Se = wGs \tag{3.2}$$

$$\frac{Se}{1+e} = \theta \tag{3.3}$$

Where, S denotes the degree of saturation; G_s, specific gravity; *w*, gravimetric water content directly measured from a *w*-SWCC test; *e(w)*, void ratio of soil sample at gravimetric water content *w* which was obtained from a shrinkage test; *θ*, volumetric water content directly measured from a *θ*-SWCC test.

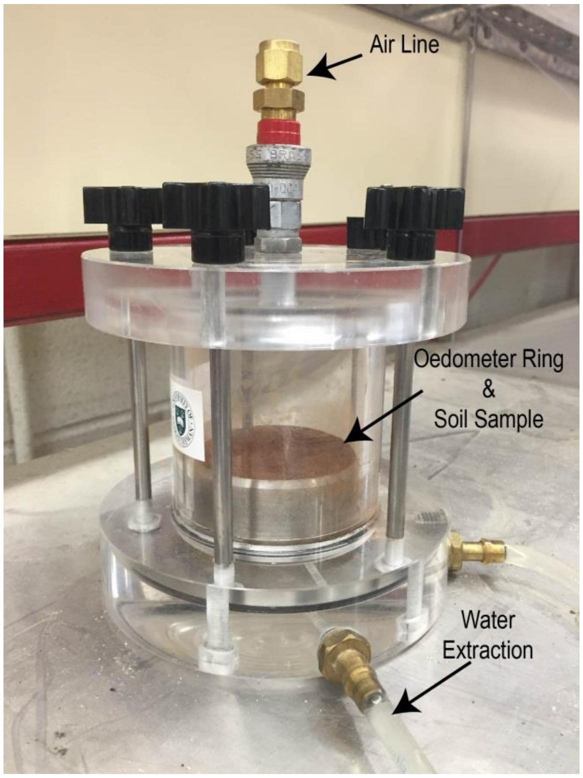

Figure 3- 5: w-SWCC using a pressure plate cell

A *w*-SWCC was obtained by conducting a SWCC test on a saturated red silt sample using a pressure plate cell (Figure 3- 5), as per ASTM D6836. The lab data was then curve fitted using the SWCC equation proposed by Fredlund & Xing (1994):

$$w(\psi) = \frac{w_i[1 - \ln(1 + \psi / \psi_r) / \ln(1 + 10^6 / \psi_r)]}{\left\{\ln[\exp(1) + (\psi / a_f)^{n_f}]\right\}^{m_f}} \quad [3.4]$$

Where, ψ denotes the matric suction; ψ_r, the residual matric suction; a_f, n_f and m_f, curve-fitting parameters; $w(\psi)$, gravimetric water content at matric suction ψ; w_i, initial gravimetric water content at saturation.

The curve fitted data (Figure 3- 6) was then combined with the shrinkage curve presented in Figure 3- 3 to obtain a SWCC (Figure 3- 7). The obtained AEV is 9.5 kPa; a residual suction of 75 to 80 kPa and a residual saturation of 20%.

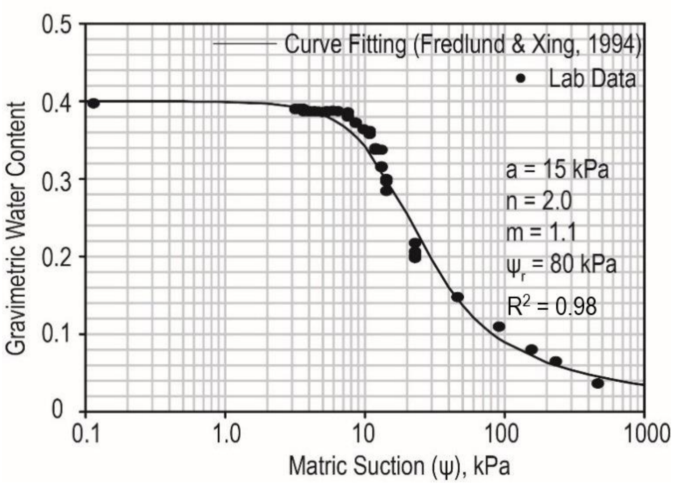

Figure 3- 6: Curve-fitted w-SWCC

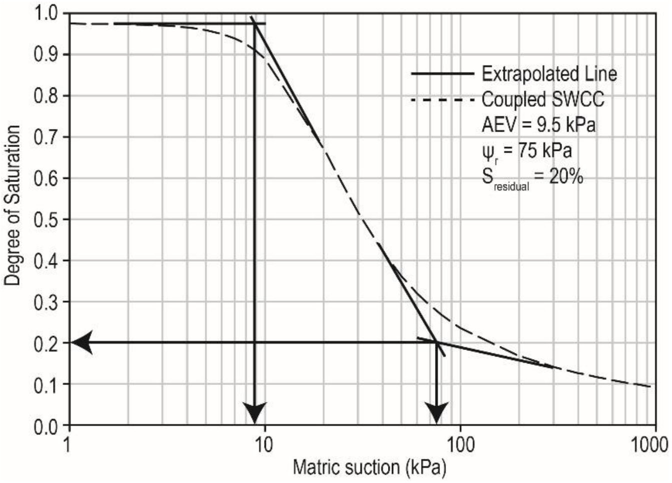

Figure 3- 7: S-SWCC obtained by coupling w-SWCC with the shrinkage curve

3.7 Consolidation Parameters

Consolidation tests were conducted on slightly compacted samples of red silt in oedometers and triaxial cells for one-dimensional and isotropic consolidation tests respectively.

3.7.1 One-Dimensional Consolidation Test

Procedures for one-dimensional consolidation tests were followed as per ASTM D2435. The purpose of one-dimensional consolidation in this research study is to obtain measurements of compression index (C_c) and recompression index (C_r) for future references. As presented in

Figure 3- 8, C_c and C_r respectively represent the slope of the virgin compression and recompression line on a *e*-log *σ'* (void ratio – log effective consolidation stress) plot. For the red silt sample, C_c is 0.078; C_r is 0.023.

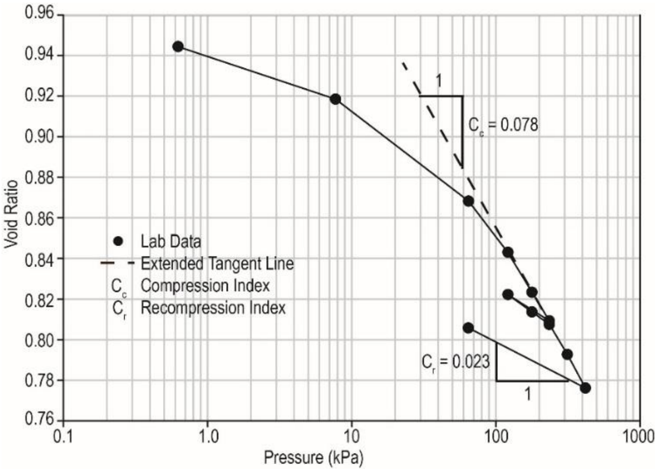

Figure 3- 8: Cc & Cr (One-dimensional Consolidation)

Though not intended, the slight compaction has given the red silt an apparent preconsolidation stress. Using the Casagrande Method, the apparent preconsolidation stress was found to be ~46 kPa. Whereas, a preconsolidation stress of ~59 kPa was obtained when the work method was used (Becker et al., 1987).

3.7.2 Isotropic Consolidation Tests

Multiple isotropic consolidation tests were conducted in the triaxial cell. The procedures for which were followed as per ASTM D4767-11. The red silt was wetted to an initial gravimetric water content of ~30%, followed by slight compaction to a bulk density of ~1.83 g/cm^3 inside a plastic pail. A thin walled tube of 1.5-inch diameter was used to extract samples from the pail vertically and horizontally. The extracted samples were set in a triaxial cell for isotropic consolidation tests. The following quantities of the red silt were obtained:

1. Consolidation Curve
2. Compression and Recompression Index (C_{cv}, C_{rv} & C_{ch}, C_{rh})
3. Coefficient of Consolidation (C_v & C_h)
4. Coefficient of volume compressibility (m_v & m_h)
5. Saturated Hydraulic Conductivity (k_v^{sat} & k_h^{sat})

NOTE: the subscript “h” and “v” is used to indicate the direction of measurement of the soil properties listed above.

Table 3- 1 summarizes the average value for all consolidation parameters mentioned above. Figure 3- 8 and Figure 3- 9 presents the trend between consolidation parameters and void ratios. Data value can be found in Table 3- 2 and Table 3- 3.

Table 3- 1: Averaged Consolidation Parameters

Item	Horizontal Direction	Vertical Direction
Compression Index, Cc	0.186	0.087
Recompression Index, Cr	0.018	0.019
Coefficient of Consolidation (NC), C (mm^2/s)	1.44	2.02
Coefficient of Volume Compressibility (NC), m (1/kPa)	1.23E-03	6.42E-04
Saturated Hydraulic Conductivity, ksat (m/s)	1.7E-08	1.3E-08

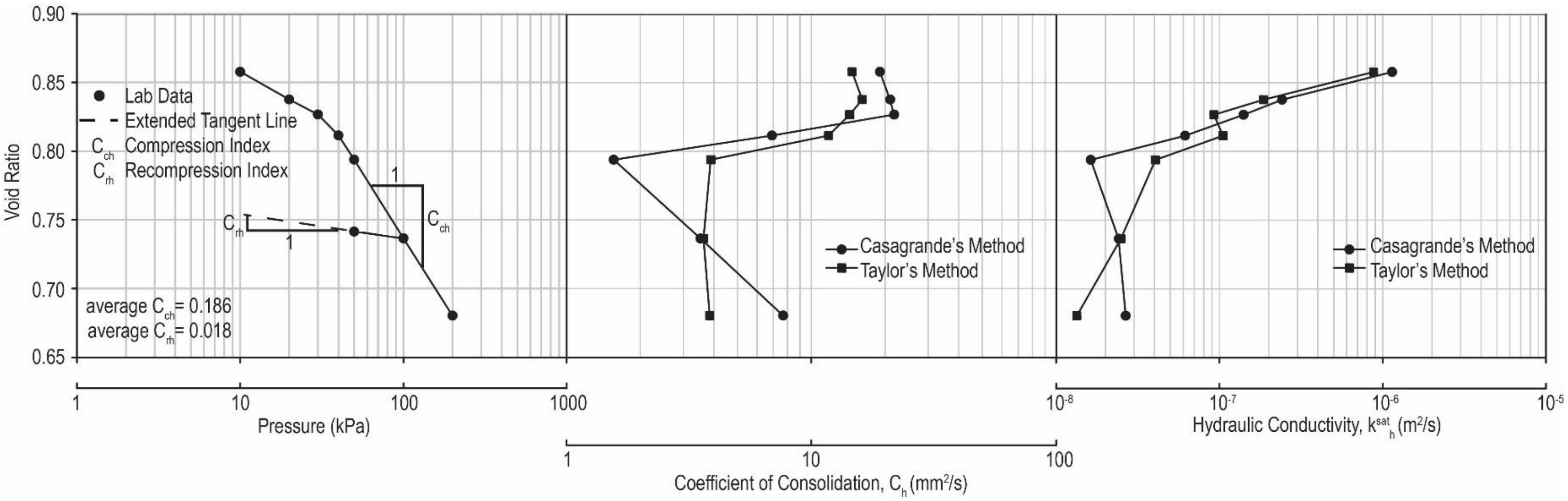

Figure 3- 9: Consolidation Parameters (Horizontal)

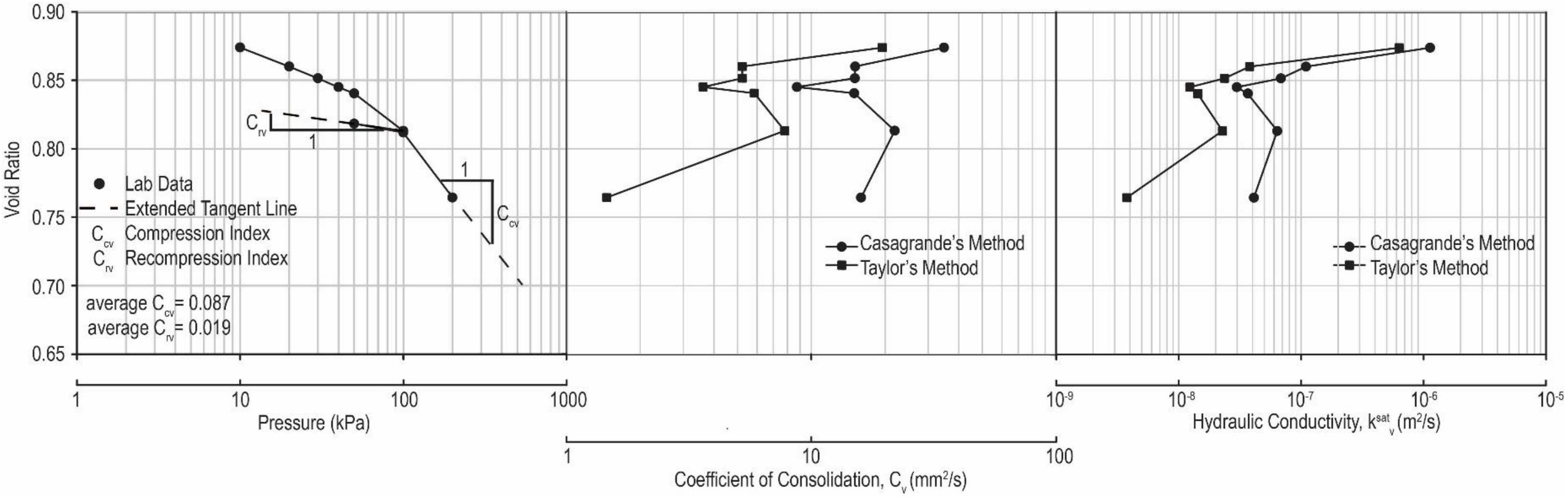

Figure 3- 10: Consolidation Parameters (Vertical)

Table 3- 2: Consolidation Data (Horizontal)

Stress (kPa)		Void Ratio			Casagrande's Method			Taylor's Method		
From	to	Initial	Final	m_h (1/kPa)	t_{50} (s)	C_h (mm^2/s)	k^{sat}_h (m/s)	t_{90} (s)	C_h (mm^2/s)	k^{sat}_h (m/s)
1	10	0.98	0.87	6.10E-03	27	19.07	1.14E-06	152	14.66	8.77E-07
10	20	0.87	0.85	1.18E-03	24	20.98	2.42E-07	135	16.14	1.86E-07
20	30	0.85	0.83	6.57E-04	23	21.76	1.40E-07	151	14.34	9.24E-08
30	40	0.83	0.82	9.08E-04	72	6.91	6.16E-08	183	11.77	1.05E-07
40	50	0.82	0.80	1.06E-03	317	1.56	1.63E-08	550	3.89	4.05E-08
50	100	0.80	0.73	6.97E-04	138	3.53	2.41E-08	580	3.63	2.48E-08
100	50	0.73	0.74	6.20E-05	9	53.55	3.26E-08	49	42.55	2.59E-08
50	100	0.74	0.73	6.12E-05	8	60.24	3.62E-08	31	67.26	4.04E-08
100	200	0.73	0.67	3.54E-04	62	7.67	2.67E-08	535	3.85	1.34E-08

Table 3- 3: Consolidation Data (Vertical)

Stress (kPa)		Void Ratio			Casagrande's Method			Taylor's Method		
From	to	Initial	Final	m_v (1/kPa)	t_{50} (s)	C_v (mm^2/s)	k^{sat}_v (m/s)	t_{90} (s)	C_v (mm^2/s)	k^{sat}_v (m/s)
1	10	0.93	0.87	3.30E-03	11	34.81	1.13E-06	85	19.49	6.31E-07
10	20	0.87	0.86	7.38E-04	25	15.13	1.09E-07	313	5.23	3.78E-08
20	30	0.86	0.85	4.61E-04	25	15.07	6.82E-08	312	5.22	2.36E-08
30	40	0.85	0.85	3.47E-04	43	8.74	2.97E-08	450	3.61	1.23E-08
40	50	0.85	0.84	2.49E-04	25	15.00	3.66E-08	277	5.86	1.43E-08
50	100	0.84	0.81	2.97E-04	17	21.93	6.39E-08	207	7.79	2.27E-08
100	50	0.81	0.82	5.72E-05	9	41.25	2.32E-08	266	6.04	3.39E-09
50	100	0.82	0.81	7.09E-05	9	41.24	2.87E-08	542	2.96	2.06E-09
100	200	0.81	0.76	2.62E-04	23	15.98	4.11E-08	1088	1.46	3.76E-09

3.8 Consolidated Undrained Triaxial Compression Tests

To capture the response of pore water pressure (u) of the red silt due to shearing, consolidated undrained triaxial compression tests (CU) were conducted as per ASTM D4767.

A total of nine undrained tests were conducted at three different effective consolidation stresses $\left(s'_p\right)$ and effective confining stress $\left(s'_3\right)$. A tabulated test plan is shown in Table 3- 4. All CU tests were conducted with a back pressure of 300 kPa. Samples were prepared with similar water content and bulk density indicated in “Isotropic Consolidation Tests”.

Table 3- 4: CU test plan

Effective Consolidation Stress (kPa)	Effective Confining Stress (kPa)	OCR
50	50	1
100	100	1
200	200	1
150	50	3
300	100	3
450	150	3
300	50	6
600	100	6
900	150	6

From the results of CU test, frictional parameters, namely friction angle (ϕ') and effective cohesion (c') were obtained. These parameters represent the effective shear strength of the soil. Each sample was sheared in a triaxial cell until it reached the critical state, from which the critical state friction angle (ϕ'_{cs}) was obtained. Furthermore, dilation angles (y) which represents volume change under shearing in drained condition can be calculated. As for undrained strength parameters, values of undrained shear strength (S_u) at various consolidation ratios (OCR) and confining stresses ($\sigma_3^{'}$) were obtained. In addition, the profile of internal pore-water pressure with shear strain (ε_q) can be captured.

3.8.1 Stress Paths

Figure 3- 11 and Figure 3- 12 are plots of total and effective stress paths respectively. The notations q, p and p' represents deviatoric stress, q ($\sigma_1 - \sigma_3$), mean total stress, p ($\frac{\sigma_1 + 2\sigma_3}{3}$) and mean effective stress, p' ($\frac{\sigma_1 + 2\sigma_3}{3} - u$) respectively. As indicated in Figure 3- 11, the slopes of the total stress paths were 3:1 as defined by a triaxial testing set-up. An increase in confining stress and/or consolidation stress both leads to an increase in deviatoric stress at failure (q_f). Before decreasing to q_f, a peak value (q_{peak}) was reached as demonstrated in Figure 3- 11 and Figure 3- 12. This behavior is caused by dilation and is quantified by dilation angles.

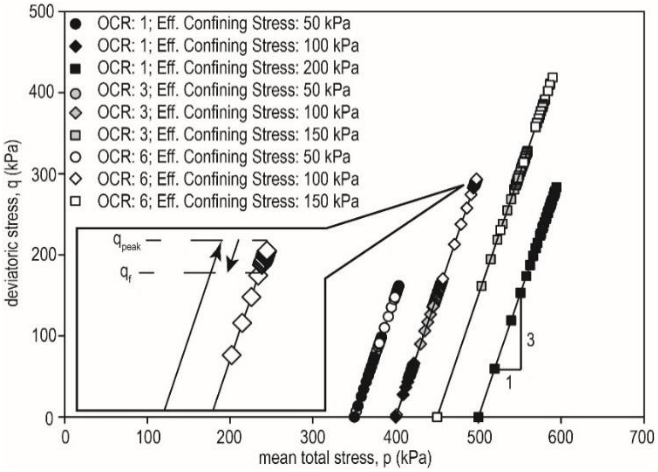

Figure 3- 11: Total Stress Path (CU)

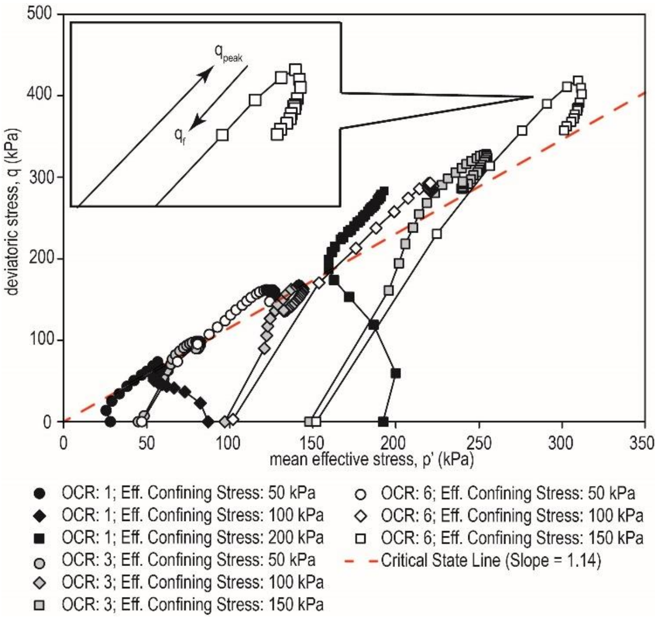

Figure 3- 12: Effective Stress Path (CU)

3.8.2 Critical State Parameters

Critical state was reached when the sample is sufficiently sheared until no volume change takes place. At critical state, the ratio between *q* and *p'*, known as "η", remains at a constant value "M". The value of M was found from the slope of the critical state line (Figure 3- 12) and the terminal value of η (Figure 3- 13). For the red silt sample, M is 1.22.

Another commonly used critical state parameter is the critical state friction angle (ϕ'_{cs}). As its name indicates, ϕ'_{cs} is the friction angle of the material at critical state.

$$M = \frac{6\sin\phi'_{cs}}{3-\sin\phi'_{cs}} \qquad [3.5]$$

Eq. 3.5, which was derived from Modified Cam-Clay Model (Schofield & Wroth, 1968), can be used to calculate ϕ'_{cs}. The critical state friction angle of the red silt was found to ranges from 28.6 degrees to 32.1 degrees, averaging 30.4 degrees.

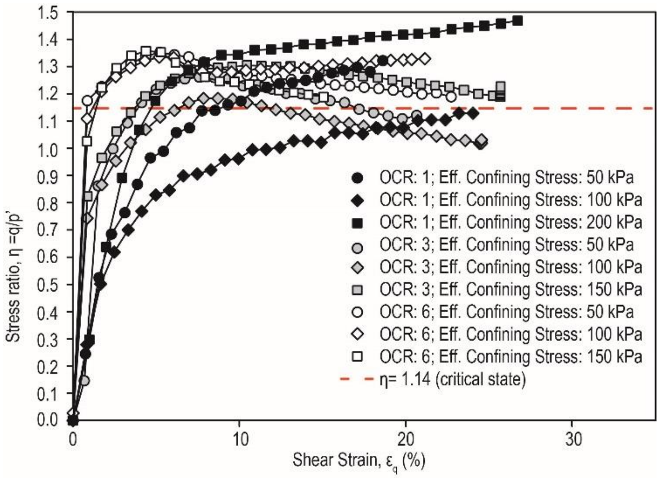

Figure 3- 13: Stress ratio plot (CU)

3.8.3 Elastic Modulus and Shear Modulus

Undrained Elastic Modulus (E_u) and Shear Modulus (G) were obtained by plotting deviatoric stress (q) against axial strain (ε_a) and shear strain (ε_q) respectively. In CU test, ε_a and ε_q are equal in magnitude (Muir Wood, 1990). As presented in Figure 3- 14, the initial slope of a $q - \varepsilon_q$ equals to E_u, which is equivalent to $3G$. The Undrained Elastic Modulus of the red silt range from 2,500 kPa to 25,000 kPa, averaging at 13,750 kPa; the Shear Modulus ranges from 833 kPa to 8,333 kPa, averaging at 4,583 kPa.

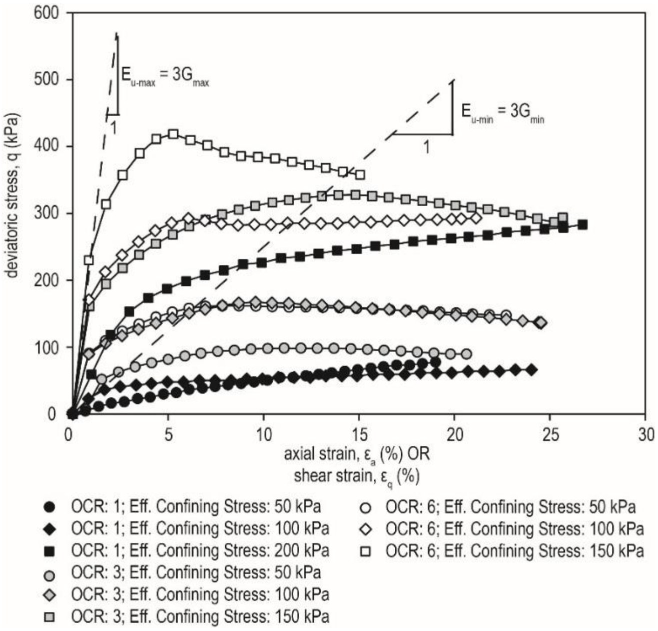

Figure 3- 14: Deviatoric Stress vs. Strain (CU)

3.8.4 Pore-Water Pressure Response

Excess pore-water responses were recorded during the CU tests. As presented in Figure 3- 15, positive pore pressure responses were recorded at low OCR values (OCR<3). As the OCR increases, the amount of generated excess pore-water pressure decreases. At OCR of 6, this decrease eventually comes to a generation of suction, where pore-water pressure decreases to a value lower than the applied back pressure (300 kPa). This phenomenon is commonly known as negative pore-water pressure and is a result of dilation. In CD tests, where pore-water pressure was controlled at a constant value, the volume of the sample increases instead.

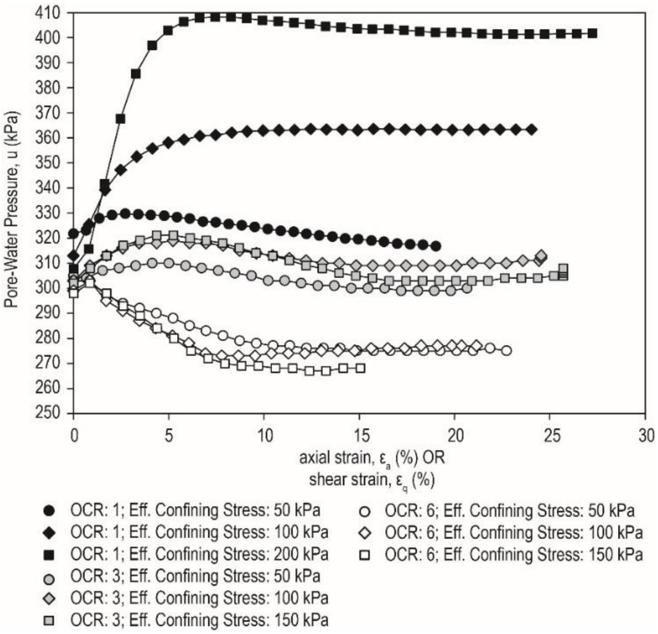

Figure 3- 15: Pore-Water Response (CU)

Table 3- 5 summarizes the pore-water pressure response in the CU tests. As mentioned, the pore-water pressure reaches positive excess pressure of ~ 0 to 100 kPa at OCR of 1 when being sheared. The magnitude of positive excess pressure being generated decreases drastically with increasing consolidation stress. At an OCR of 3, the positive excess pore-water pressures were offset by the dilation effect, from which the net change of pore-water pressures are negligibly small. The pore-water pressure eventually drops to the suction range, where the pore-water pressure becomes lower than that of the initial value (back pressure). At an OCR of 6, the suction being generated is ~30 kPa.

Table 3- 5: Pore-water pressure response (CU)

OCR	Confining Stress (kPa)	Pore-water Pressure (kPa)		
		initial	maximum	final
1	50	321	330	317
1	100	313	362	362
1	200	307	408	401
3	50	305	311	298
3	100	303	318	304
3	150	302	322	308
6	50	303	302	273
6	100	299	303	275
6	150	298	304	266

3.8.5 Mohr's Circle

Mohr's circle is plotted using the value of σ'_1 and σ'_3 at failure (peak value), namely σ'_{1f} and σ'_{3f}. Multiple Mohr's circles of same OCR were plotted together to obtain the effective friction angle (ϕ') and effective cohesion (*c'*), therefore, the Mohr-Coulomb failure envelope (Figure 3-16). The friction angles and effective cohesions for the red silt at various OCRs are summarized in Table 3- 6.

Table 3- 6: Stresses at failure (CU)

OCR	Confining Stress (kPa)	u_f (kPa)	σ'_{1f}	σ'_{3f}	c'	ϕ'
1	50	330	59	20	0	29.9
1	100	363	144	37	0	29.9
1	200	409	306	91	0	29.9
3	50	302	146	48	0	30.4
3	100	314	253	86	0	30.4
3	150	305	473	145	0	30.4
6	50	282	230	68	0	33.3
6	100	278	415	122	0	33.3
6	150	279	589	171	0	33.3

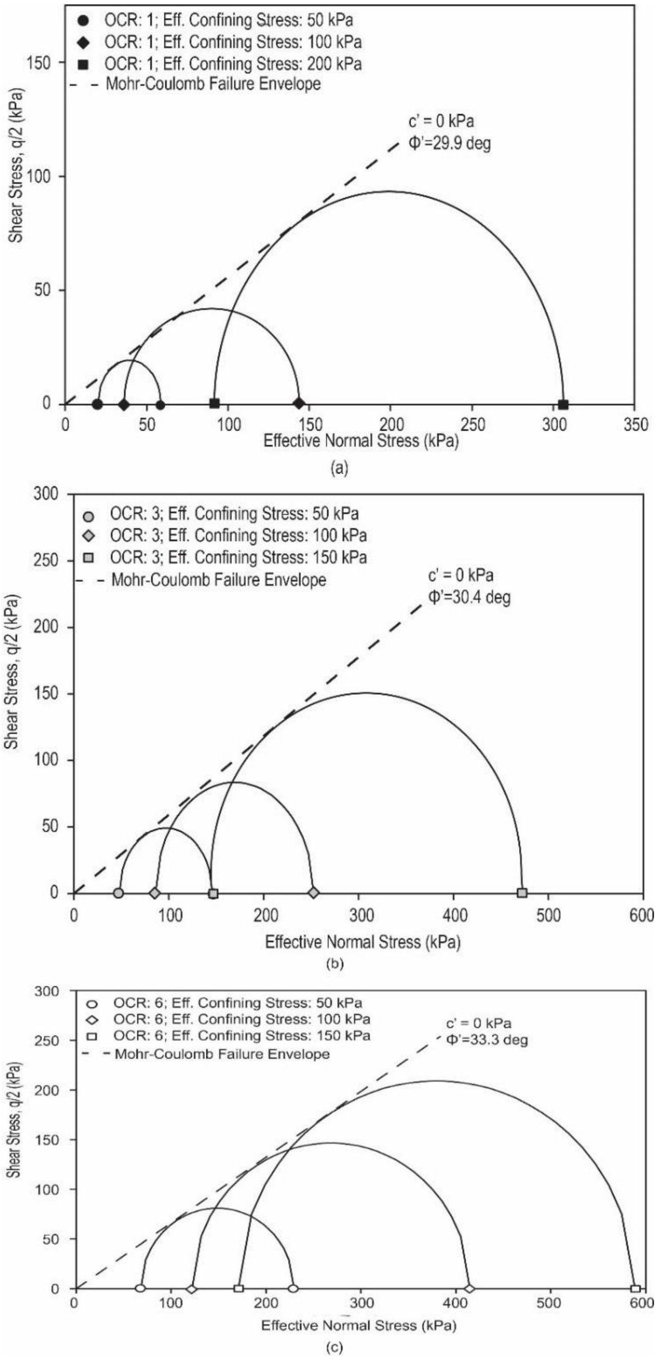

Figure 3- 16: Mohr-Coulomb failure envelopes

3.8.6 *Undrained Strength Parameters*

In a confined environment, undrained shear strength (S_u) was obtained using the peak deviatoric (q_{peak}) value (Eq. 3.6) The S_u values obtained from each CU test are presented in Figure 3- 17 and Table 3- 7.

$$S_u = \frac{q_{peak}}{2} \qquad [3.6]$$

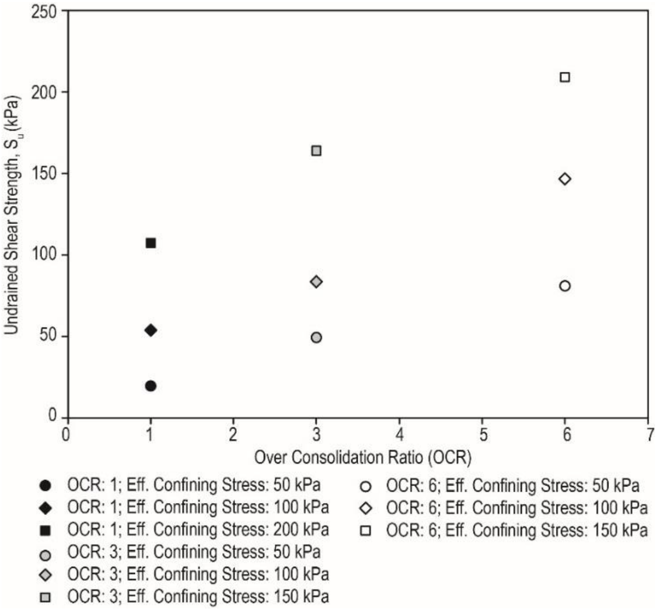

Figure 3- 17: Undrained Shear Strength (CU)

Table 3- 7: Undrained Shear Strength Values (CU)

OCR	Confining Stress (kPa)	Su (kPa)	Su/σ'_1 (kPa)
3	50	49	0.98
3	100	83	0.83
3	150	164	1.09
6	50	81	1.62
6	100	146	1.46
6	150	209	1.39
1	50	19	0.39
1	100	54	0.54
1	200	107	0.54

Ladd & Foott (1974) observed that S_u is dependent of the consolidation history and confining stress of a soil sample, and that when S_u is normalized and plotted against OCR, the values collapsed onto one single power function (Eq. 3.7). This method was later on known as “Stress History And Normalized Soil Engineering Properties (SHANSEP)”.

$$(\frac{S_u}{\sigma'_1})_{OC} = (\frac{S_u}{\sigma'_1})_{NC}(OCR^{\Lambda}) \qquad [3.7]$$

Where, $(\frac{S_u}{\sigma'_1})_{NC}$ equals the ratio of undrained shear strength to vertical confining stress of a normally consolidated sample; $(\frac{S_u}{\sigma'_1})_{OC}$ stands for the ratio of undrained shear strength to vertical confining stress of an over consolidated sample; OCR as the over consolidation ratio; Λ is a curve-fitting parameter. The average value of $(\frac{S_u}{\sigma'_1})_{NC}$ is 0.487, and using linear regression analysis, Λ was found to be 0.627.

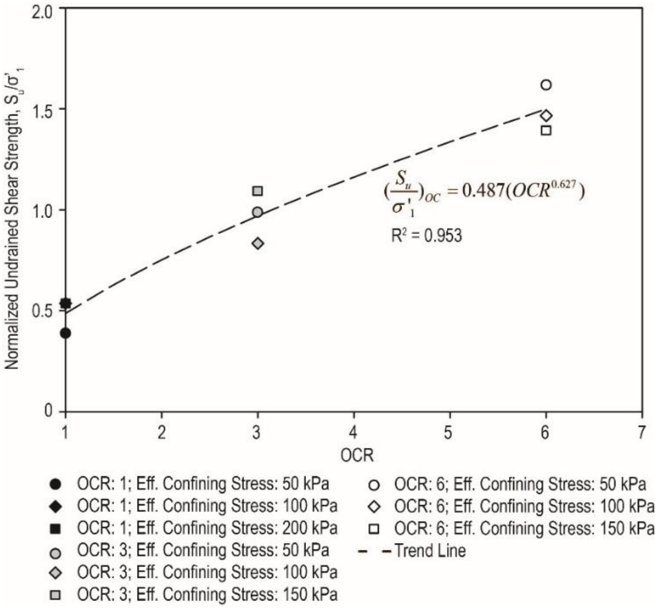

Figure 3- 18: Normalized Undrained Shear Strength (CU)

As presented in Figure 3- 18 and Table 3- 7, OCRs were plotted against normalized values of undrained shear strength ($\frac{S_u}{\sigma'_1}$). A trend line (Eq. 3.7) was curve fitted to the data set.

3.8.7 Dilation Angles

Dilation angle (ψ) is defined as the ratio of volumetric strain to shear strain in Consolidated Drained Tests. However, soil samples are kept at constant volume in CU tests. Rowe (1962) and Bolton (1986) has developed a correlation to ψ using peak friction angle (ϕ') and critical state friction angle (ϕ'_{CS}).

Using the dilation angle calculated with Rowe's or Bolton's equation, the volumetric strain of a soil when being sheared was estimated using equations developed by Houlsby (1991) under plane strain condition or Vermeer & De Borst (1984) under axis-symmetric condition. A list of calculation methods for dilation angles have been listed in Table 3- 8.

Table 3- 8: Literature References for Dilation Angle Calculations

Equation for dilation angle	Literature
$\sin\psi_R = \frac{\sin\phi'_{peak} - \sin\phi'_{cs}}{1 - (\sin\phi'_{peak}\sin\phi'_{cs})}$	Rowe (1962)
$\sin\psi_H = \frac{-\dot{\varepsilon}_v}{\dot{\varepsilon}_q}$	Houlsby (1991)
$\sin\psi_{VD} = \frac{-\dot{\varepsilon}_v / \dot{\varepsilon}_1}{2 - \dot{\varepsilon}_v / \dot{\varepsilon}_1}$	Vermeer & De Borst (1984)
$0.48\psi_B = \phi'_{peak} - \phi'_{cs}$	Bolton (1986)

As mentioned earlier, dilation angles of CU tests were calculated using equations proposed by Rowe (1962) and Bolton (1986) (Table 3- 9).

Table 3- 9: Dilation Angles (CU)

OCR	ϕ' (degrees)	ϕ'_{cs} (degrees)	ψ_R (degrees)	ψ_B (degrees)
1	29.9	30.4	-0.6	-1.0
3	30.4	30.4	0.0	0.0
6	33.3	30.4	3.4	6.0

NOTE: negative dilation angles indicate the soil being a strain-hardening material (contract when sheared).

As demonstrated in Table 3-9, dilation begins to take place when the OCR exceeds 3. The result is consistent with that shown in the pore-water pressure response (Figure 3-14), at which suction generation begins to start at an OCR value slightly exceeding 3.

One may observe that the dilation angle using Bolton's equation is nearly double that of Rowe's. Vermeer & Schanz (1996) observed the underestimation of dilation angle using Rowe's method and questioned one of Rowe's assumptions, which assumes the friction angle at failure in plane strain condition equals that of the critical state friction angle in axi-symmetric conditions (triaxial).

3.9 Unsaturated Consolidated Undrained Triaxial Compression Test

To obtain the shear strength profile of the red silt in various unsaturated conditions, seven Unsaturated Consolidated Undrained Triaxial (UCU) Tests were conducted. Although not listed as one of the ASTM standards, the procedures of unsaturated traixial tests can be readily found in many publications (Fredlund & Rahardjo, 1993; Ho & Fredlund, 1982; Leong et al., 2013).

Similar to the procedures of CU tests (ASTM D4767), a soil sample was first saturated and consolidated to an effective stress of 50 kPa to mimic the apparent consolidation effect due to compaction. Upon completion of consolidation, the sample was then desaturated by applying air pressure through the top cap (Figure 3-19). Using the axis-translation technique, the matric suction can be controlled by varying pore-air pressure (u_a) and pore-water pressure (u_w) to the sample (Hilf, 1956). The magnitude of matric suction (ψ) using axis translation technique is given by:

$$\Psi = u_a - u_w \qquad [3.8]$$

While increasing the applied air pressure, the confining stress (σ_3) was raised at the same time to maintain the net normal stress ($\sigma_3 - u_a$) at the designated value. The shearing process was commenced after the desaturation process was completed. To shear the sample under undrained condition, the valves leading to pore-air pressure and back pressure was closed. Shearing was achieved by increasing the axial strain at a fixed rate. The rate of shearing for the red silt samples were set at 0.0025% strain per minute as suggested by Bishop & Donald, 1961; Ho & Fredlund, 1982; and Chantawarangu, 1983. The shearing process was continued until the deviatoric stress and the pore pressures no longer measured a change upon further straining.

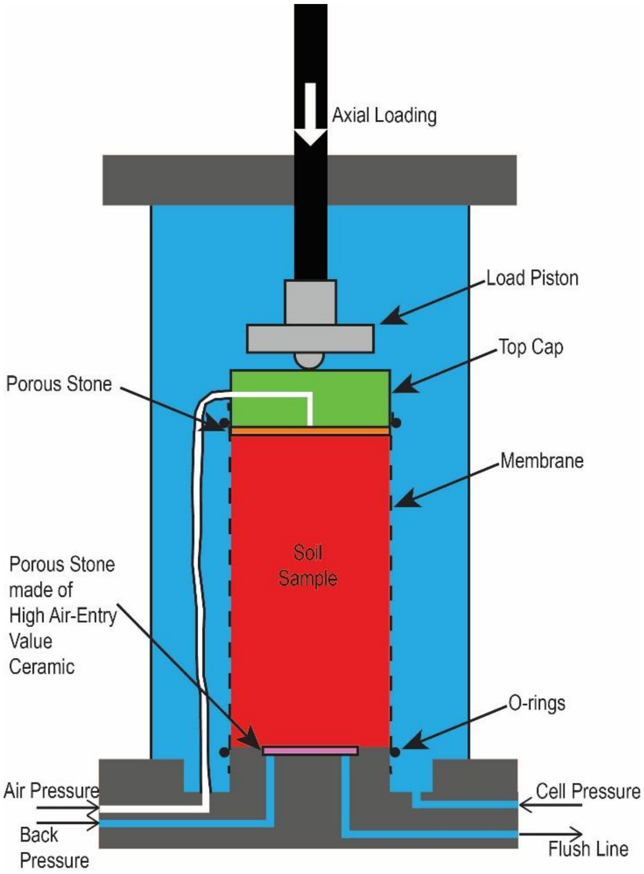

Figure 3- 19: Set-up for Unsaturated Triaxial Tests

All seven UCU tests were tested under various magnitudes of net normal stress and matric suction, a tabulated test plan is shown in Table 3- 10.

Table 3- 10: Consolidated Unsaturated Undrained test plan

ID	Initial Confining Stress, σ_{3i} (kPa)	Initial Air Pressure, u_a (kPa)	Initial Back Pressure, u_w (kPa)	Net Normal Stress, σ_3-u_a (kPa)	Matric Suction, u_a-u_w (kPa)
UCU1	150	60	40	90	20
UCU2	110	80	40	30	40
UCU3	140	110	40	30	70
UCU4	160	130	40	30	90
UCU5	120	100	40	20	60
UCU6	95	65	40	30	25

In UCU tests, a sample is considered failed when the ratio $\frac{\sigma_1-\sigma_3}{\sigma_3-u_w}$ reaches its peak value (Bishop et al., 1960). The corresponding stresses measured at this peak value are defined as the failure stresses. Using Mohr-Coulomb theory, the shear strength of the unsaturated soil (τ_{ff}) can then be calculated as:

$$\tau_{ff}=\frac{\sigma_{1f}-\sigma_{3f}}{2}\cos(\phi') \qquad [3.9]$$

While the net normal stress at the corresponding shear strength is:

$$(\sigma-u_a)_f=\frac{\sigma_{1f}+\sigma_{3f}}{2}-\frac{\sigma_{1f}-\sigma_{3f}}{2}\sin(\phi')-u_{af} \qquad [3.10]$$

Together with the measured matric suction at failure $(u_a-u_w)_f$, effective cohesion (c'), friction angle (ϕ') and unsaturated friction angle (ϕ^b) can be obtained by substituting the failure stresses into the shear strength envelop of unsaturated soils proposed by Fredlund & Rahardjo (1993):

$$\tau_{ff}=c'+(\sigma-u_a)_f\tan\phi'+(u_a-u_w)_f\tan\phi^b \qquad [3.11]$$

The obtained failure stresses are summarized in Table 3- 11, and the change of stresses with axial strain are presented in Figure 3- 20 and Figure 3- 24.

Table 3- 11: Failure Stresses of UCU tests

ID	Final Axial Stress, σ_{1f} (kPa)	Final Confining Stress, σ_{3f} (kPa)	Shear Stress, τ_{ff} (kPa)	Net Normal Stress, $(\sigma-u_a)_f$ (kPa)	Matric Suction, $(u_a-u_w)_f$ (kPa)
UCU1	408.5	150.0	112.5	153.5	1.2
UCU2	283.8	110.0	75.8	87.2	36.5
UCU3	350.7	140.0	91.3	129.1	13.9
UCU4	363.6	160.0	88.7	93.4	53.1
UCU5	307.8	120.0	81.8	89.8	42.5
UCU6	214.0	95.0	51.6	72.0	7.2

Based on the shear strength envelope of unsaturated soils (Eq. 3.11), the obtained effective cohesion is 11.1 kPa; the friction angle is 29.9 degrees; the unsaturated friction angle is 24.2 degrees.

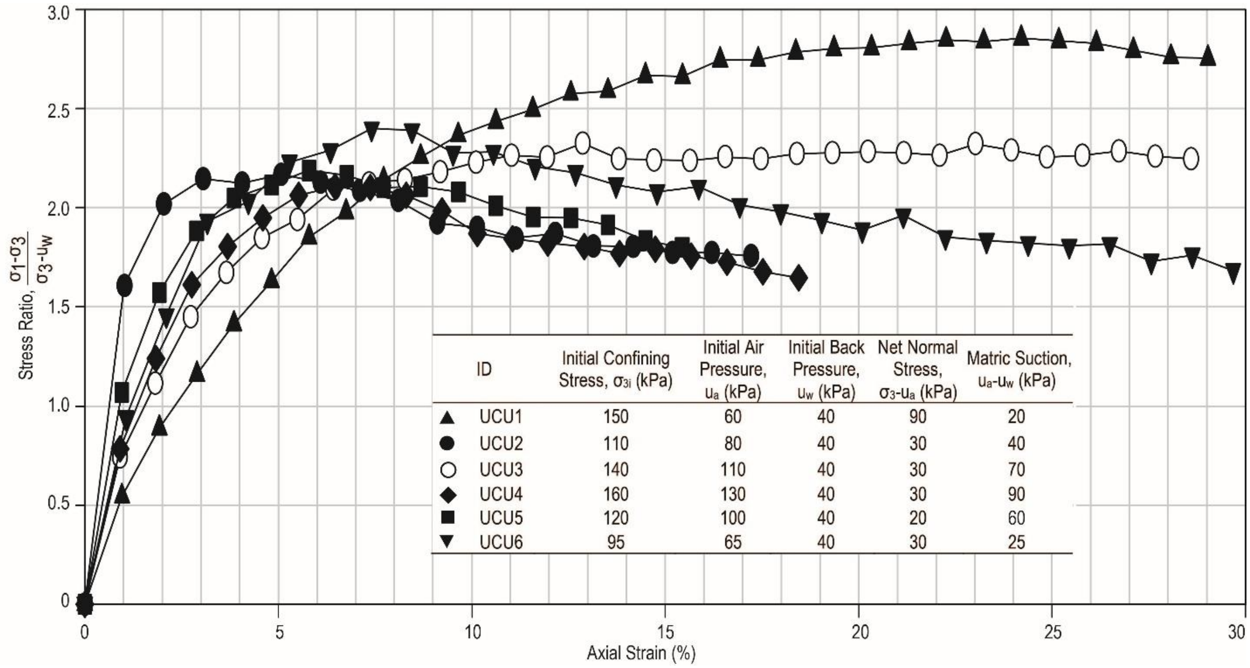

	ID	Initial Confining Stress, σ_{3i} (kPa)	Initial Air Pressure, u_a (kPa)	Initial Back Pressure, u_w (kPa)	Net Normal Stress, σ_3-u_a (kPa)	Matric Suction, u_a-u_w (kPa)
▲	UCU1	150	60	40	90	20
●	UCU2	110	80	40	30	40
○	UCU3	140	110	40	30	70
◆	UCU4	160	130	40	30	90
■	UCU5	120	100	40	20	60
▼	UCU6	95	65	40	30	25

Figure 3- 20: Instantaneous Changes of Stress Ratio during Unsaturated Triaxial Tests

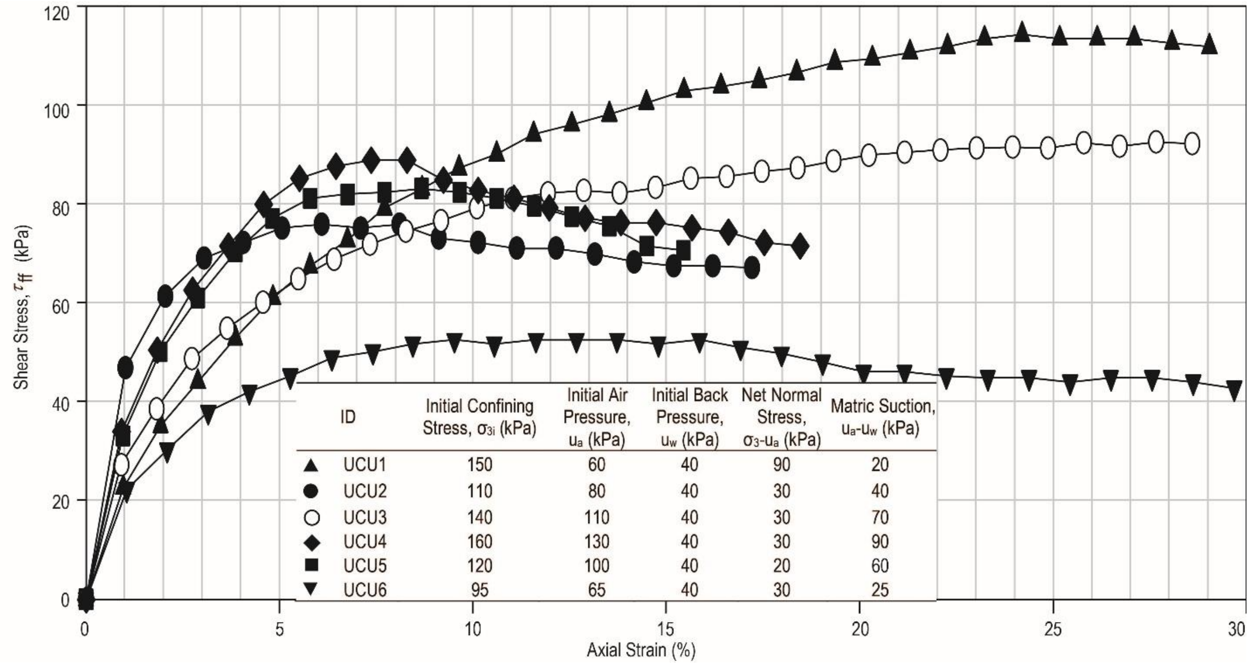

	ID	Initial Confining Stress, σ_{3i} (kPa)	Initial Air Pressure, u_a (kPa)	Initial Back Pressure, u_w (kPa)	Net Normal Stress, σ_3-u_a (kPa)	Matric Suction, u_a-u_w (kPa)
▲	UCU1	150	60	40	90	20
●	UCU2	110	80	40	30	40
○	UCU3	140	110	40	30	70
◆	UCU4	160	130	40	30	90
■	UCU5	120	100	40	20	60
▼	UCU6	95	65	40	30	25

Figure 3- 21: Instantaneous Changes of Shear Stress during Unsaturated Triaxial Tests

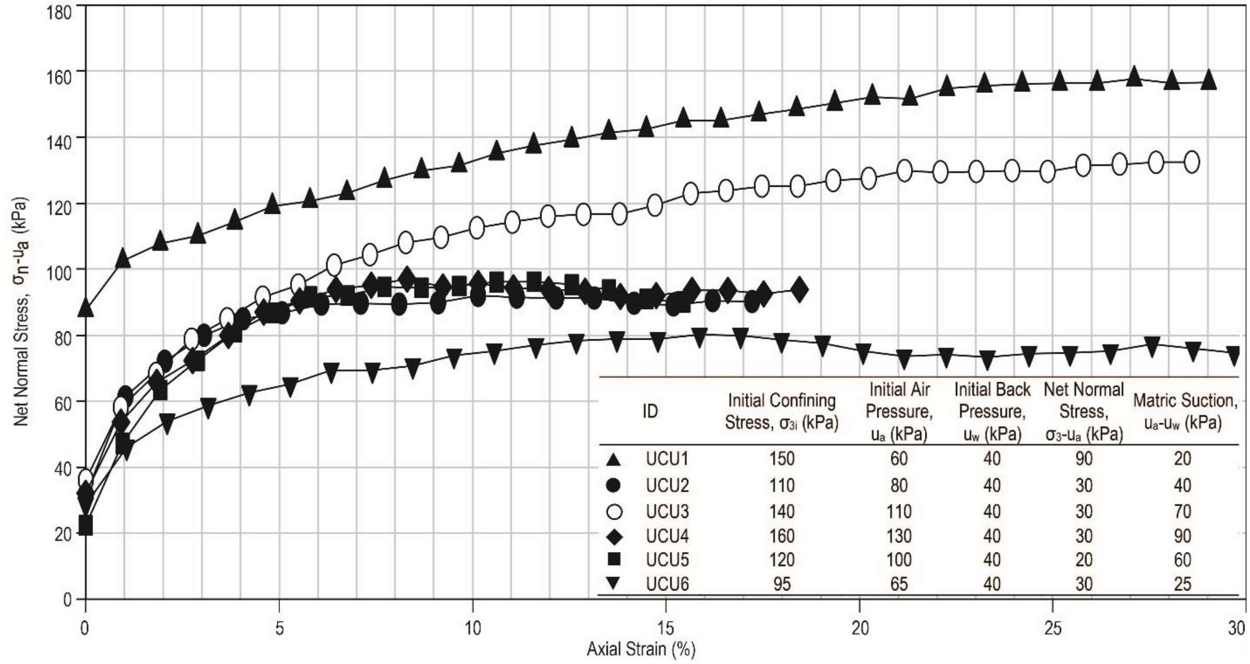

Figure 3- 22: Instantaneous Changes of Net Normal Stress during Unsaturated Triaxial Tests

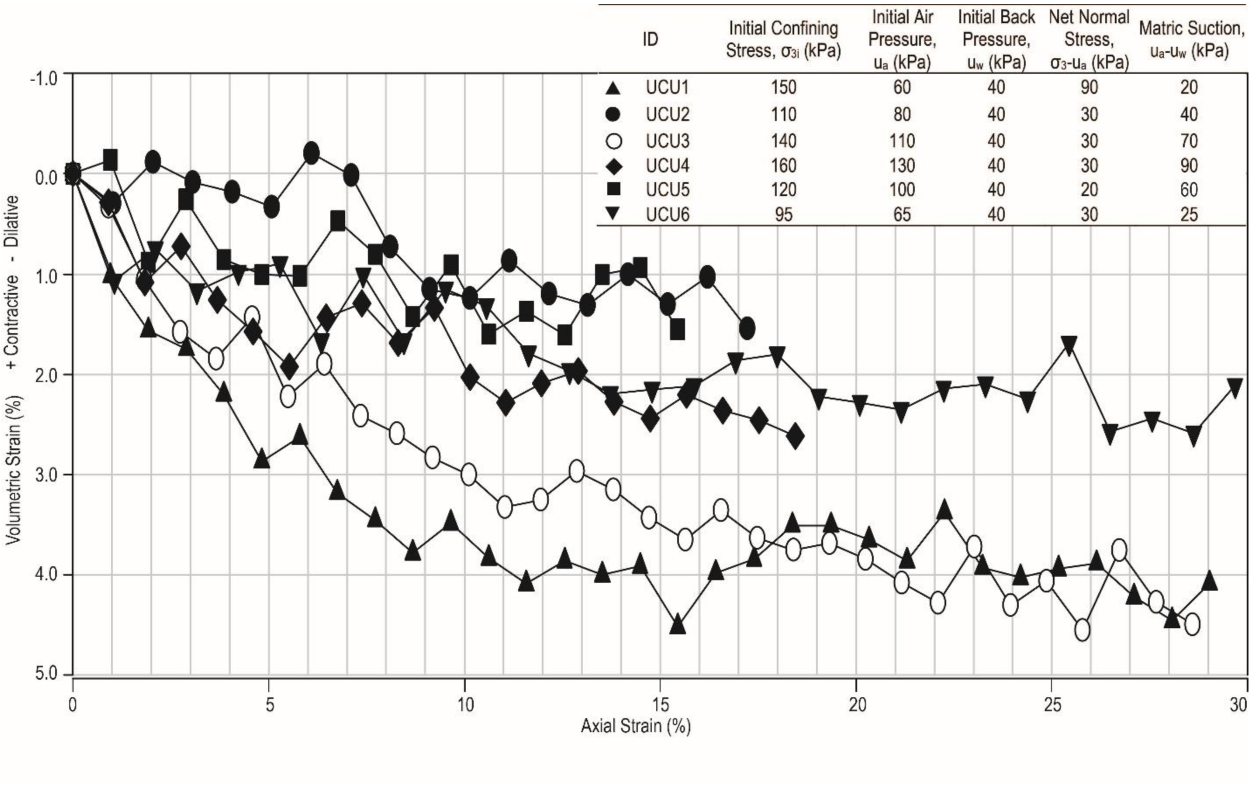

Figure 3- 23: Instantaneous Volumetric Changes during Unsaturated Triaxial Tests

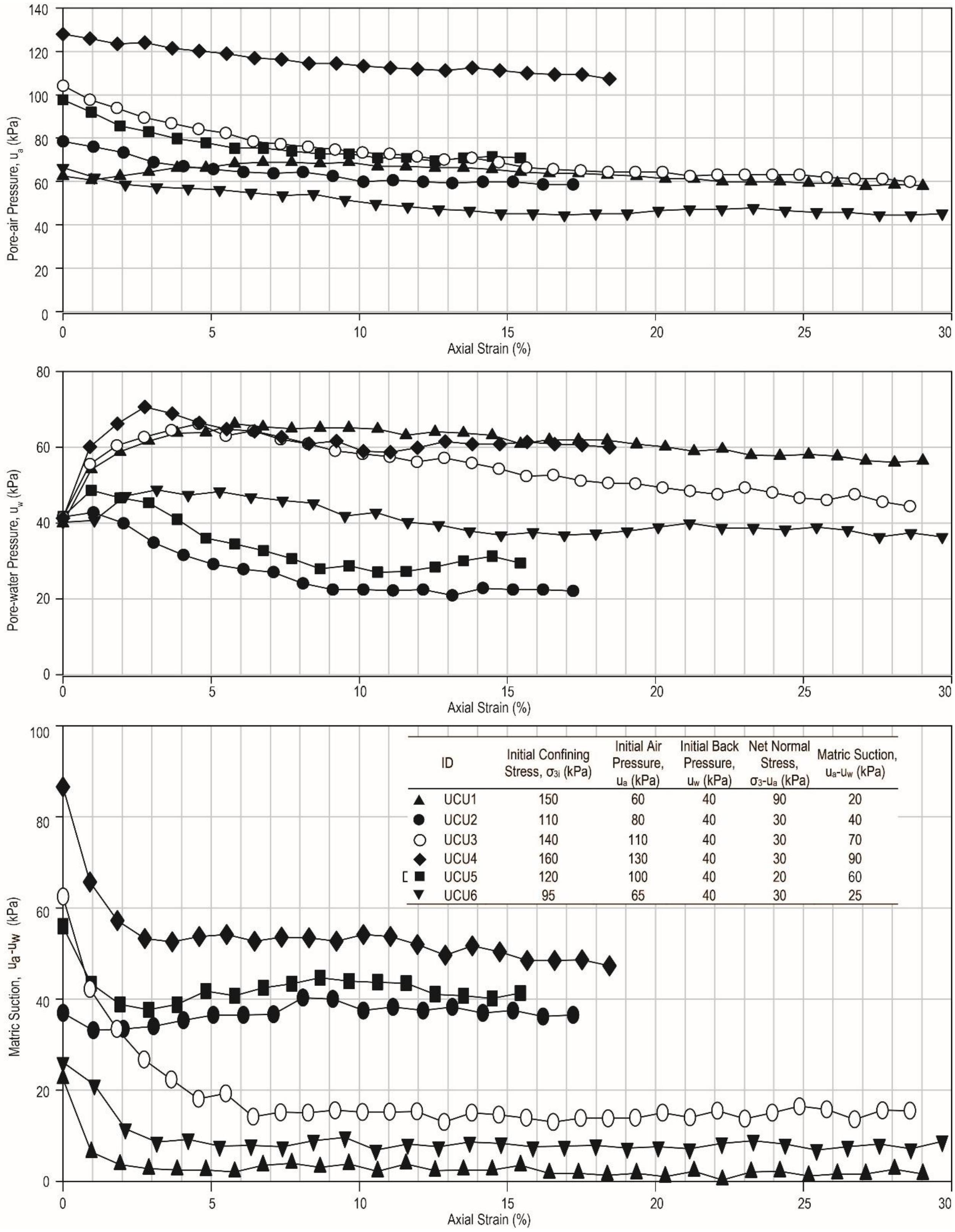

	ID	Initial Confining Stress, σ_{3i} (kPa)	Initial Air Pressure, u_a (kPa)	Initial Back Pressure, u_w (kPa)	Net Normal Stress, σ_3-u_a (kPa)	Matric Suction, u_a-u_w (kPa)
▲	UCU1	150	60	40	90	20
●	UCU2	110	80	40	30	40
○	UCU3	140	110	40	30	70
◆	UCU4	160	130	40	30	90
■	UCU5	120	100	40	20	60
▼	UCU6	95	65	40	30	25

Figure 3- 24: Instantaneous Changes of Pore Pressures during Unsaturated Triaxial Tests

References

ASTM, D. (1994). 854 92. Standard test method for specific gravity of soils. Annual Book of ASTM Standards, 4, 80-3.

ASTM, D. (2012). 4318-10.“. Standard Test Methods for Liquid Limit, Plastic Limit, and Plasticity Index of Soils.” Annual book of ASTM standards, ASTM international, Philadelphia.

ASTM. (2016). Standard test method for particle-size distribution (gradation) of fine-grained soils using the sedimentation (hydrometer) analysis. D7928-16.

ASTM (2004). ASTM D4767,“. Standard Test Method for Consolidated Undrained Triaxial Compression Test for Cohesive Soils”, Annual Book of ASTM Standards, 913-925.

Becker, D. E., et al. (1987). Work as a criterion for determining in situ and yield stresses in clays. Canadian Geotechnical Journal, pp. 549-564.

Bishop, A., & Donald, I. (1961). The experimental study of partly saturated soil in the triaxial apparatus. Proceedings of the 5th international conference on soil mechanics and foundation, 1, pp. 13-21. Paris.

Bishop, A., Alpan, I., Blight, G., & Donald, I. (1960). Factocs Controlling the Shear Strength of Partly Saturated Cohesive Soils. ASCE Res. Conf. Shear Strength of Cohesive Soils, (pp. 503-532). University of Colorado, Boulder.

Bolton, M. (1986). The strength and dilatancy of sands. Geotechnique, 16, 65-78.

Chantawarangul, K. (1983). Comparative study of different procedures to evaluate effective stress strength parameters for partially saturated soils. Thailand: Asian Institute of Technology.

Fredlund, D., & Houston, S. (2013). Interpretation of soil-water characteristic curves when volume change occurs as soil suction is changed. Advances in Unsaturated Soils, 15-31.

Fredlund, D., & Rahardjo, H. (1993). Soil mechanics for unsaturated soils. John Wiley & Sons.

Fredlund, D.G.; Xing, A. (1994). Equations for the soil-water characteristic curve. Canadian Geotechnical Journal(31), 533-546.

Fredlund, M.D.; Wilson, G.W.; Fredlund, D.G. (2002). Representation and estimation of the shrinkage curve. Third Internation Conference on Unsaturated Soils, 145-149.

Hilf, J. (1956). An investigation of pore water pressure in compacted cohesive soils. Bureau of Reclamation (US).

Ho, D., & Fredlund, D. (1982). A Multistage Triaxial test for unsaturated soils. Geotechnical Testing Journal.

Houlsby, G. (1991). How the dilatancy of soils affects their behaviour. Oxford: University of Oxford, Department of Engineering Science.

Ladd, C., & Foott, R. (1974). New design procedure for stability of soft clays. J. Geotechn. Eng. Div. ASCE, 100(GT7), 763-786.

Lambe, T., & Whitman, R. (1968). Soil Mechanics. New York: John Wiley & Sons.

Leong, E., Nyunt, T., & Rahardjo, H. (2013). Triaxial Testing of Unsaturated Soils. Multiphysical Testing of Soils and Shales, 33-44.

Muir Wood, D. (1990). Soil Behaviour and Critical State Soil Mechanics. 1990: Cambridge University Press.

Rowe, P. (1962). The stress-dilatancy relation for static equilibrium of an assembly of particles in contact. Proc. R. Soc., A269, 500-527.

Schofield, A., & Wroth, P. (1968). Critical State Soil Mechanics. Cambridge: Cambridge University.

Vermeer, P., & De Borst, R. (1984). Non-Associated Plasticity for Soils, Concrete and Rock. Heron, 29(No. 3).

Vermeer, P., & Schanz, T. (1996). Angles of friction and dilatancy of sand. Geotechnique, 145-152.

Chapter 4. Cone Penetration Testing in Unsaturated Silt with Matric Suction Measurements

by Jonathan M. Wong[1] *and David Elwood*[2]

[1] MSc Candidate, Department of Civil, Geological and Environmental Engineering, University of Saskatchewan, Saskatoon, SK, Canada S7N 5B4. jmw932@mail.usask.ca

[2] Assistant Professor, Department of Civil, Geological and Environmental Engineering, University of Saskatchewan, Saskatoon, SK, Canada S7N 5B4. david.elwood@usask.ca

Corresponding author

David Elwood
Department of Civil, Geological and Environmental Engineering, University of Saskatchewan
Saskatoon, SK, Canada S7N 5B4
Email: david.elwood@usask.ca
Tel: +1 (306) 966-3246

4.1 Preface

All work reported in this chapter, including design of the experimental program, implementation of the experiments, review of the literature, development of the theoretical framework, analysis and discussion of the results and writing of the text, has been carried out by the MSc. student. As supervisor, Dr. David Elwood reviewed all parts of the work.

A version of this chapter has been published with the following citations:

1. Wong, J. M., Elwood, D. (2018). Cone Penetration Testing in Unsaturated Silt with Matric Suction Measurements. Journal of Geotechnical and Geoenvironmental Engineering (In the process of publication).

This chapter may or may not contain additional details found in the published manuscripts.

4.2 Introduction

A cone penetration test (CPT) is an *in situ* testing method used to determine the geotechnical properties of soils and is conducted by pushing an instrumented metallic cone (piezocone) into the ground at a fixed rate. Physical properties of the subsurface can be estimated empirically using the load cell and friction sleeve readings of the piezocone. *In situ* pore-water pressure (u_0) and consolidation parameters of the subsurface can also be evaluated by conducting a pore pressure dissipation (PPD) test, which takes place when penetration is temporarily paused during advancement.

Despite the rapid development of empirical correlations, CPT interpretations have mostly been applied to saturated or completely dry soils (Robertson & Campanella, 1983a,b) in which the pore-water pressure (u) is known. For two reasons, very few publications report the use of CPTs to evaluate the properties of unsaturated soils. First, most existing empirical correlations were formulated from CPT results in saturated soils, which brings into question their applicability to unsaturated soils. Because matric suction is not considered when deriving these empirical correlations, the impact of matric suction on subsurface characterization is not known. Second, most pore-water pressure transducers installed on piezocones can measure matric suction (negative pore-water pressure) but such readings will be inaccurate if the porous stone is desaturated (Campanella & Robertson, 1988), which can occur either during dilation of an over-consolidated soil or through contact with an unsaturated soil. Desaturation of the porous stone will occur because the matric suction introduces a hydraulic gradient that draws fluid out from the porous stone, resulting in the formation of cavitation nuclei and a potentially discontinuous liquid phase. This can primarily occur during cessation of cone advancement for either a PPD test or for shear wave velocity measurements. Desaturation is not necessarily detrimental to the overall function of the cone during advancement through nearly saturated soils because the kinematic pore-water pressures will force the porous stone to saturation. However, if the soil is highly dilatant (resulting in high negative pore-water pressures during cavity expansion) or has a natural water content near the centre of the soil water characteristic curve (SWCC) (at an approximate effective degree of saturation of 50%) then the porous stone might not re-saturate upon restarting cone advancement. Furthermore, pore-water pressure transducers that record negative pore-water pressures can appear to function as designed without obviously desaturating. This can be misleading and give a false sense of accuracy, leading to misuse of data during the interpretation phase.

Tensiometers can be used to directly measure the matric suction of unsaturated soils, provided the induced negative pore-water pressures are less than atmospheric pressure. Tensiometers are water columns equipped with a vacuum pressure transducer and a porous stone made of high-air-entry-value (HAEV) ceramic, which prevents pore-air from entering its pore space and allows for the free passage of water into or out of the instrument depending on the water potential of the soil.

The objective of this work was to conduct calibration chamber tests to investigate the applicability of CPT correlations in an unsaturated, moderately dilatant silt. The experiments were conducted by advancing a NOVA piezocone (CPTu) within a cylindrical chamber filled with silt, with cone resistance, sleeve friction, and pore-water pressure at the U2 position (cone shoulder) recorded. Four jet-fill type tensiometers equipped with strain gauge vacuum transducers were installed inside the chamber to various depths to record the change of negative pore-water pressures (matric suction) prior to, during, and after cone penetration. Penetration was halted once the piezocone reached the target depth, and a PPD test immediately conducted. The results demonstrate how to extend CPT applications to unsaturated soils with the use of tensiometers.

4.3 Methodology

4.3.1 The Test Chamber

The chamber (Figure 4-1) used in this experiment was a high density polyethylene (HDPE) corrugated pipe measuring 0.9 m diam. × 1.63 m high × 6.4 mm thick with a corrugated thickness of 63.5 mm. The bottom rim of the pipe sat in a groove milled into a 38.1-mm thick PVC base plate. The groove was sealed with plumber's wax to ensure water tightness.

Prior to deposition of the silt, a layer of silicone lubricant followed by a thin plastic film was applied to the inner wall of the chamber. Such preparation works were intended to reduce the interface friction between the chamber wall and the silt, as suggested by Rieke & Chilingarian (1974). The top face of the chamber was also covered by a plastic film immediately after soil deposition and cone penetration to reduce the loss of water content through evaporation.

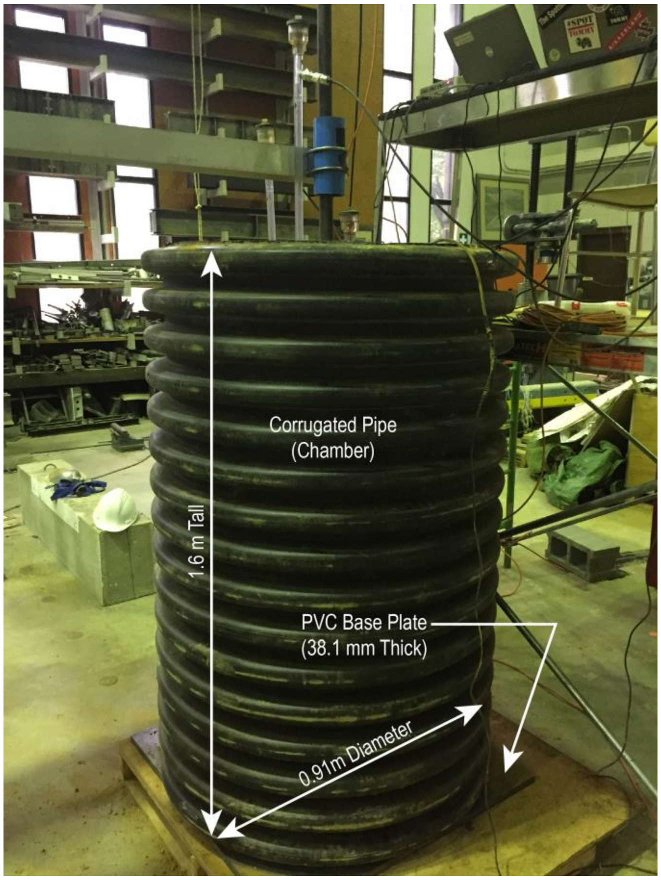

Figure 4- 1: Photo of test chamber setup

Physical properties of the silt were characterized in Chapter 3. The silt was first pulverized and mixed to a specific water content (ranging from 14.5 to 35% gravimetric water content; Table 4-1) using a concrete mixer, then deposited into the chamber and compacted by hand in 10-cm lifts. Each lift was compacted by dropping a tamper (square base, length 254 mm, weight 5.7 kg) 30 times from a height 1 m above the surface. The compaction effort involved was 25.6 kJ per m^3 of soil, which is equivalent to 1% compaction effort for a modified Proctor test. The relative density of the silt in the chamber tests ranged from 8 to 44%.

4.3.2 Tensiometers

Tubular-Plexiglas tensiometers, featuring a HAEV ceramic tip on one end and a jet-fill type water reservoir and strain-gauge type vacuum pressure transducer on the other (Figure 4-2), were used to measure the water potential (matric suction) of the unsaturated soils.

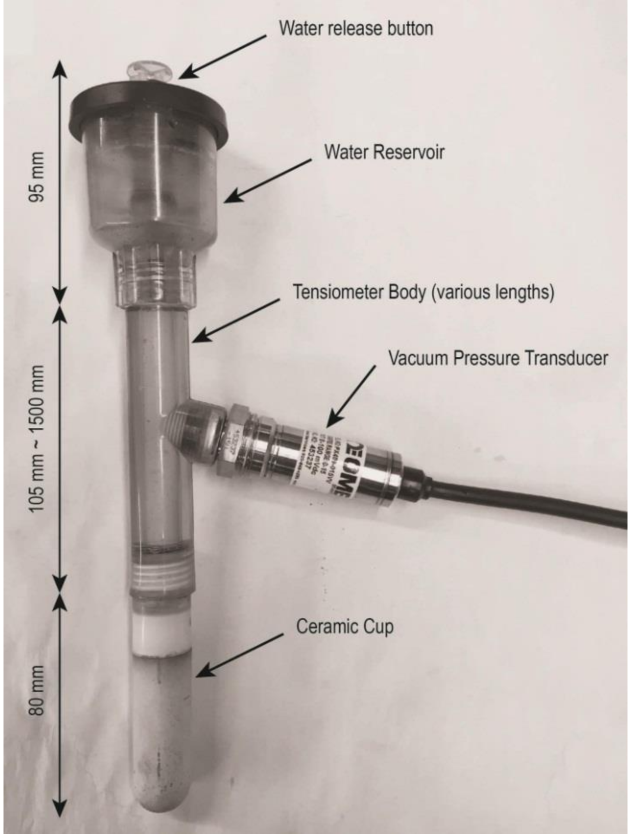

Figure 4- 2: Jet-fill type tensiometer

Before installing the tensiometers into the unsaturated soil, they were first filled with de-aired water and the ceramic tip saturated. Saturation was achieved by immersing the ceramic cup into de-aired water inside a vacuum chamber for a minimum of 24 h. Once all components of the a given tensiometer were saturated, it was installed into the unsaturated soil. To accurately measure the water potential (matric suction), the ceramic tip must be in intimate contact with the surrounding soil. Tensiometers (22-mm diameter) were inserted into 18-mm diameter holes of the test chamber drilled with an auger bit to the desired test interval.

Because the ceramic tip was saturated, the water potential of the unsaturated soil is lower than within the tensiometer. The potential difference induces a tensile stress on the water within the tensiometer, which is measured by the strain-gauge type vacuum pressure transducer at a rate of 1 Hz. However, when the water within the tensiometer is under tensile stress, air bubbles can form as a result of cavitation nuclei, provided the water potential of the soil is less than atmospheric pressure. If air bubbles were observed within the water column, the water release button on the jet-fill reservoir was pressed and the negative pressure within the water column was vented. The tensiometers were left in place until the matric suction measurements suggested equilibrium with the soil was achieved and no air bubbles were visible within the tensiometer. Depending on the water potential of the soil, the time to reach equilibrium was up to 24 h. The ceramic tips used were rated at 100 kPa (1 ATM) air-entry value. This rating represents the maximum allowable difference in water potential a saturated ceramic tip can withstand before intrusion of air into the pore space of the ceramic. The rating of the ceramic tip should be greater than or equal to the residual suction of the unsaturated soil.

One tensiometer was buried near the centerline of the chamber and used to record the matric suction change at the tip of the piezocone in the wet zone (TS1), and three tensiometers were inserted away from the centerline at different radii to record the matric suction change near the piezocone shoulder in the wet zone (TS2), dry zone (TS3), and the assumed elastic region (TS4) (Table 4-1; Figure 4-3). The locations of these tensiometers were chosen such that those measuring the matric suction within the plastic zone (TS1, TS2, and TS3) were within an ~80 mm radius of the pore pressure transducer (Burns & Mayne, 1998a) and the one measuring the matric suction within the assumed elastic zone (TS4) was at least 200 mm from the wall of the chamber.

4.3.3 Experiments

Four chamber tests were conducted: Test 1 with silt at one water content and Tests 2 to 4 with two layers of silt at different water contents (Table 4-1). The drier layer overlaid the wetter layer to prevent gravity drainage of water. After compacting the last lift of each silt layer, a soil sample was extracted using a 25.4-mm diameter Shelby tube. The bulk density and gravimetric water content of the soil samples were measured at depths throughout each layer.

The advancement rate of the piezocone was a constant 15 mm/s in accordance with ASTM D5778. Cone resistance, sleeve friction, matric suction, and pore-water pressure were recorded during penetration. A pore-water PPD test was conducted in each silt layer when the piezocone reached the depth of the tensiometers. Every PPD test was conducted until the tensiometer readings (matric suction) recovered to initial values.

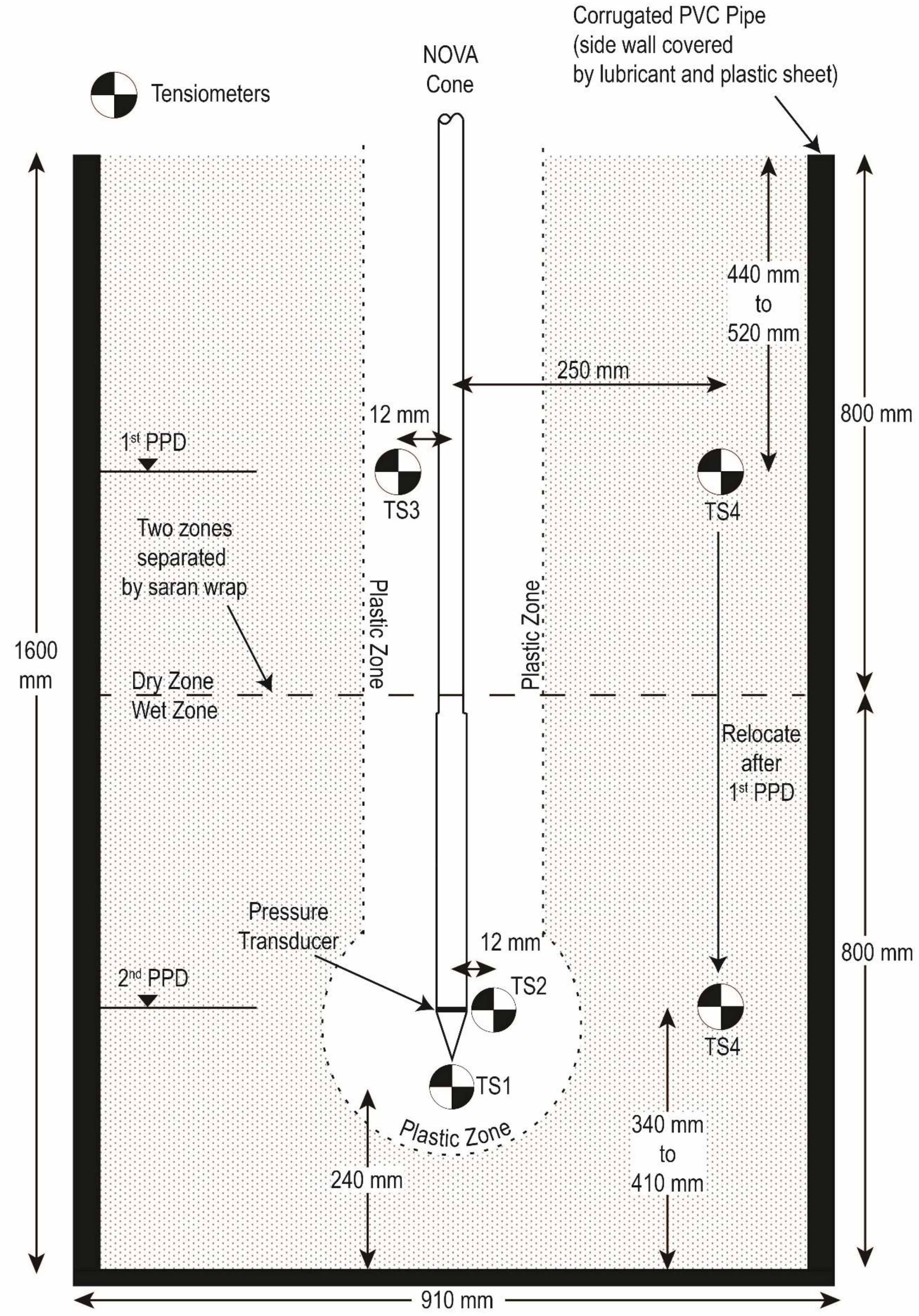

Figure 4- 3: General layout of chamber test

Table 4- 1: Test plan for chamber tests

	Test 1	Test 2		Test 3		Test 4	
		Dry Zone	Wet Zone	Dry Zone	Wet Zone	Dry Zone	Wet Zone
Bulk density (kN/m^3)	19.0	13.0	18.5	18.0	18.5	14.0	18.0
Degree of saturation	100	32.3	89.9	75.0	85.0	36.4	89.2
Void ratio	0.93	1.22	0.90	0.87	0.86	1.26	1.00
Gravimetric water content (%)	35	14.5	30	24	27	17	33
Matric suction (kPa)	9.4	70.7	20.4	24.6	16.0	53.5	14.1
PPD test depth (m)	1.24	0.467	1.26	0.52	1.23	0.44	1.19
Relative density (%)	37	8	40	43	44	4	30

4.3.4 Consideration of boundary conditions

Results of a CPT conducted in a test chamber might differ significantly from those conducted in the field due to different boundary conditions, which are particularly difficult to quantify as they can vary with many factors. Parkin & Lunne (1982) report that boundary effects are negligible provided the chamber diameter is at least 50 times larger than the cone penetrometer for tests conducted in a dense sand (relative density ~90%) and 20 times larger for tests conducted in a loose sand (relative density ~30%). The chamber size used for experiments described herein was 25 times larger than the cone diameter (3.6 cm), meaning boundary effects are possible; in addition, boundary effects are expected because the silt specimen was compacted to a relative density higher than 20% (Table 4-1) (Parkin & Lunne, 1982). Yu & Mitchell (1998) state that the rigidity of the chamber wall can also affect cone penetrometer readings. For a chamber with flexible walls (constant pressure), the cone resistance measured tends to be lower than values measured in the field; however, a higher cone resistance is usually measured in chambers with rigid walls (zero deformation). Our chamber wall was reinforced with corrugated ribs, so it is reasonable to assume a zero-deformation boundary condition on the sidewall and the bottom face of the chamber (i.e., a Type B2 chamber; Parkin & Lunne, 1982) and that cone resistance values obtained in the chamber tests might be higher than under field conditions. Overall, this research did not quantify boundary effects but efforts were made to minimize them when possible. Pore-water pressure changes measured in the tensiometer installed within the assumed elastic region suggest negligible measured change, with the wall treatment and chamber size appearing sufficient to minimize any boundary effects.

4.4 Results and Discussion

4.4.1 In-situ SWCC

Fredlund & Houston (2013) report the SWCC can differ if the porosity of a soil sample changes. This suggests a hysteresis between laboratory and *in situ* SWCC data due to differences in sample preparation (and, hence, different porosities). To obtain the *in situ* SWCC, tensiometers were used to measure the matric suction after the unsaturated silt was deposited into the chamber. The bulk density and gravimetric water content of the silt layer were measured from the silt sample extracted after compaction, with the degree of saturation and void ratio calculated. The degree of saturation values were then plotted against the matric suction value, and curve fitted (Fredlund & Xing, 1994) to obtain the *in situ* SWCC. Figure 4-4 indicates the *in situ* SWCC (tensiometer measurements) is shifted to the right compared to the laboratory SWCC (pressure plate cell), meaning the soil is able to sustain higher suction before desaturation. As a result, the air-entry value also shifted from ~9.5 kPa (lab condition) to ~15 kPa (*in situ* measurement).

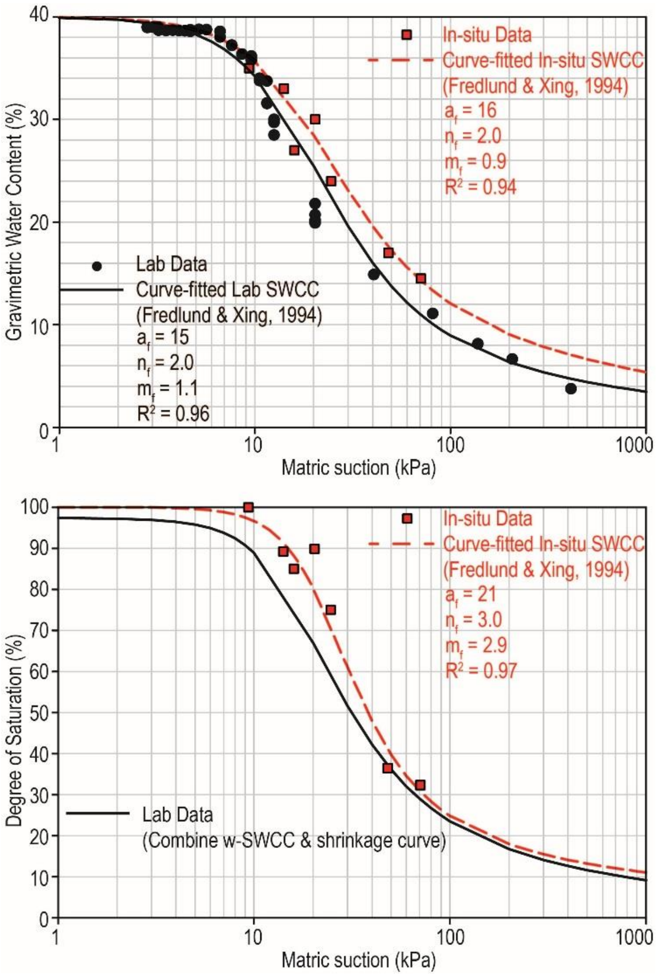

Figure 4- 4: Lab and in situ SWCC

4.4.2 Correction for Cone Resistance & Sleeve Friction

Due to the different geometry of the friction sleeve and the cone tip load cell, cone resistance could be affected by excess pore-water pressure, i.e., the unequal end area effect (Campanella et al., 1986). A correction factor can be applied to the measured cone resistance (q_c) to obtain a corrected cone resistance value (q_t):

$$q_t = q_c + u_2(1-a)\,, \tag{4.1}$$

where u_2 is the excess pore-water pressure measured by the pore pressure transducer located at the cone shoulder (referred to as the u_2 location) and a is the net area ratio, which is a specific calibration value for each instrument and typically ranges between 0.7 and 0.85 (0.842 herein, as determined by the manufacturer).

A correction factor for sleeve friction (f_s) is usually required, especially for 15-cm^2 cone penetrometers; however, the cone used in the chamber tests has a cross-sectional area of 10 cm^2 so the correction is negligible (Robertson & Cabal, 2015). Furthermore, because no pressure transducer was installed at the u_3 position (top of friction sleeve), the method to obtain a correction factor for the sleeve friction reading of a 10-cm^2 cone was limited.

The q_c and f_s readings, which respectively represent the stiffness and shaft friction of the soil, were obtained through the load cell and friction sleeve on the piezocone and recorded continuously with depth during penetration. Note that soft clay tends to have a low value of cone resistance and a high value of sleeve friction while sand tends to have a high value of cone resistance and a low value of sleeve friction.

Matric suction plotted against average values of f_s (Figure 4-5a) and q_t (Figure 4-5b), along with the *in situ* SWCC, show that the q_t measured in unsaturated soils generally tends to increase with matric suction whereas f_s attains a maximum value near the air-entry value (AEV) of the soil. These results are expected as cone resistance is known to vary with the shear strength of the soil (Nash & Duffin, 1982; Lunne et al., 1986; Aas et al., 1986). The shear strength of the unsaturated soil also increases with increasing matric suction (Bishop, 1959; Fredlund & Rahardjo, 1993), and therefore it stands to reason that the cone resistance would also increase (Yang & Russell, 2015). Detailed continuous measurement of cone resistance and sleeve friction with depth for the four chamber tests are available in Appendix 4A.

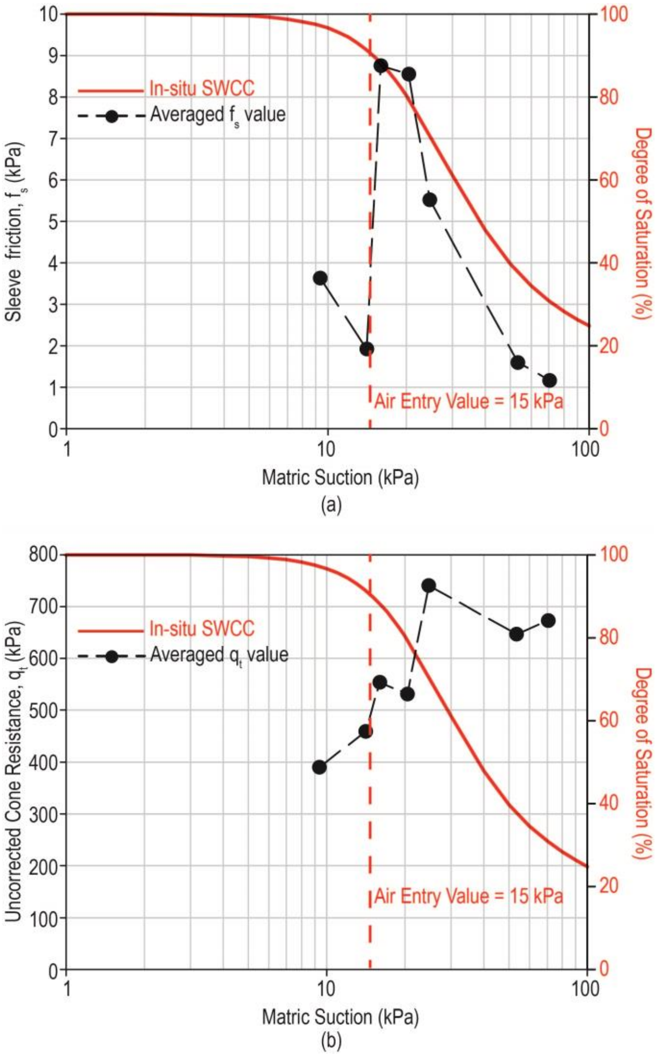

Figure 4- 5: Matric suction vs. (a) average sleeve friction and (b) average corrected cone resistance

4.4.3 Pore Pressure Dissipation Test

Figure 4-6 presents the PPD curves obtained for all chamber tests (individual interpretations of each PPD are provided in Appendix 4C). The pore pressure transducer does not always record a change of pore pressure during the PPD tests; specifically, the pore pressure transducer readings show little to no change when the *in situ* suction is above ~24.6 kPa (degree of saturation ≤ 75%).

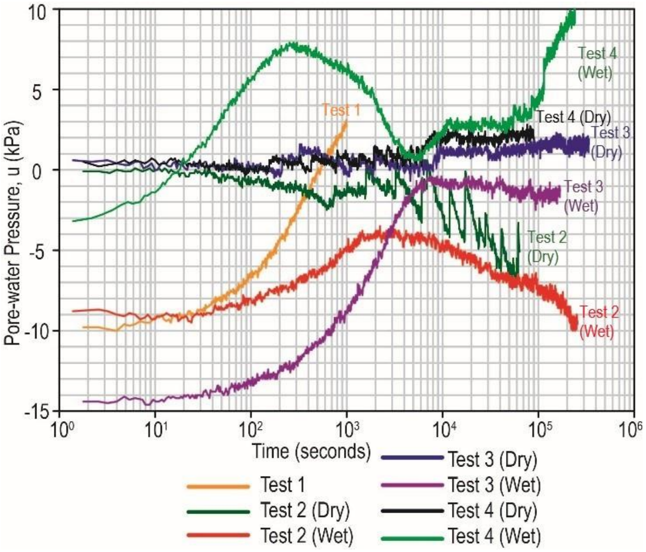

Figure 4- 6: PPD curves of chamber tests

For PPDs that recorded a dissipating pressure, the trend of the curves is an exponential increase in pore pressure with time. Once the pore pressure reaches a maximum value, it either remains constant (Test 1 and Test 3) or decreases with time (Test 2 and Test 4). However, the decrease in pore pressure after peak values is likely the result of a hydraulic head difference between the wet and dry zones. Hence, the pore pressures are assumed to be fully recovered at the peak value. A complete PPD test in granular soil might only takes several minutes but in fine-grained soils could take days to complete. PPD tests in fine-grained soil are therefore often terminated at t_{50} (when half the excess pore-water pressure has dissipated). Empirical correlations (described below) and t_{50} values determined here were used to estimate hydraulic properties of the subsurface, including the hydraulic conductivity (k) and coefficient of consolidation (c_h) (Table 4-2).

Table 4- 2: t50 values and estimated hydraulic properties

Test	Matric suction (kPa)	q_t-σ_{v0} (kPa)	From PPD results			From tensiometer results		
			t_{50} (s)	k ($\times 10^{-9}$ m/s)	c_h ($\times 10^{-6}$ m^2/s)	t_{50} (s)	k ($\times 10^{-9}$ m/s)	c_h ($\times 10^{-6}$ m^2/s)
Test 1	9.36	376.5	426	8.30	2.63	415	8.52	2.70
Test 2 Wet Zone	20.4	530.1	628	4.00	1.78	176	14.3	6.36
Test 3 Wet Zone	15.96	552.5	1305	1.85	0.86	73	33.0	15.3
Test 4 Wet Zone*	14.1	457.9	40	73.1	28.1	752	3.87	1.49

*Tensiometer damaged by piezocone; leakage might have affected PPD test readings. Tensiometer t_{50} value was estimated based on other tensiometers.

4.4.4 Tensiometer Readings

Similar to the results of the PPD tests, tensiometer measurements were mostly unresponsive to cone penetration when the degree of saturation of the soil was ≤ 75% (matric suction > 25 kPa). The lack of response might also be a function of the loose nature of the soil and not necessarily reflective of the negative pore-water pressure response in the soil. A drastic change of tensiometer readings with cone insertion was observed when the degree of saturation of the soil was ≥ 75% (matric suction < 25 kPa). As demonstrated in Figure 4-7 as an example (Test 3), matric suction slightly increases (~1 to 2 kPa) as the piezocone approaches the depth of the tensiometers. This increase in suction is immediately followed by a sharp decrease in matric suction until the shoulder of the piezocone reaches the depth of the tip of the tensiometer. The matric suction measured at this depth equals the excess pore-water pressure generated by cone penetration measured at the cone shoulder (u_2) position. Penetration is then halted for the PPD test, and the matric suction slowly rises to its initial value. Full recovery of matric suction was generally observed within 3 to 5 h of the beginning of a PPD test (see t_{50} values in Table 4-2). Individual tensiometer readings are presented in Appendix 4D.

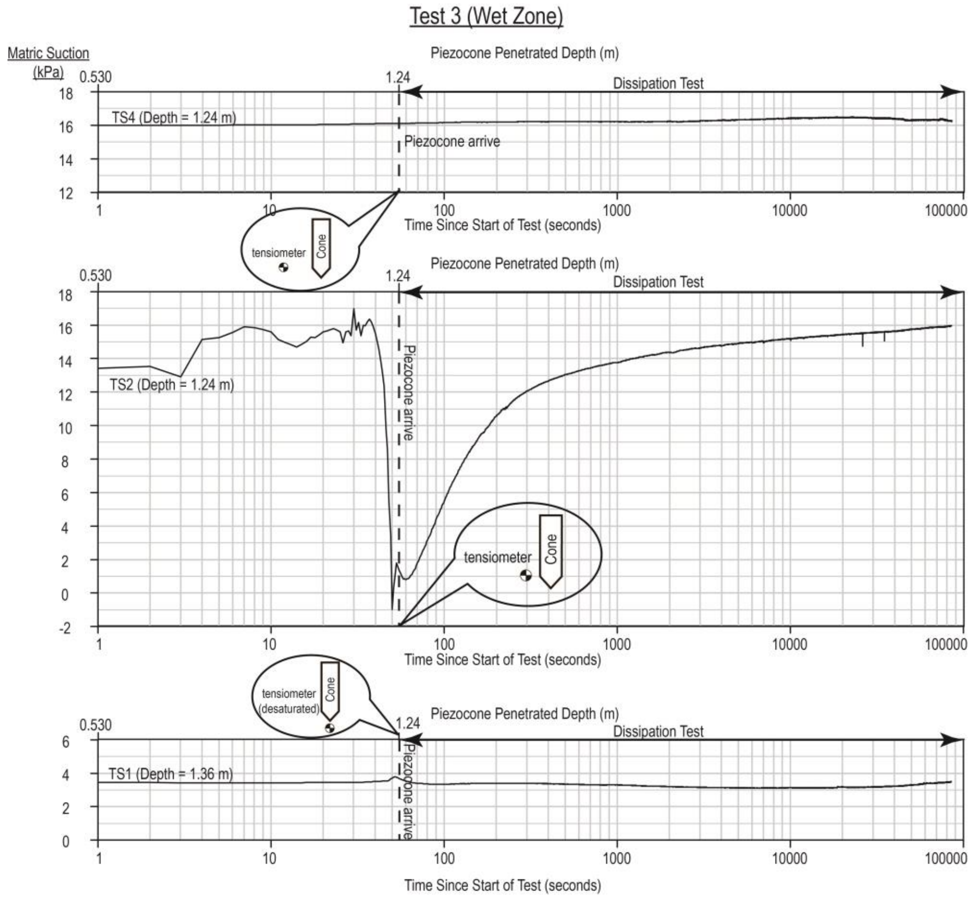

Figure 4- 7: Two types of matric suction responses (Test 3)

4.4.5 Estimation of Hydraulic Properties

Typically, the hydraulic properties of the subsurface (k and c_h) can be evaluated using the dissipation rate from the PPD test. The following partial differential equation, derived from cavity expansion theory (Torstensson, 1977), can be used to relate the dissipating pore-water pressure to distance and time from the piezocone:

$$\frac{\partial u}{\partial t} = c_h\left(\frac{\partial^2 u}{\partial r^2} + \frac{\beta}{r}\frac{\partial u}{\partial r}\right), \qquad [4.2]$$

where t is the time of dissipation; r is the radial distance from piezocone (r_0 = radius of piezocone); and β is the cavity expansion coefficient (β =1 for cylindrical cavity; β =2 for spherical cavity).

Eq. 4.2 was later re-written as a Terzaghi type consolidation equation (Campanella & Robertson, 1988; Houlsby et al., 1989) to calculate the coefficient of consolidation using PPD data:

$$T = \frac{c_h t}{r_0^2 \sqrt{I_R}} , \qquad [4.3]$$

where t is the time to reach a certain degree of consolidation ($\Delta u/u_0$); r_0 is the radius of the piezocone (1.8 cm); T is a time factor that depends on degree of consolidation, tip geometry of piezocone, and porous element location; and I_R is the rigidity index ($I_R = G/S_u \approx 200$ for our red silt). Torstensson (1977) realized that $\Delta u/u_0$ is related to both I_R and the quantity r_o^2/c_h in Eq. 4.3. Using the method of finite differences, Teh & Houlsby (1991) created a tabulated solution to obtain T. Eq. 4.3 is also known as the t_{50} method for estimating the horizontal coefficient of consolidation of the soil, which uses the initial pore-water pressure (u_0) (estimated from CPT soundings) and time to dissipate 50% of pore-water pressure (obtained from PPD test). Note that the hydraulic conductivity of unsaturated soil varies with both degree of saturation and void ratio (Fredlund & Rahardjo, 1993), and is always lower than for saturated soils. Therefore, the typical t_{50} method is only applicable to unsaturated soils at low suction (close to air-entry value) because no dissipation response in evident at higher matric suction (>25 k).

Burns & Mayne (1998b) proposed an empirical correlation to coefficient of volume compressibility (m_h) and *k* using q_t:

$$k = \frac{c_h \gamma_w}{1/m_h} = \frac{c_h \gamma_w}{8.25(q_t - \sigma_{vo})} , \qquad [4.4]$$

where σ_{v0} is the vertical total stress and γ_w is the unit weight of water. Eq. 4.4 was developed based on the database of cone penetration tests in saturated soils, assuming the constrained modulus ($1/m_h$) is 8.25 times the net cone resistance (q_t-σ_{v0}). While unsaturated soils are generally more compressible than saturated soils (due to the compressibility of air filled voids), no evidence indicates the degree of saturation to which this equation is applicable for unsaturated soils. Using Equations 3 and 4, the *k* and c_h of the unsaturated soils were estimated using the t_{50} values obtained from the PPDs and tensiometers (Table 4-2).

In addition to empirical correlations derived from cavity expansion theory, the *in situ* SWCC can also be used to estimate the hydraulic conductivity of unsaturated soil. Brooks & Corey (1964) proposed the following equations, in conjunction with a pore-size distribution index (λ), to estimate the unsaturated hydraulic conductivity:

$$\begin{aligned} k_{unsat} &= k_{sat}\left(\frac{AEV}{u_a - u_w}\right)^{2+3\lambda} && for\ u_a - u_w > AEV \\ k_{unsat} &= k_{sat} && for\ u_a - u_w \le AEV \end{aligned} \quad . \qquad [4.5]$$

The pore-size distribution index (λ) is defined as the negative slope of a SWCC (degree of saturation against suction). The λ parameter can be obtained by curve fitting the Brooks & Corey SWCC model (Eq. 4.6) to the *in situ* SWCC (Figure 4-4):

$$\begin{aligned} \frac{S - S_r}{1 - S_r} &= \left(\frac{AEV}{u_a - u_w}\right)^{\lambda} && for\ u_a - u_w > AEV \\ S &= 1 && for\ u_a - u_w \le AEV \end{aligned} \quad , \qquad [4.6]$$

where k_{unsat} is the unsaturated hydraulic conductivity; k_{sat} is the saturated hydraulic conductivity; AEV is the air-entry value obtained from *in situ* SWCC; *S* is the instantaneous degree of saturation; S_r is the residual degree of saturation; u_a-u_w is the matric suction; and λ is the pore-size distribution index. The results are presented in Figure 4-8.

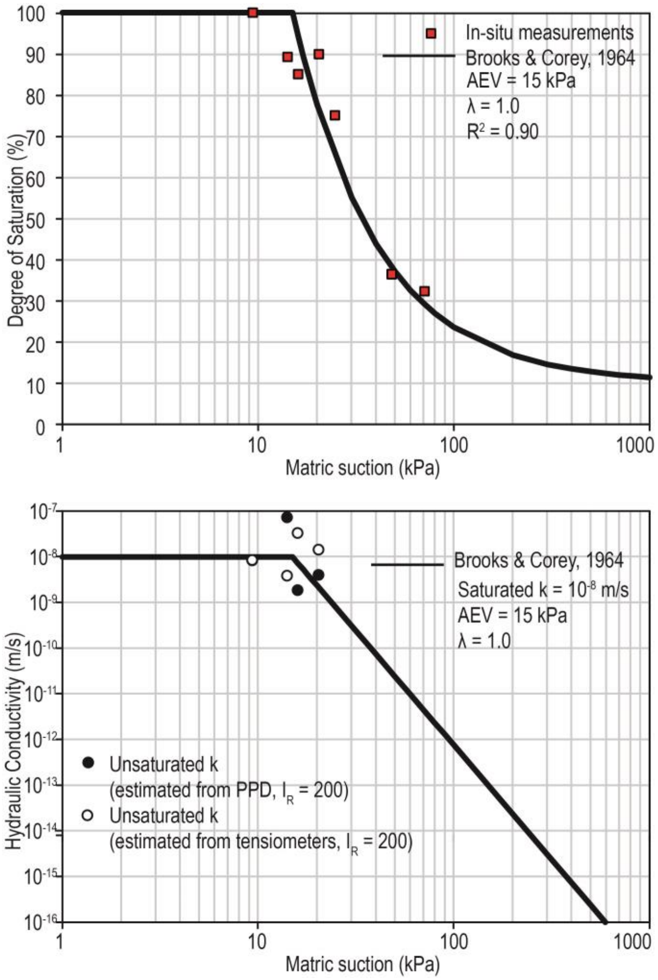

Figure 4- 8: Estimated unsaturated hydraulic conductivity (in situ conditions)

4.4.6 *Estimation of In Situ Pore-water Pressure*

During a PPD test, the excess pore-water pressure generated by cone penetration dissipates until *in situ* levels are achieved, from which the pore-water pressure profile of the subsurface can be deduced (see Figure 4-9 as an example). For saturated soils, the pore-water pressure of the subsurface is normally assumed to be under hydrostatic conditions; however, this cannot be assumed for the chamber test because the water content of the soil column was controlled and kept constant. Tensiometer readings from Test 1 indicate the pore-water pressure was constant with depth (data not shown). The *in situ* pore-water pressures measured for each test are summarized in Table 3.

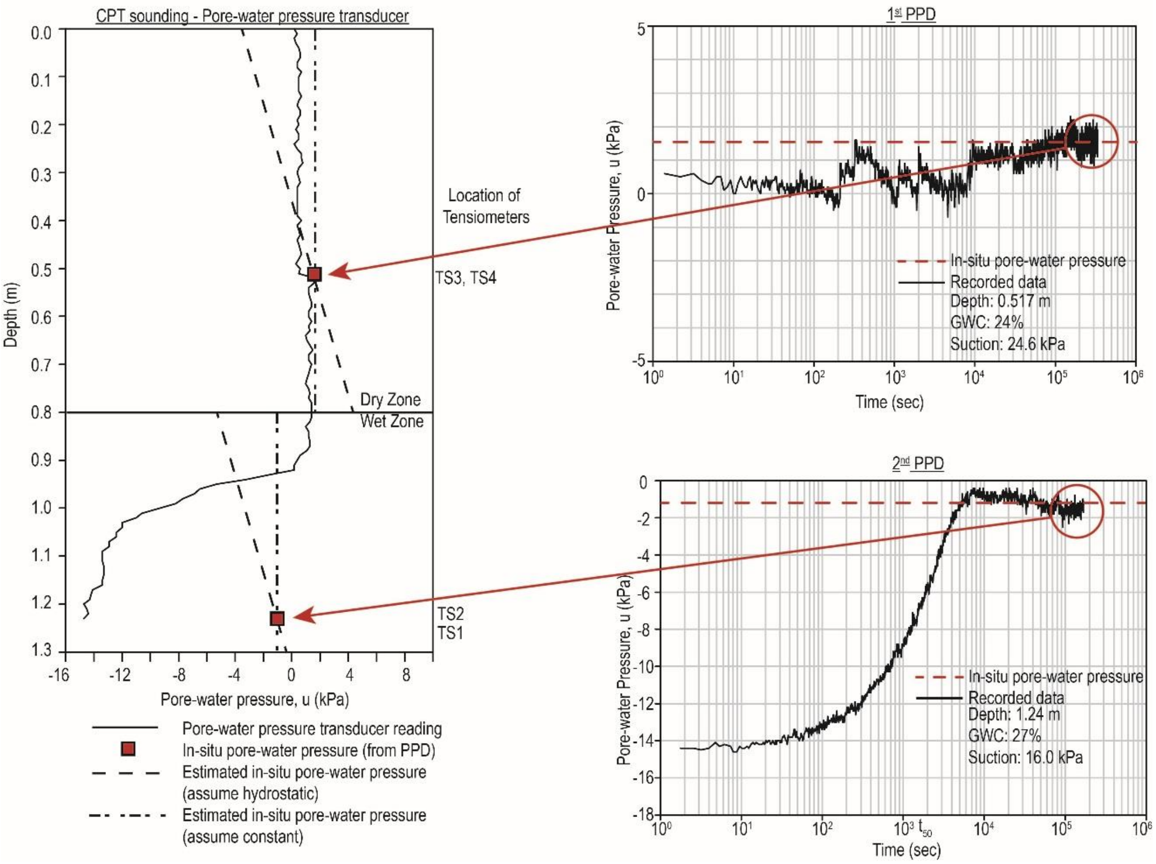

Figure 4- 9: Interpreting in situ pore-water pressure from PPD test results for Test 3 (pore pressure transducer)

Table 4- 3: Pore-water pressure profile of each chamber test

	In situ pore-water pressure (kPa)		
	Estimated from PPDs	Estimated using tensiometers	% Difference
Test 1	8	-9.4	185
Test 2 Dry Zone	-0.1	-70.7	100
Test 2 Wet Zone	-3.5	-20.4	83
Test 3 Dry Zone	0.6	-24.6	102
Test 3 Wet Zone	-0.5	-16.0	97
Test 4 Dry Zone	2.5	-53.5	105
Test 4 Wet Zone	-3.2	-14.1	77

Air pressure was not controlled during the chamber tests (remains atmospheric), so matric suction values measured by the tensiometers are equal to the *in situ* pore-water pressure obtained from the axis translation technique (Hilf, 1956). However, the *in situ* pore-water pressures estimated using PPD tests and tensiometers are very different (>77%) and could be due to desaturation of the pore-pressure transducer.

Despite the fact that on-board pore-water pressure transducers are mostly used to measure a positive pore-water pressure response, the literature (Burns & Mayne, 1998a,b; Robertson & Cabal, 2015; Robertson et al., 2017) suggests they are also capable of measuring pore-water pressures in the negative range. However, measurements of negative pore-water pressure become inaccurate if the instrument is not fully saturated (Campanella & Robertson, 1988; Fredlund et al., 2012). This is very likely the case while conducting CPT tests in unsaturated soils because the porous stone could be desaturated due to hydraulic head differences or air diffusion. Because the readings from the pore pressure transducer obtained in an unsaturated soil generally do not reflect the actual negative pore-water pressure (suction), erroneous results can occur if it is used to characterize the *in situ* condition of the soil.

4.4.7 *Effective Stress of Unsaturated Soils*

One of the erroneous interpretations that can result from inaccurate pore pressure measurements is effective stress. In saturated soils, the effective stress (σ’) is the difference between total stress (σ) and pore-water pressure (u_w) (Terzaghi, 1925):

$$\sigma' = \sigma - u_w \, . \qquad [4.7]$$

Terzaghi’s effective stress equation assumes the soil is a two-phase material (containing only solids and water). However, unsaturated soil is a four-phase material that contains solids, water, the contractile skin (meniscus), and air (Fredlund and Morgenstern, 1977). Bishop (1959) proposed an expression for σ’ in unsaturated soil that also accounts for the pore-air pressure (u_a):

$$\sigma' = \sigma - u_a + \chi(u_a - u_w) \, , \qquad [4.8]$$

where χ is the effective stress parameter. The term u_a-u_w is also known as matric suction, which was defined by Hilf (1956) using the axis-translation method. χ is dependent on the degree of saturation and, for practical purposes, is sometimes assumed to be the degree of saturation (S) (Leroueil & Hight, 2003). However, Jennings & Burland (1962) demonstrated that χ is not only quite different from the degree of saturation but also varies with different types of materials. The χ parameter of the red silt was estimated in Chapter 3 using unsaturated triaxial tests.

The effective stress of the unsaturated soil was estimated by substituting the vertical overburden stress, pore-air pressure (equal to atmospheric, hence, 0 kPa), and matric suction (measured from tensiometers) into Eq. 4.8. Because the pore-water pressures estimated using PPD tests and tensiometers are significantly different (Table 3), the calculated values for *in situ* effective stress also differ. Figure 4-10 shows the effective stress evaluated using the PPD tests tends to underestimate the suction hardening effect, and so the estimated *in situ* effective stress is closer to the value of total stress.

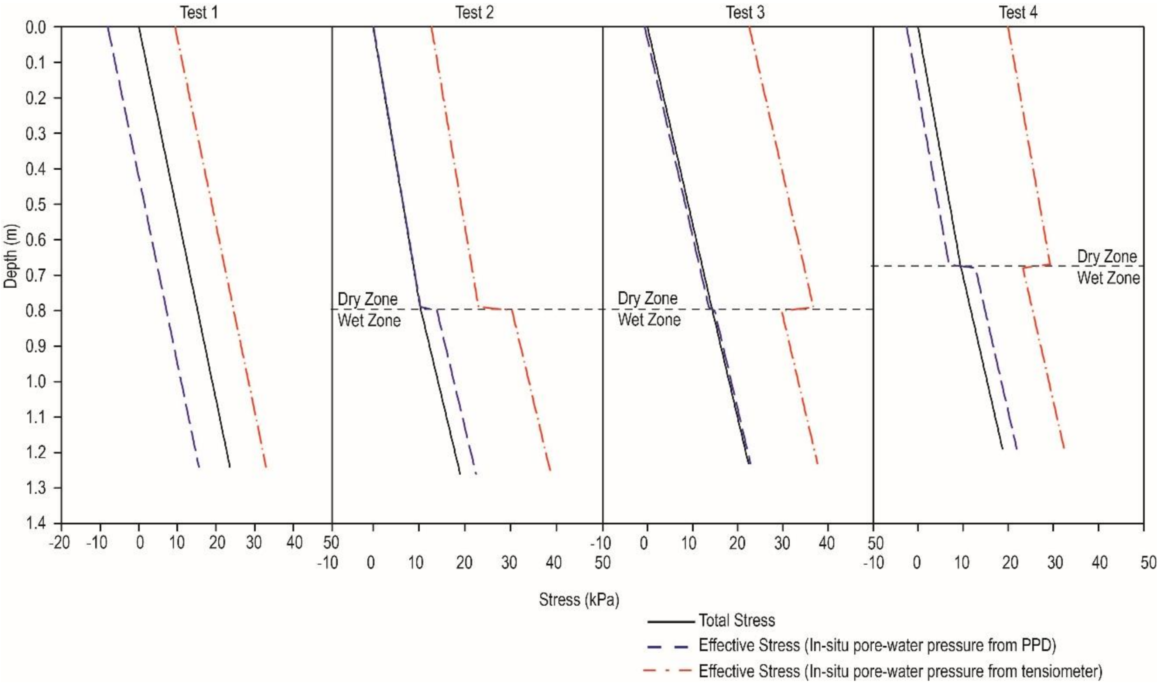

Figure 4- 10: Calculated effective stresses for chamber tests

4.4.8 Soil Behaviour Type (SBT)

CPTs provide extremely detailed information about subsurface stratigraphy. Robertson (1990) developed two SBT charts to determine the soil type of the subsurface. The first plots the normalized cone resistance (Q_{tn}) and normalized friction ratio (F_r) on an SBT chart (Robertson & Cabal, 2015), with these two values iteratively calculated until the values of soil behaviour type index (I_c), stress exponent (n), and normalized cone resistance (Q_{tn}) converge in the following equations (Robertson, 2016):

$$Q_{tn} = \left(\frac{q_t - \sigma_v}{p_a}\right)\left(\frac{p_a}{\sigma_v'}\right)^n , \qquad [4.9]$$

$$F_r = \frac{f_s}{q_t - \sigma_v} * 100\% , \qquad [4.10]$$

$$I_c = \sqrt{(3.47 - \log Q_{tn})^2 + (\log F_r + 1.22)^2} , \qquad [4.11]$$

$$n = 0.381(I_c) + 0.05\left(\frac{p_a}{\sigma_v'}\right) - 0.15 , \qquad [4.12]$$

where σ_v' is the vertical effective stress; σ_v is the vertical total stress; p_a is the atmospheric pressure (101.3 kPa); and q_t is the corrected cone resistance.

As noted above, the effective stress of an unsaturated soil can be incorrectly evaluated if the *in situ* pore pressure is derived solely from the PPD test. As a result, error could also propagate to the SBT analyses, because the estimated soil types using the results of PPD and tensiometers are different (see Figure 4-11 as an example; SBT analyses for all tests available as Figures SI 19-32).

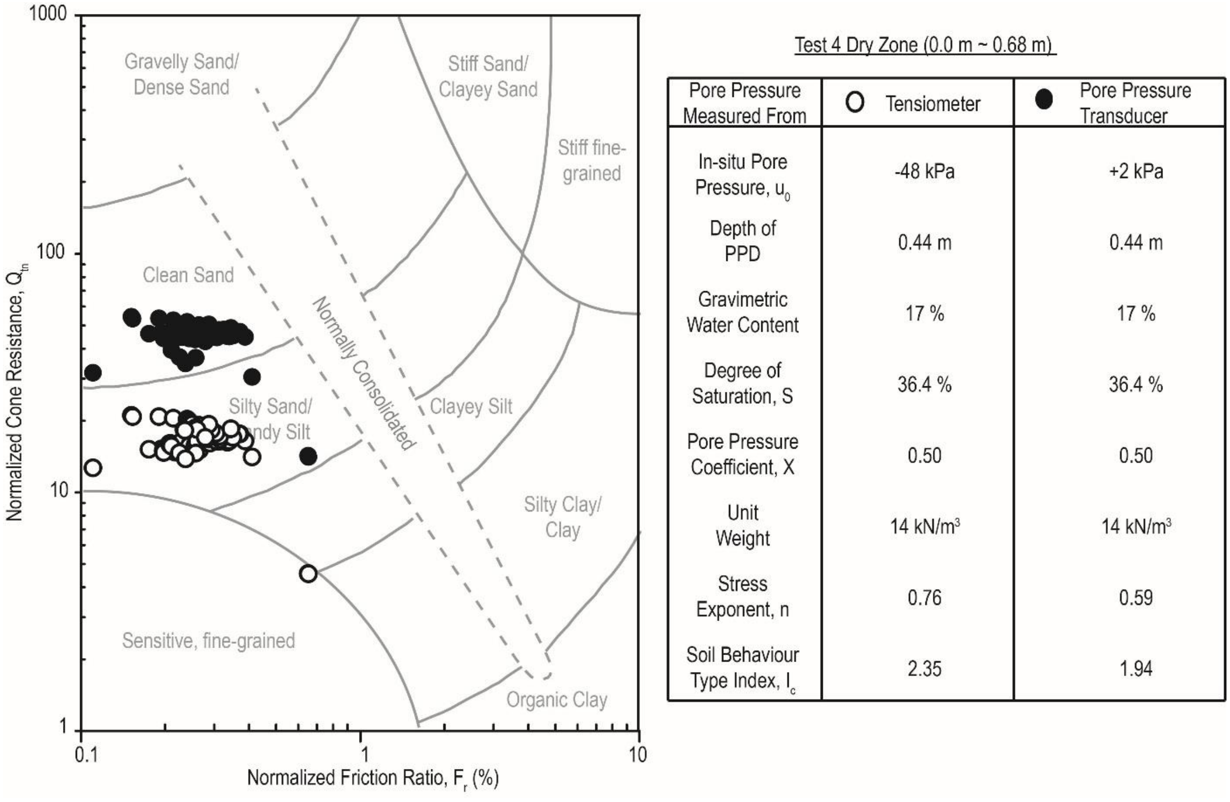

Test 4 Dry Zone (0.0 m ~ 0.68 m)

Pore Pressure Measured From	○ Tensiometer	● Pore Pressure Transducer
In-situ Pore Pressure, u_0	-48 kPa	+2 kPa
Depth of PPD	0.44 m	0.44 m
Gravimetric Water Content	17 %	17 %
Degree of Saturation, S	36.4 %	36.4 %
Pore Pressure Coefficient, X	0.50	0.50
Unit Weight	14 kN/m³	14 kN/m³
Stress Exponent, n	0.76	0.59
Soil Behaviour Type Index, I_c	2.35	1.94

Figure 4- 11: Different SBT results (Qt-Fr plot) using tensiometer and pore pressure transducer readings from Test 4 (dry zone)

Prior to the chamber tests, the grain size distribution determined using sieve and hydrometer analyses (Chapter 3) classified the red silt specimen as a silty-sand. The SBT results for each chamber test (Figure 4-12) show the evaluated soil type becomes more granular with increasing suction (decreasing degree of saturation), which could be a result of increasing stiffness (cone resistance) and decreasing sleeve friction. Alternatively, the failure to capture negative pore-water pressures (measuring 0 when the pore-water pressure is -16 to -24 kPa) could have resulted in an over-estimation of Q_{tn}, which collaterally deviated the SBT value.

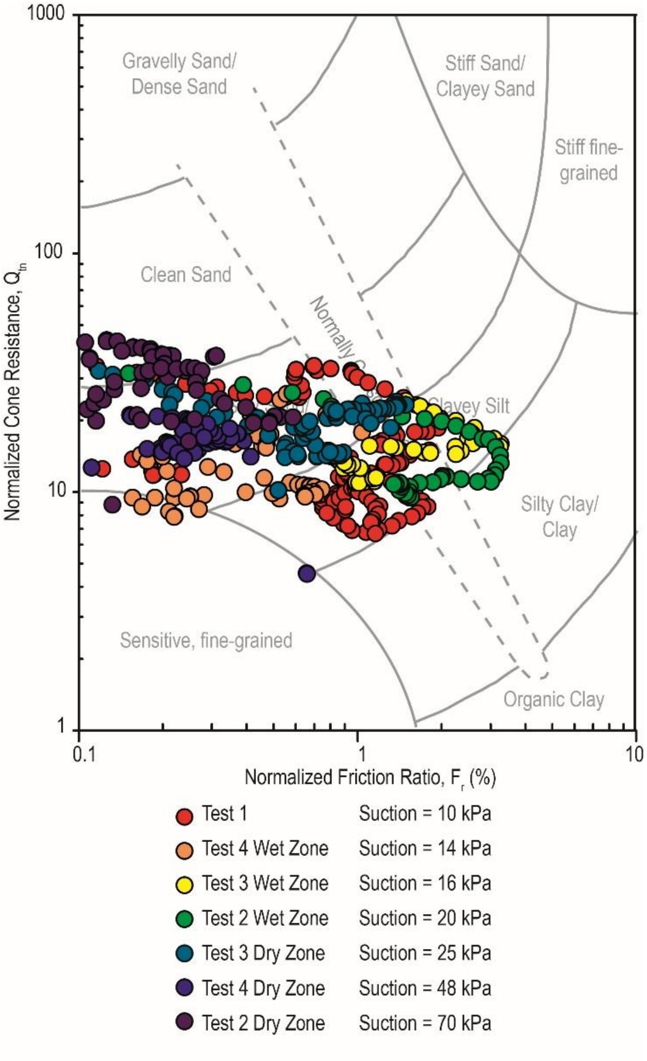

Figure 4- 12: Estimated soil type with change of suction (Qt-Fr plot)

Lunne et al. (1997) generalize the hydraulic conductivities and SBT indices of each material classified using an SBT chart (Table 4-4), but these do not seem applicable to unsaturated soils. As demonstrated in Figure 4-8, the hydraulic conductivity of an unsaturated soil decreases with increasing suction. While the SBT suggests the unsaturated silt is “Clean Sand” in Figure 4-12, the hydraulic conductivities of clean sand and unsaturated silt are seven to eight orders of magnitude different (Table 4-4 and Figure 4-8). Extra caution should therefore be taken when estimating soil properties from the SBT chart.

Table 4- 4: Zone and material on SBT chart (after Lunne et al., 1997)

SBT Zone	Material	Hydraulic conductivity (m/s)	SBT Index, I_c
1	Sensitive, fine grained	3×10^{-10} to 3×10^{-8}	N/A
2	Organic soils-peats	1×10^{-10} to 1×10^{-8}	$I_c > 3.60$
3	Clay to silty clay	1×10^{-10} to 1×10^{-9}	$3.60 > I_c > 2.95$
4	Silt-clay mixtures	3×10^{-9} to 1×10^{-7}	$2.95 > I_c > 2.60$
5	Fine sand-silt mixtures	1×10^{-7} to 1×10^{-5}	$2.60 > I_c > 2.05$
6	Sands	1×10^{-5} to 1×10^{-3}	$2.05 > I_c > 1.31$
7	Gravelly sand	1×10^{-3} to 1	$I_c < 1.31$
8	Very stiff sand to clayey sand	1×10^{-8} to 1×10^{-3}	N/A
9	Very stiff fine grained	1×10^{-9} to 1×10^{-7}	N/A

The second type of SBT chart utilizes the excess pore-water pressure measurement and cone resistance value obtained with depth to determine the soil type of the subsurface, plotting Q_{tn} vs. normalized pore pressure parameter (B_q) (Robertson & Cabal, 2015). Q_{tn} can be calculated using Equations 9-12, and B_q is calculated using (Robertson, 2016):

$$B_q = \frac{u_2 - u_0}{q_t - \sigma_v}, \tag{4.13}$$

where u_2 is the excess pore-water pressure measured at cone shoulder (u_2 position) and u_0 is the *in situ* pore-water pressure.

Although the values of B_q are consistent (close to zero) due to the magnitude of excess pore-water pressure being small compared to the net cone resistance ($q_t - \sigma_v$), the SBT results can be different (Figure 4-13); here, the pore pressure transducer results classify the red silt as a clean sand/silty sand material whereas tensiometer readings classify it as a silty sand to clayey silt.

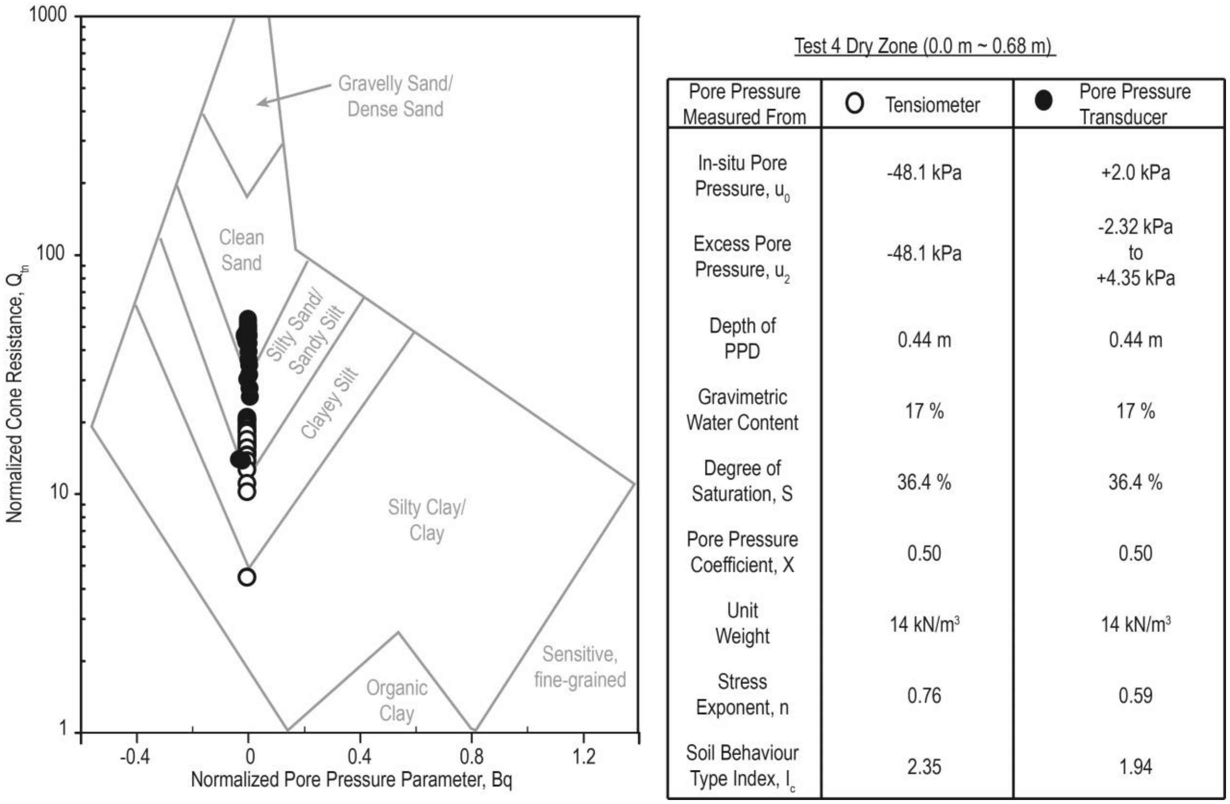

Test 4 Dry Zone (0.0 m ~ 0.68 m)

Pore Pressure Measured From	○ Tensiometer	● Pore Pressure Transducer
In-situ Pore Pressure, u_0	-48.1 kPa	+2.0 kPa
Excess Pore Pressure, u_2	-48.1 kPa	-2.32 kPa to +4.35 kPa
Depth of PPD	0.44 m	0.44 m
Gravimetric Water Content	17 %	17 %
Degree of Saturation, S	36.4 %	36.4 %
Pore Pressure Coefficient, X	0.50	0.50
Unit Weight	14 kN/m^3	14 kN/m^3
Stress Exponent, n	0.76	0.59
Soil Behaviour Type Index, I_c	2.35	1.94

Figure 4- 13: Different SBT results (Qt-Bq plot) using tensiometer and pore pressure transducer readings from Test 4 (dry zone)

Plotting the SBT results of each chamber test together (Figure 4-14) again indicates that the evaluated soil type becomes more granular with increasing suction (decreasing degree of saturation). This phenomenon is within expectations considering the combination of unvarying B_q values (close to zero) and increasing cone resistance (thus, Q_{tn}) with increasing matric suction (Figure 4-5).

4.4.9 *Friction Angle*

The shear strength profile of an unsaturated soil can be estimated using the modified Mohr-Coulomb equations proposed by Fredlund & Rahardjo (1993):

$$\tau_{ff} = c' + (\sigma - u_a)_f \tan\phi' + (u_a - u_w)_f \tan\phi^b, \tag{4.14}$$

where τ_{ff} is the shear strength at failure for unsaturated soil; *c'* is the effective cohesion; $(\sigma\text{-}u_a)_f$ is the net normal stress at failure; ϕ' is the effective friction angle; $(u_a\text{-}u_w)_f$ is the matric suction at failure; and ϕ^b is the friction angle denoting the change of shear stress with respect to matric suction. This parameter was created by Fredlund & Rahardjo (1993) to provide a linear approximation to the effective stress parameter (χ) of unsaturated soils. As such, the shear stress at failure of an unsaturated soil can be estimated using the frictional parameters (namely *c'*, ϕ', and ϕ^b) under different stress state variables ($(\sigma\text{-}u_a)_f$ and $(u_a\text{-} u_w)_f$). The frictional parameters of the red silt were characterized by unsaturated triaxial tests with measured values of *c'*, ϕ', and ϕ^b of 11.1 kPa, 29.9°, and 24.2°, respectively.

Mayne & Campanella (2005) proposed Eq. 4.15 to approximate the graphical solution proposed by the Norwegian University of Science and Technology (NTNU) (Sennset et al., 1988), which is applicable to most sands, silts, and clays if the normalized pore pressure parameter is between 0.1 and 1.0 and when ϕ' is between 20 and 45°:

$$\phi' \approx 29.5^\circ B_q^{0.121}\left[0.256 + 0.336 B_q + \log Q_{tn}\right]. \tag{4.15}$$

For soils with $B_q < 0.1$, such as the red silt, the empirical correlation proposed by Kulhawy & Mayne (1990) should be used instead:

$$\phi' = 17.6 + 11\log(Q_{tn})\,. \tag{4.16}$$

The normalized cone resistance in Eq. 4.16 can be obtained from either pore pressure transducer or tensiometer readings. Averaged friction angles of the red silt from each test were estimated based on Q_{tn} values calculated using data from either the pore pressure transducers or tensiometers. Figure 4-14 shows the friction angle measured from triaxial test results falls outside the one standard deviation range of the estimated friction angle using the pore pressure transducer readings, and also indicates the values of the estimated friction angle increase with matric suction, possibly influenced by the increasing cone resistance with matric suction (Figure 4-5).

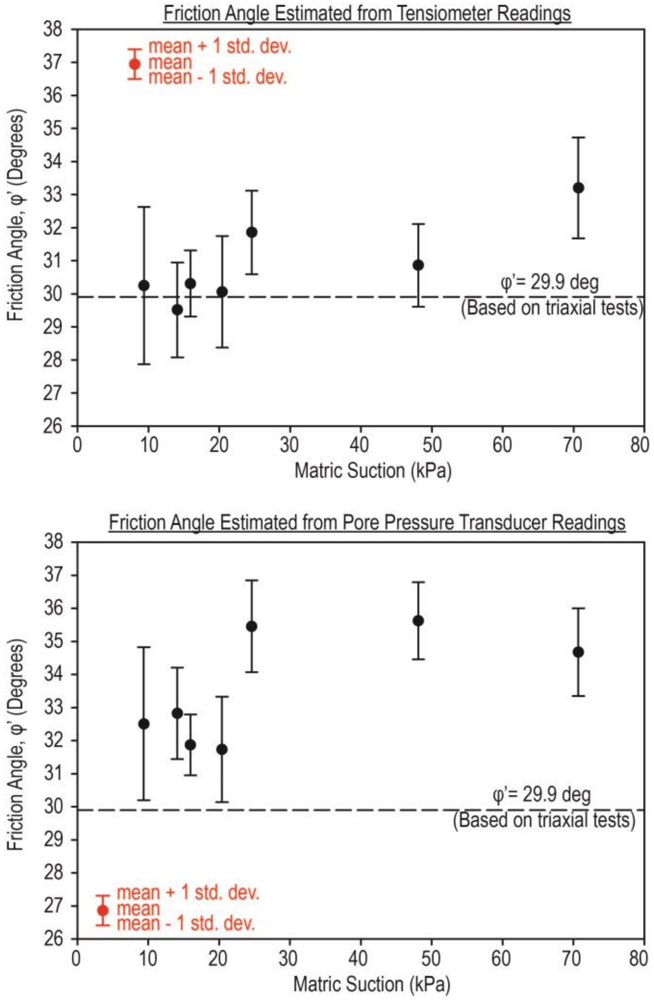

Figure 4- 14: Estimated friction angles

4.4.10 Estimation of Effective Stress Parameter

An insufficient number of CPT projects have been conducted in unsaturated soils to produce an empirical correlation relating ϕ^b to cone resistance or sleeve friction, and therefore evaluation of the effective stress parameter, and thus ϕ^b, requires a more complex and mathematically rigorous approach.

The CPT is often analyzed using the spherical cavity expansion analogy (Vesić, 1972), in which a spherical cavity is created within a soil mass. The stress required to create the cavity is known as the limit pressure (σ_{LP}). Outside the cavity is a plastic zone of radius *R*, within which the soil yields and deforms plastically. The stresses acting on the soil within the plastic zone are defined as the radial stress (σ_r) and hoop stress (σ_θ). The elastic zone surrounds the plastic zone. Soils within the elastic zone deform elastically (no volume change), and have minimal changes in pore pressure. The radial stress at the interface of the elastic/ plastic zone is denoted as the yield stress (σ_P).

Carter et al. (1986) provided solutions to the spherical cavity expansion for a cohesive-frictional soil using Mohr-Coulomb's constitutive model, from which σ_{LP} can be calculated using the *in situ* principal stresses (σ_r and σ_θ):

$$\frac{2G}{p_o} = \frac{N-1}{N+k}\left[T\left(\frac{\sigma_{LP}}{\sigma_P}\right)^{\gamma} - Z\frac{\sigma_{LP}}{\sigma_P}\right] \qquad [4.17]$$

where *G* is the shear modulus; p_o is the at-rest lateral earth pressure; *k* equals 1 (cylindrical expansion) or 2 (spherical expansion); *N* is the passive lateral earth pressure coefficient; and *T, Z,* and γ are parameters related to friction angle, dilation angle, and Poisson's ratio, respectively (fully defined in Carter et al. (1986)).

Parameters used for the calculation of σ_{LP} are presented in Chapter 3. Because the σ_{LP} calculated according to Carter et al. (1986) assumes the soil is a standard Mohr-Coulomb material, the shear strength due to matric suction should therefore be considered the “effective cohesion” or c’ for a truly cohesionless material:

$$\tau = c' + \sigma' \tan\phi' , \tag{4.18}$$

where

$$\mathrm{c}' = (u_a - u_w)_{\mathrm{f}} \tan\phi^b \tag{4.19}$$

or

$$\mathrm{c}' = \chi(u_a - u_w)_{\mathrm{f}} \tan\phi' . \tag{4.20}$$

Ladanyi & Johnston (1974) derived a relationship between cone resistance (q_t) and the limit pressure (σ_{LP}) for a cohesive-frictional material using Mohr-Coulomb as the constitutive model of the soil:

$$q_t = \sigma_{LP}(1 + \tan\phi') + c' . \tag{4.21}$$

The σ_{LP} and *c’* of the unsaturated soil can, therefore, be iteratively calculated by matching the calculated cone resistance value to the averaged value of the measured cone resistance until convergence. The predicted and measured cone resistance values are presented in Figure 4-15. In general, the shear strength gained through matric suction is approximately 1.5 to 3.5% of the net cone resistance value.

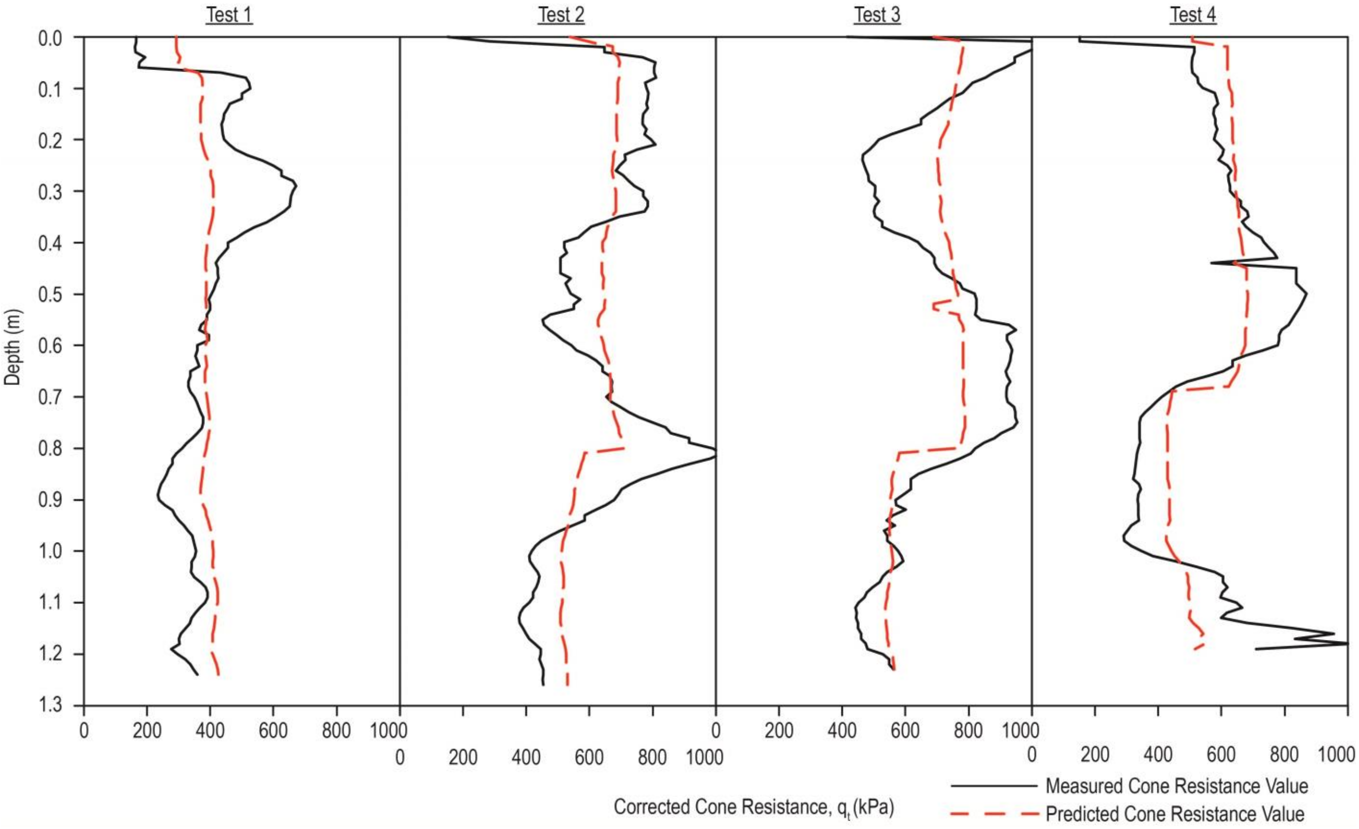

Figure 4- 15: Measured and predicted cone resistance values.

With the obtained *c'* value, the measured matric suction using tensiometers and the estimated friction angle using Eq. 4.17, the effective stress parameter ϕ^b or χ can be estimated using Eq. 4.19 and Eq. 4.20, respectively. Figures 4-16 and 4-17 show the estimated values and the lab-testing results are consistent with each other.

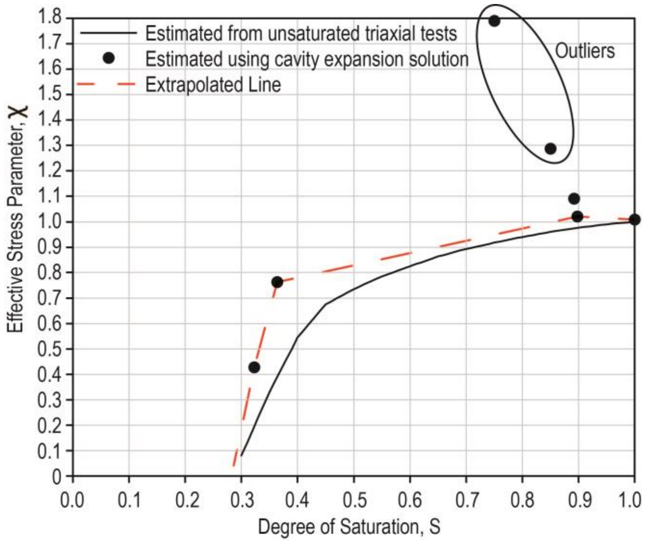

Figure 4- 16: Measured and predicted effective stress parameter

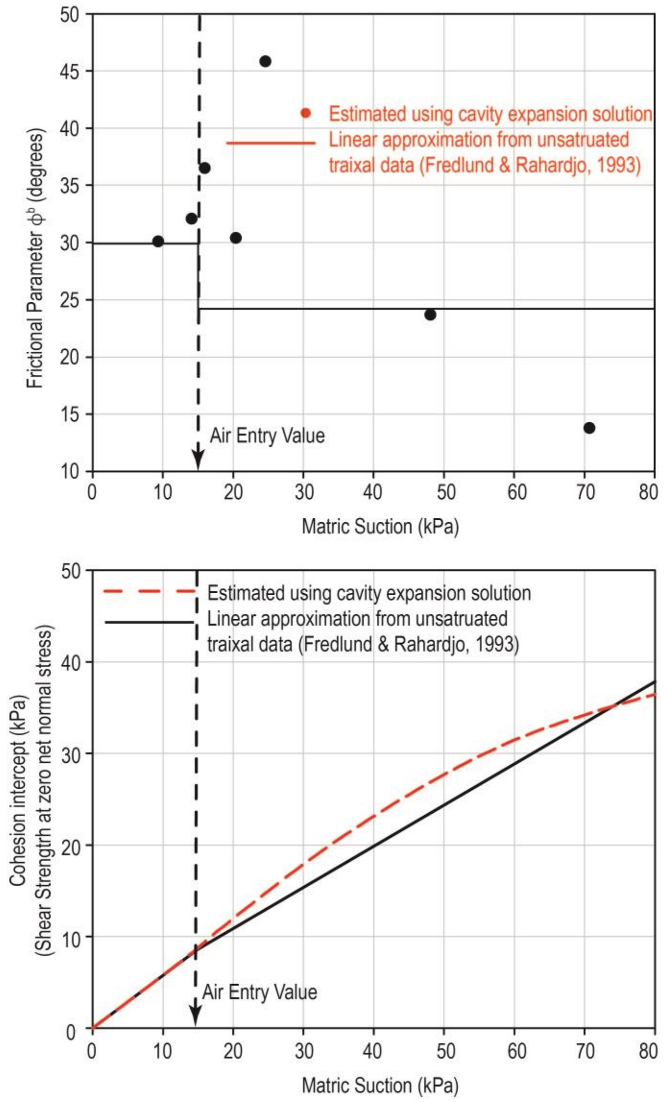

Figure 4- 17: Measured and predicted frictional parameters of the unsaturated silt

4.5 Conclusion

This research study investigated the validity of existing empirical correlations for CPT in unsaturated soils. Unsaturated silt specimens with controlled water content were deposited into a 1.6-m tall 0.9-m diameter pipe and penetrated by a 10-cm^2 piezocone. In addition to cone resistance, sleeve friction, and pore-water pressure, matric suction was also measured using tensiometers. Chamber test results indicate a conventional pore pressure transducer with a brass porous stone is incapable of capturing the matric suction in unsaturated soils and, hence, tensiometers ought to be used to obtain pore pressure measurements during and after penetration.

While the pore pressure transducer unit is incapable of providing any useful information within unsaturated soils because its porous element desaturates, tensiometers ought to be used to evaluate pore pressures. Tensiometer readings can be used to estimate *in situ* SWCC, unsaturated hydraulic conductivity, the *in situ* pore-water pressure profile, and *in situ* effective stress.

Empirical correlations used to interpret the results of PPD tests and SBT were also reviewed, with their applicability to unsaturated soils shown to be limited. In contrast, the empirical correlation used to estimate the friction angle of the subsurface agrees with the values obtained through lab testing, indicating its applicability provided the matric suction of the soil is accurately measured.

Spherical cavity expansion solutions proposed by Carter et al. (1986) and Ladanyi & Johnston (1974) were used to estimate the apparent cohesion and limit pressure of the chamber test results. These values were used to calculate the frictional parameter φ^b and the effective stress parameter χ of the unsaturated soil, which were highly consistent with lab results.

References

Aas, G., Lacasse, S., Lunne, T., & Hoeg, K. (1986). Use of in-situ tests for foundation design on clay. *Proceeding of In Situ '86: Use of In Situ Tests in Geotechnical Engineering*, 1-30.

ASTM, D. (2000). Standard Test Method for Performing Electronic Friction Cone and Piezocone Penetration Testing of Soils. ASTM D-5778.

Bishop, A. (1959). The principle of effective stress. *Teknisk Ukeblad, 106*(39), 859-863.

Brooks, R., & Corey, T. (1964). *Hydraulic Properties of Porous Media.* Fort Collins: Colorado State University.

Burns, S., & Mayne, P. (1998a). Monotonic and dilatory pore-pressure decay during piezocone tests in clay. *Canadian Geotechnical Journal, 35*, 1063-1073.

Burns, S., & Mayne, P. (1998b). *Penetrometers for Soil Permeability and Chemical Detection.* Georgia Institute of Technology.

Campanella et al. (1986). Factors affecting the pore water pressure and its measurement around a penetrating cone. *International Proceedings of 39th Canadian Geotechnical Conference*, 291-299.

Campanella, R., & Robertson, P. (1988). Current status of the piezocone test. *In Proc. 1st Int. Symp. on Penetration Testing, 1*, 93-116.

Carter, J.P., Booker, J.Y., & Yeung, S.K. (1986) Cavity expansion in cohesive frictional soils. *Geotechnique,* 36(3), 349-358

Fredlund, D., & Houston, S. (2013). Interpretation of soil-water characteristic curves when volume change occurs as soil suction is changed. *Advances in Unsaturated Soils*, 15-31.

Fredlund, D. G., & Morgenstern, N. R. (1977). Stress state variables for unsaturated soils. *Journal of Geotechnical and Geoenvironmental Engineering*, *103*(ASCE 12919).

Fredlund, D.,Rahardjo, H. & Rahardjo, H. (1993). *Soil Mechanics for Unsaturated Soils.* John Wiley & Sons.

Fredlund, D. G., Rahardjo, H., & Fredlund, M. D. (2012). Unsaturated soil mechanics in engineering practice. John Wiley & Sons.

Fredlund, D.G., & Xing, A. (1994). Equations for the soil-water characteristic curve. *Canadian Geotechnical Journal* (31), 533-546.

Hilf, J. (1956). *An investigation of pore water pressure in compacted cohesive soils.* Bureau of Reclamation (US).

Houlsby, G., Wroth, C., Teh, C., & Sagaseta, C. (1989). *Research at Oxford on Analysis of the Piezocone Test.* Oxford University, Department of Engineering Science.

Jennings, J., & Burland, J. (1962). Limitations to the use of effective stresses in partly saturated soils. *Geotechnique, 12*(2), 125-144.

Kulhawy, F.H. & Mayne, P.W. (1990). *Manual on Estimating Soil Properties for Foundation Design, Report EPRI EL-6800.* Electric Power Research Institute, Palo Alto, CA. 306 pp.

Ladanyi, B., & Johnston, G.H. (1974). Behavior of circular footings and plate anchors embedded in permafrost. *Canadian Geotechnical Journal, 11(4)*, 531-533.

Leroueil, S., & Hight, D. (2003). Behaviour and properties of natural soils and soft rocks. *Characterisation and Engineering Properties of Natural Soils, 1*, 29-254.

Lunne, T., Eidsmoen, T., Gillespie, D., & Howland, J. (1986). Laboratory and field evaluation of cone penetrometer. *Proceeding of In-Situ '86: Use of In Situ Tests in Geotechnical Engineering*, 714-729.

Lunne, T., Robertson, P., & Powell, J. (1997). *Cone Penetration Testing in Geotechnical Practice.* New York: Blackie Academic, EF Spon/Routledge Publishing.

Mayne, P.W. & Campanella, R.G. (2005). Versatile site characterization by seismic piezocone. *Proceedings of the 16th International Conference on Soil Mechanics and Geotechnical Engineering*, Vol.2 (Osaka), Millpress, Rotterdam, The Netherlands, 721-724.

Nash, D., & Duffin, M. (1982). Site investigation of glacial soils using cone penetration tests. *Proceeding of 2nd European Symposium on Penetration Testing*, 733-738.

Parkin, A. K., & Lunne, T. (1982). Boundary effects in the laboratory calibration of a cone penetrometer for sand. *Norwegian Geotechnical institute publication*, (138).Rieke, H., & Chilingarian, G. (1974). Chapter 8. Equipment and techniques used in compaction studies. In H. Rieke, & G. Chilingarian, *Compaction of Argillaceous Sediments* (Vol. 16, pp. 353-398). New York: Elsevier.

Robertson, P. (1990). Soil classification using the cone penetration test. *Canadian Geotechnical Journal, 27*(1), 151-158.

Robertson, P. (2016). Cone penetration test (CPT)-based soil behaviour type (SBT) classification system—an update. *Canadian Geotechnical Journal, 53*(12), 1910-1927.

Robertson, P., & Cabal, K. (2015). *Guide to Cone Penetration Testing for Geotechnical Engineering* (6th ed.). California: Gregg Drilling & Testing, Inc.

Robertson, P., & Campanella, R. (1983a). Interpretation of cone penetration tests. Part I: Sand. *Canadian Geotechnical Journal, 20*, 718-733.

Robertson, P., & Campanella, R. (1983b). Interpretation of cone penetration tests. Park II: Clay. *Canadian Geotechnical Journal*(20), 734-745.

Robertson, P., da Fonseca, A., Ulrich, B., & Coffin, J. (2017). Characterization of unsaturated mine waste: a case history. *Canadian Geotechnical Journal, 0*(ja). Retrieved from https://www.youtube.com/watch?v=_BSStibb7dY

Senneset, K., Sandven, R., Lunne, T., By, T., & Amundsen, T. (1988, March). Piezocone tests in silty soils. In *Proceedings of the International Symposium on Penetration Testing, ISOPT*(Vol. 1, pp. 955-966).

Teh, C., & Houlsby, G. (1991). An analytical study of the cone penetration test in clay. *Goetechnique*, *41*(1), 17-34.

Terzaghi, K. (1925). Principles of soil mechanics, IV—Settlement and consolidation of clay. *Engineering News-Record*, *95*(3), 874-878.

Torstensson, B. (1977). The pore pressure probe. *Nordiske Geotekniske Mote*, *34*, 34.1-34.15.

Vesic, A. S. (1972). Expansion of cavities in infinite soil mass. *Journal of Soil Mechanics & Foundations Div*, 98(sm3).

Wong, J. (2018). Cone Penetration Test in Unsaturated Silt with Matric Suction Measurements, M.Sc. Thesis, University of Saskatchewan.

Yang, H., & Russell, A. (2015). Cone penetration tests in unsaturated silty sands. *Canadian Geotechnical Journal*, 431-444.

Yu, H., & Mitchell, J. (1998). Analysis of cone resistance: review of methods. *Journal of Geotechnical and Geoenvironmental Engineering*, *124*(2), 140-149.

Appendix 4A - CPT soundings

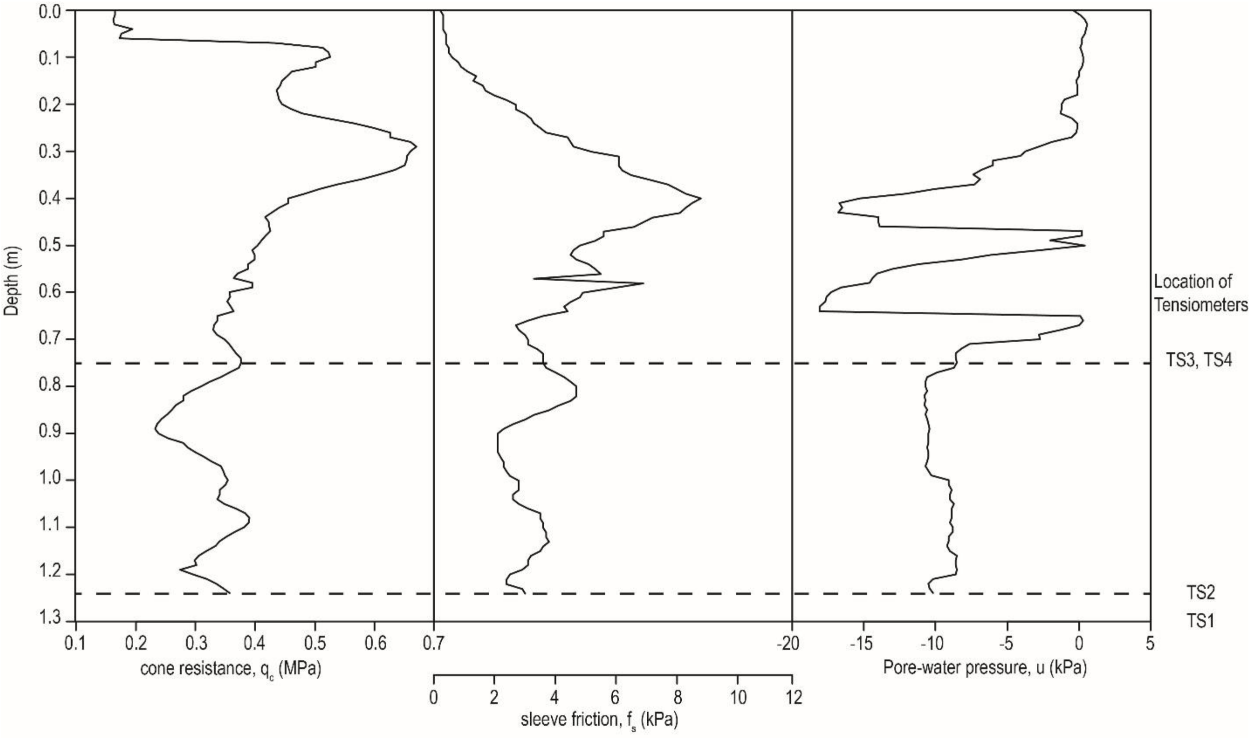

Figure 4A- 1: CPT soundings of Test 1

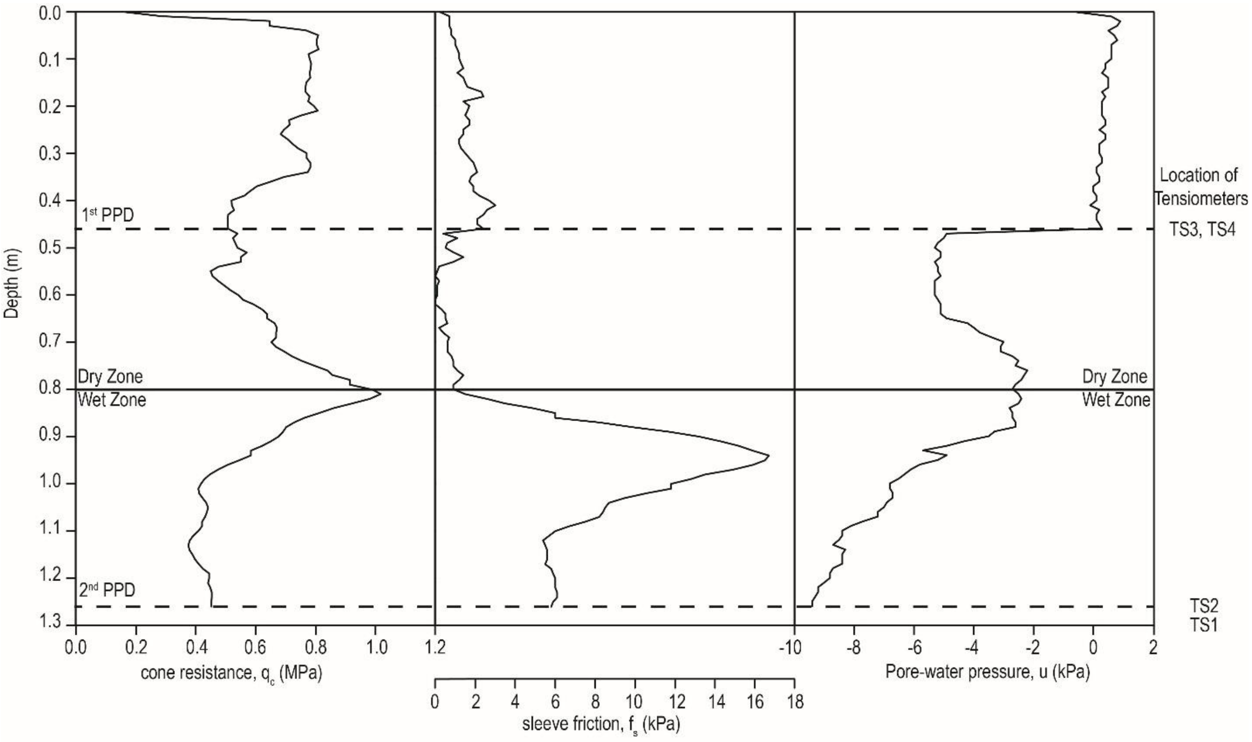

Figure 4A- 2: CPT soundings of Test 2

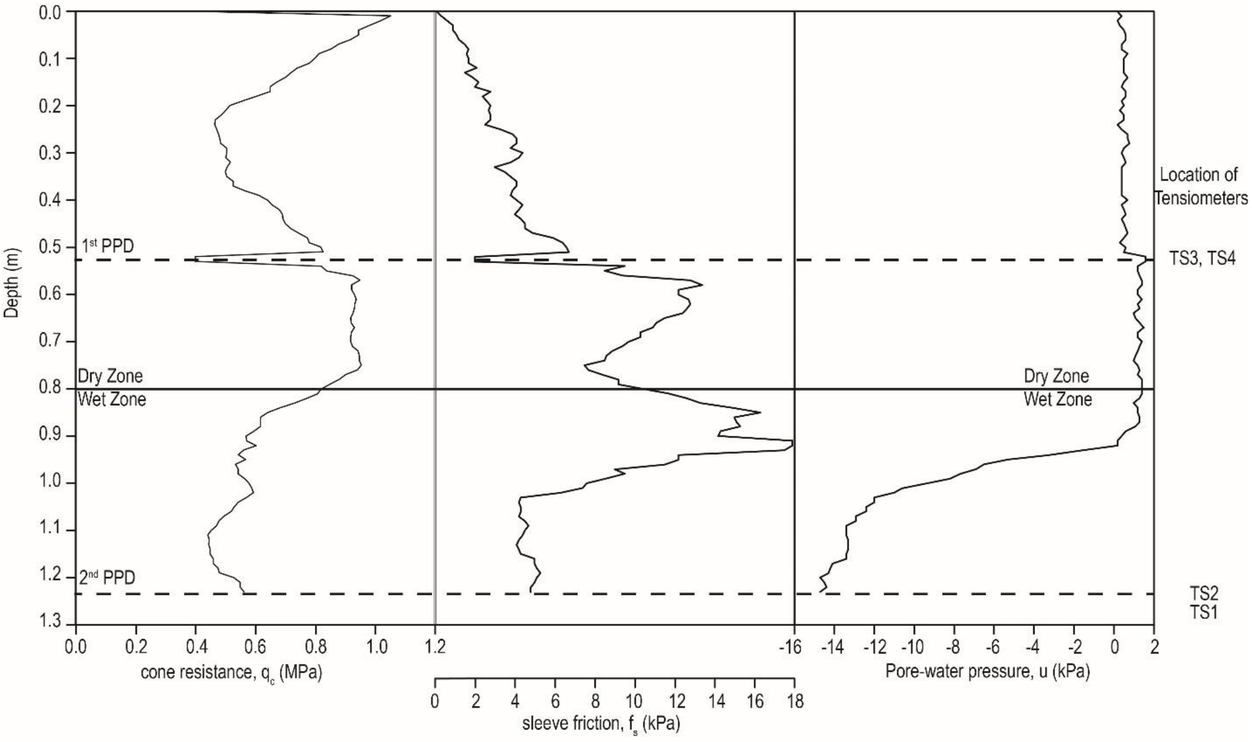

Figure 4A- 3: CPT soundings of Test 3

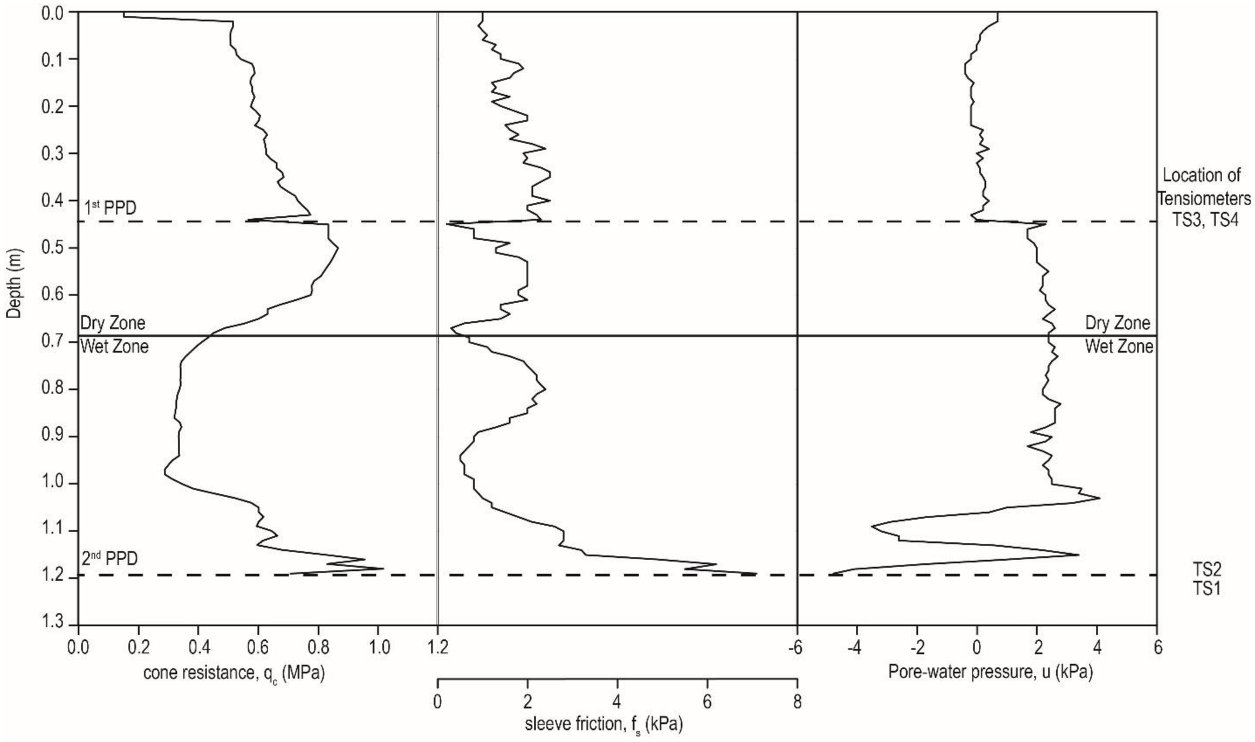

Figure 4A- 4: CPT soundings of Test 4

Appendix 4B - SBT charts

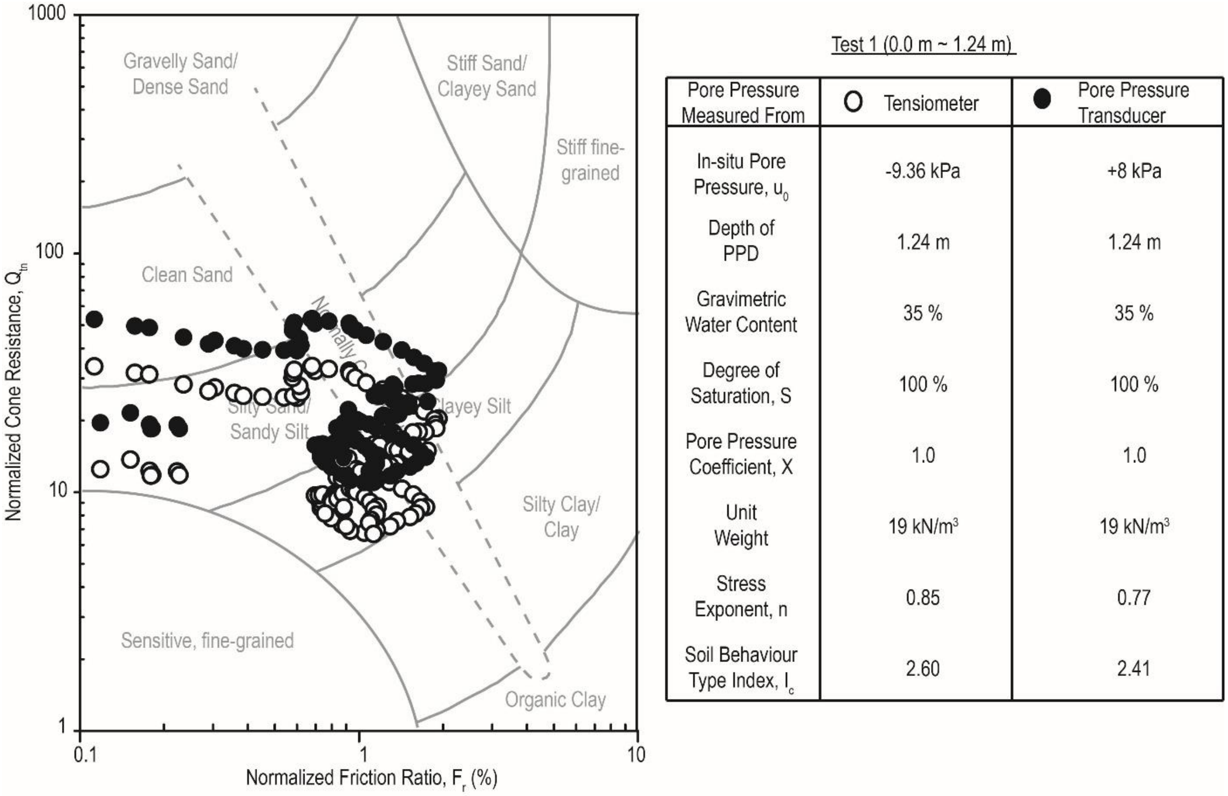

Test 1 (0.0 m ~ 1.24 m)

Pore Pressure Measured From	○ Tensiometer	● Pore Pressure Transducer
In-situ Pore Pressure, u_0	-9.36 kPa	+8 kPa
Depth of PPD	1.24 m	1.24 m
Gravimetric Water Content	35 %	35 %
Degree of Saturation, S	100 %	100 %
Pore Pressure Coefficient, X	1.0	1.0
Unit Weight	19 kN/m^3	19 kN/m^3
Stress Exponent, n	0.85	0.77
Soil Behaviour Type Index, I_c	2.60	2.41

Figure 4B- 1: SBT of Test 1 (Q_{tn} - F_r plot)

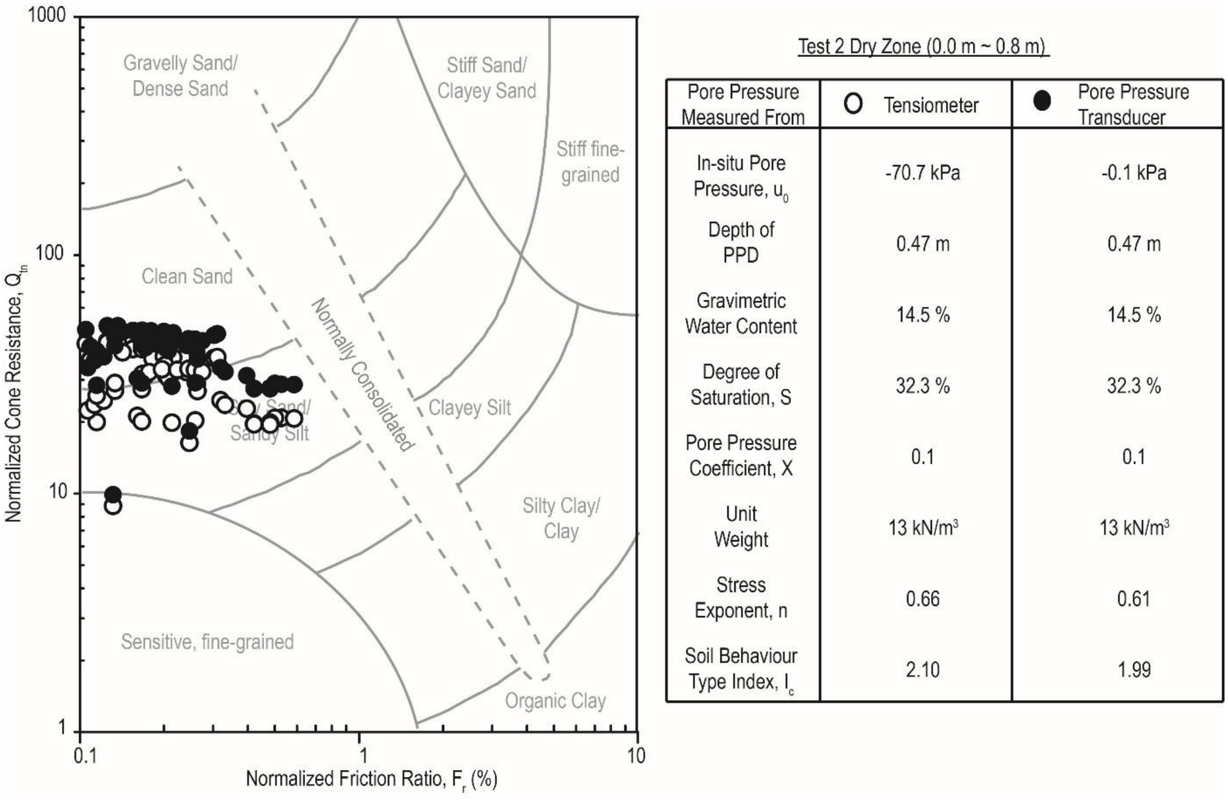

Test 2 Dry Zone (0.0 m ~ 0.8 m)

Pore Pressure Measured From	○ Tensiometer	● Pore Pressure Transducer
In-situ Pore Pressure, u_0	-70.7 kPa	-0.1 kPa
Depth of PPD	0.47 m	0.47 m
Gravimetric Water Content	14.5 %	14.5 %
Degree of Saturation, S	32.3 %	32.3 %
Pore Pressure Coefficient, X	0.1	0.1
Unit Weight	13 kN/m^3	13 kN/m^3
Stress Exponent, n	0.66	0.61
Soil Behaviour Type Index, I_c	2.10	1.99

Figure 4B- 2: SBT of Test 2 Dry Zone (Q_{tn} - F_r plot)

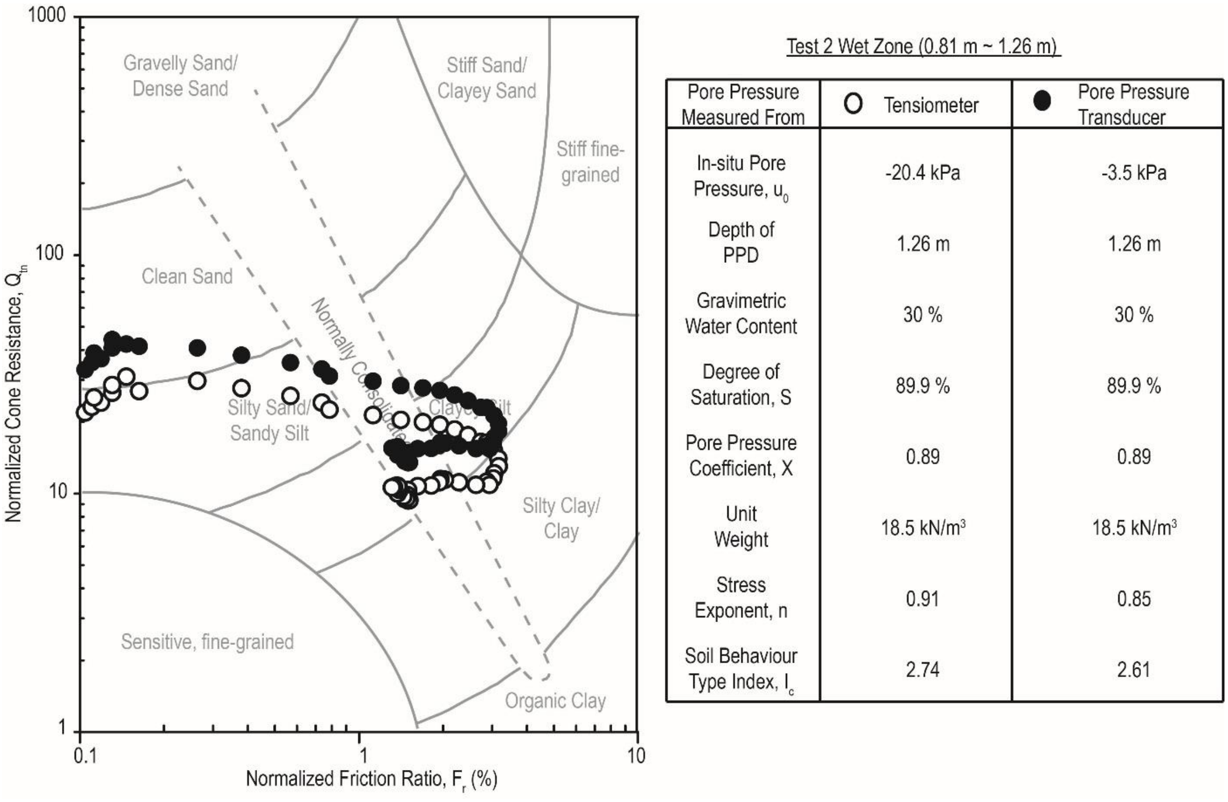

Test 2 Wet Zone (0.81 m ~ 1.26 m)

Pore Pressure Measured From	○ Tensiometer	● Pore Pressure Transducer
In-situ Pore Pressure, u_0	-20.4 kPa	-3.5 kPa
Depth of PPD	1.26 m	1.26 m
Gravimetric Water Content	30 %	30 %
Degree of Saturation, S	89.9 %	89.9 %
Pore Pressure Coefficient, X	0.89	0.89
Unit Weight	18.5 kN/m^3	18.5 kN/m^3
Stress Exponent, n	0.91	0.85
Soil Behaviour Type Index, I_c	2.74	2.61

Figure 4B- 3:SBT of Test 2 Wet Zone (Q_{tn} - F_r plot)

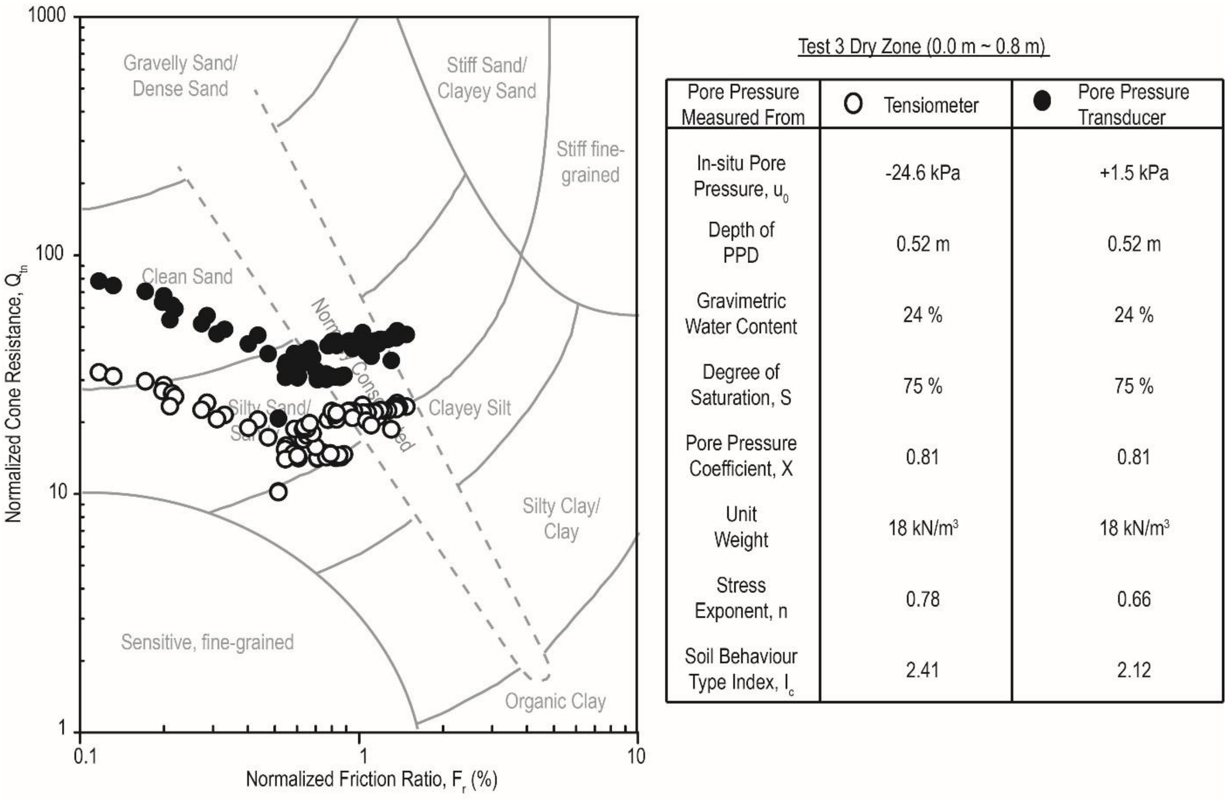

Test 3 Dry Zone (0.0 m ~ 0.8 m)

Pore Pressure Measured From	○ Tensiometer	● Pore Pressure Transducer
In-situ Pore Pressure, u_0	-24.6 kPa	+1.5 kPa
Depth of PPD	0.52 m	0.52 m
Gravimetric Water Content	24 %	24 %
Degree of Saturation, S	75 %	75 %
Pore Pressure Coefficient, X	0.81	0.81
Unit Weight	18 kN/m^3	18 kN/m^3
Stress Exponent, n	0.78	0.66
Soil Behaviour Type Index, I_c	2.41	2.12

Figure 4B- 4: SBT of Test 3 Dry Zone (Q_{tn} - F_r plot)

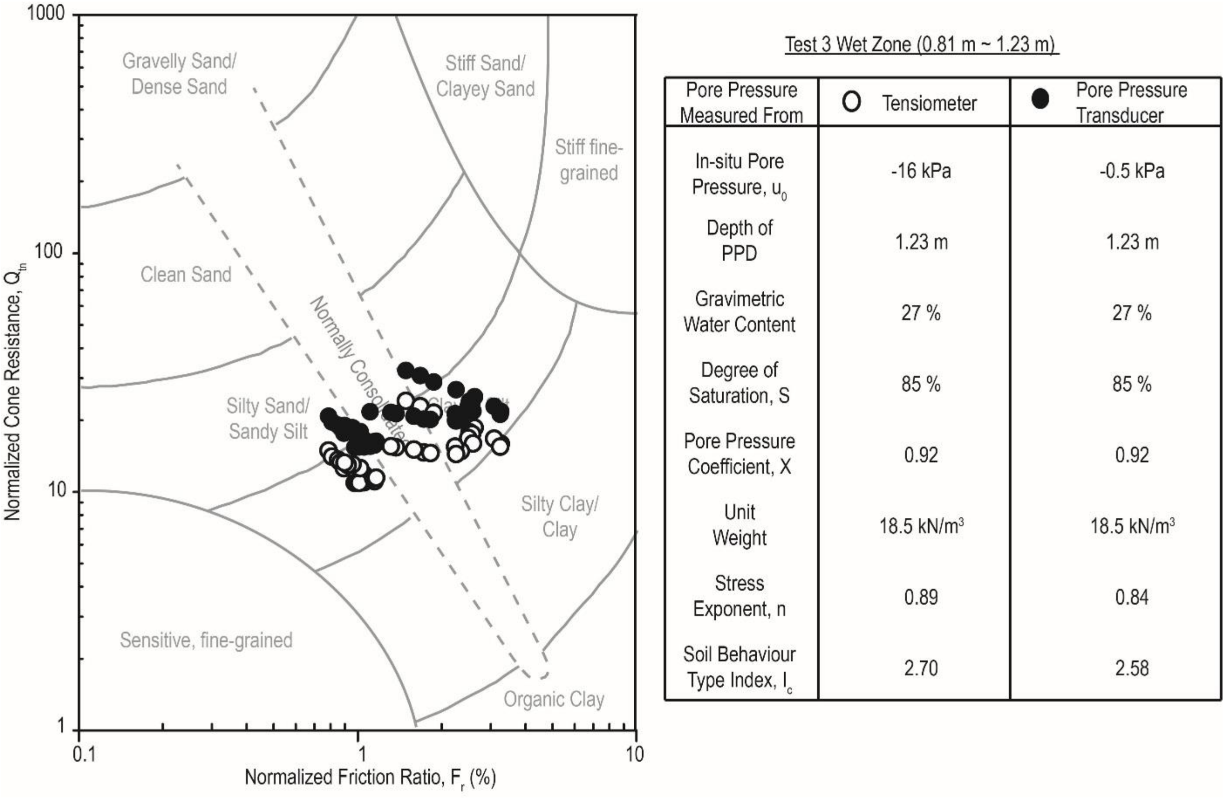

Test 3 Wet Zone (0.81 m ~ 1.23 m)

Pore Pressure Measured From	○ Tensiometer	● Pore Pressure Transducer
In-situ Pore Pressure, u_0	-16 kPa	-0.5 kPa
Depth of PPD	1.23 m	1.23 m
Gravimetric Water Content	27 %	27 %
Degree of Saturation, S	85 %	85 %
Pore Pressure Coefficient, X	0.92	0.92
Unit Weight	18.5 kN/m^3	18.5 kN/m^3
Stress Exponent, n	0.89	0.84
Soil Behaviour Type Index, I_c	2.70	2.58

Figure 4B- 5: SBT of Test 3 Wet Zone (Q_{tn} - F_r plot)

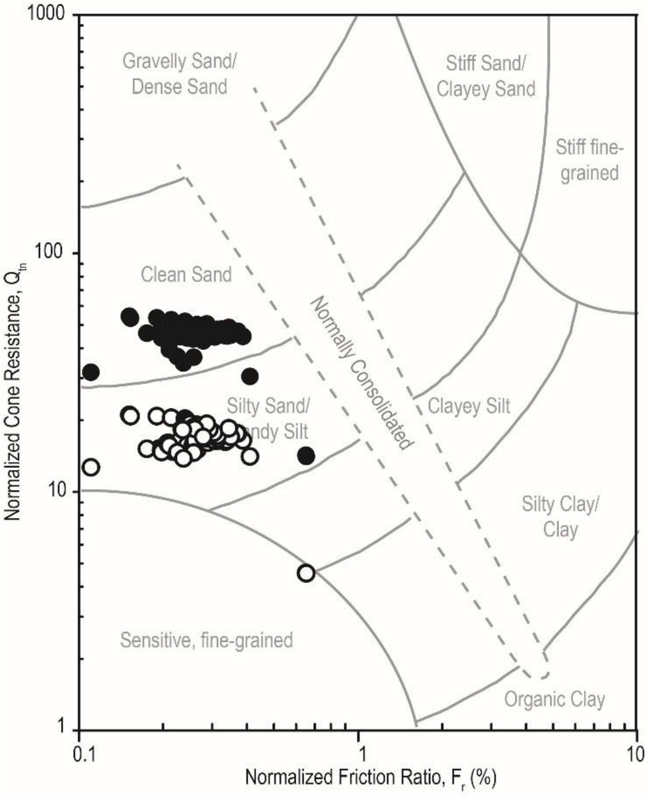

Test 4 Dry Zone (0.0 m ~ 0.68 m)

Pore Pressure Measured From	○ Tensiometer	● Pore Pressure Transducer
In-situ Pore Pressure, u_0	-48 kPa	+2 kPa
Depth of PPD	0.44 m	0.44 m
Gravimetric Water Content	17 %	17 %
Degree of Saturation, S	36.4 %	36.4 %
Pore Pressure Coefficient, X	0.50	0.50
Unit Weight	14 kN/m^3	14 kN/m^3
Stress Exponent, n	0.76	0.59
Soil Behaviour Type Index, I_c	2.35	1.94

Figure 4B- 6: SBT of Test 4 Dry Zone (Q_{tn} - F_r plot)

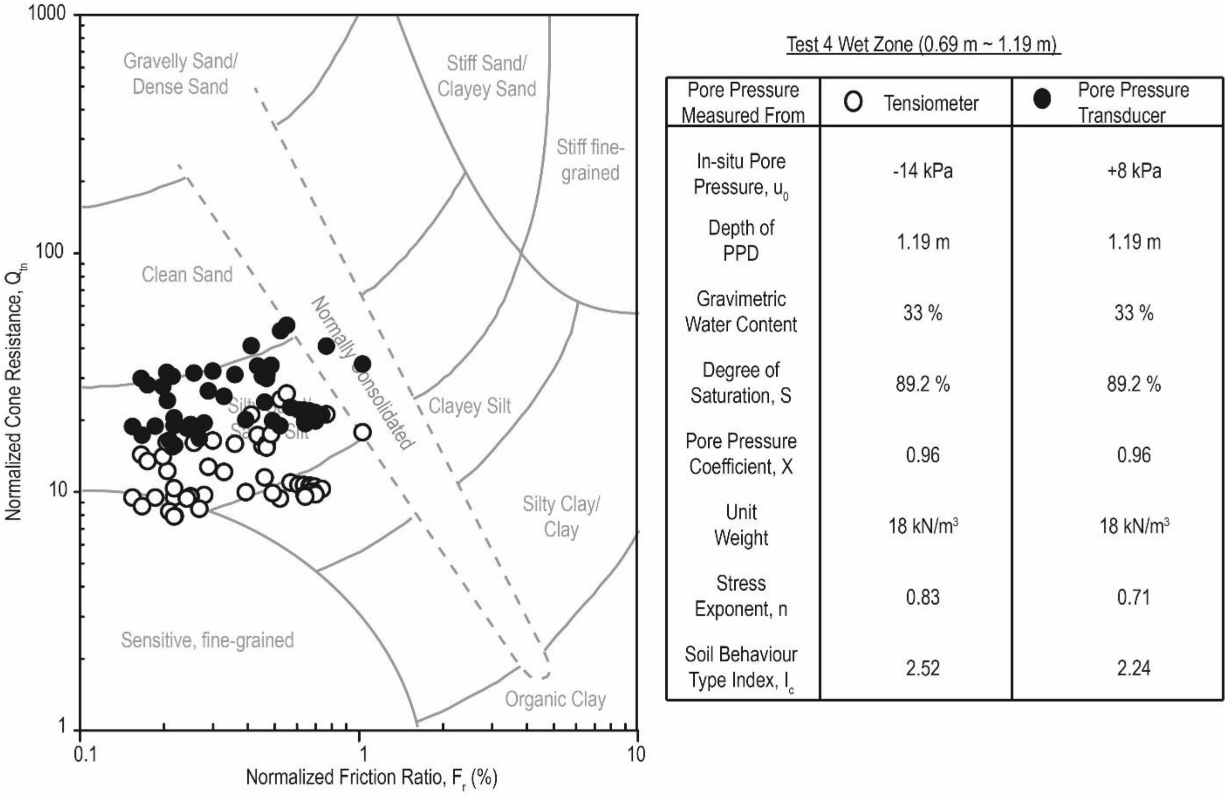

Test 4 Wet Zone (0.69 m ~ 1.19 m)

Pore Pressure Measured From	○ Tensiometer	● Pore Pressure Transducer
In-situ Pore Pressure, u_0	-14 kPa	+8 kPa
Depth of PPD	1.19 m	1.19 m
Gravimetric Water Content	33 %	33 %
Degree of Saturation, S	89.2 %	89.2 %
Pore Pressure Coefficient, X	0.96	0.96
Unit Weight	18 kN/m^3	18 kN/m^3
Stress Exponent, n	0.83	0.71
Soil Behaviour Type Index, I_c	2.52	2.24

Figure 4B- 7: SBT of Test 4 Wet Zone (Q_{tn} - F_r plot)

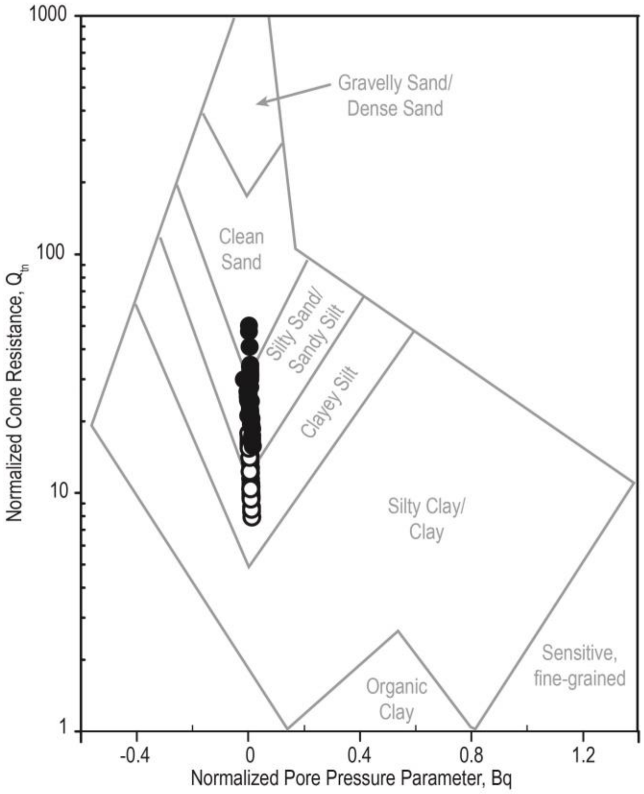

Test 1 (0.0 m ~ 1.24 m)

Pore Pressure Measured From	○ Tensiometer	● Pore Pressure Transducer
In-situ Pore Pressure, u_0	-9.36 kPa	+8 kPa
Excess Pore Pressure, u_2	-6.7 kPa	-4.16 kPa to +8.0 kPa
Depth of PPD	1.24 m	1.24 m
Gravimetric Water Content	35 %	35 %
Degree of Saturation, S	100 %	100 %
Pore Pressure Coefficient, X	1.0	1.0
Unit Weight	19 kN/m^3	19 kN/m^3
Stress Exponent, n	0.85	0.77
Soil Behaviour Type Index, I_c	2.60	2.41

Figure 4B- 8: SBT of Test 1 (Q_{tn} - B_q plot)

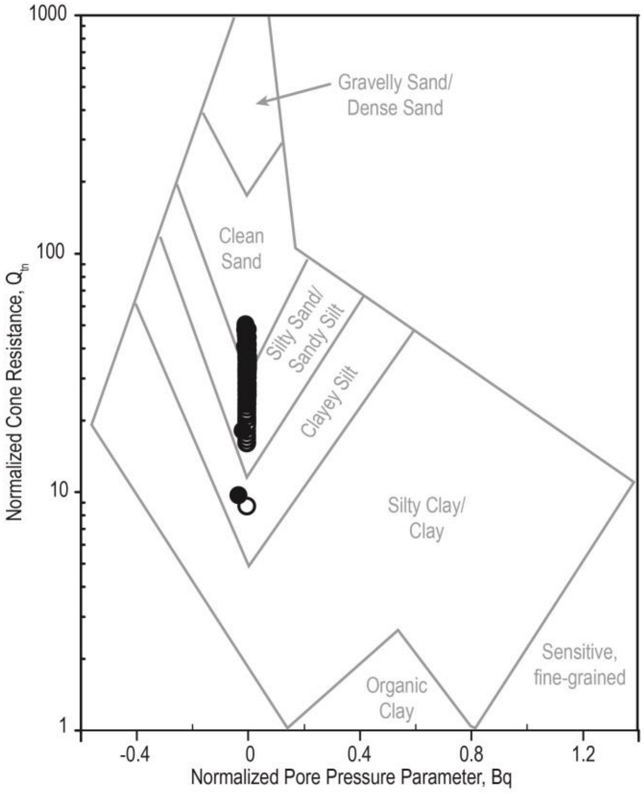

Test 2 Dry Zone (0.0 m ~ 0.80 m)

Pore Pressure Measured From	○ Tensiometer	● Pore Pressure Transducer
In-situ Pore Pressure, u_0	-70.7 kPa	-0.1 kPa
Excess Pore Pressure, u_2	-70.7 kPa	-4.58 kPa to +3.27 kPa
Depth of PPD	0.47 m	0.47 m
Gravimetric Water Content	14.5 %	14.5 %
Degree of Saturation, S	32.3 %	32.3 %
Pore Pressure Coefficient, X	0.1	0.1
Unit Weight	13 kN/m^3	13 kN/m^3
Stress Exponent, n	0.66	0.61
Soil Behaviour Type Index, I_c	2.10	1.99

Figure 4B- 9: SBT of Test 2 Dry Zone (Q_{tn} - B_q plot)

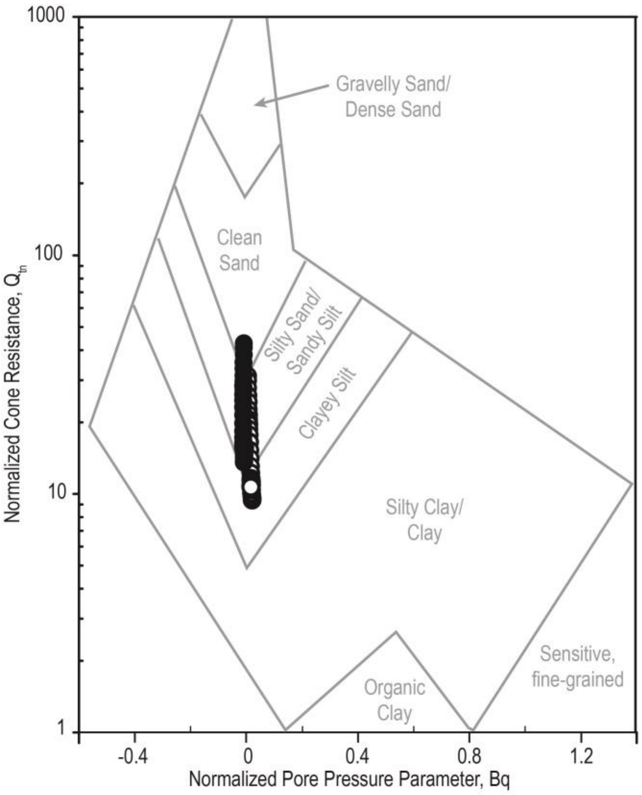

Test 2 Wet Zone (0.81 m ~ 1.26 m)

Pore Pressure Measured From	○ Tensiometer	● Pore Pressure Transducer
In-situ Pore Pressure, u_0	-20.4 kPa	-3.5 kPa
Excess Pore Pressure, u_2	-11.1 kPa	-7.91 kPa to -3.50 kPa
Depth of PPD	1.26 m	1.26 m
Gravimetric Water Content	30 %	30 %
Degree of Saturation, S	89.9 %	89.9 %
Pore Pressure Coefficient, X	0.89	0.89
Unit Weight	18.5 kN/m^3	18.5 kN/m^3
Stress Exponent, n	0.91	0.85
Soil Behaviour Type Index, I_c	2.74	2.61

Figure 4B- 10: SBT of Test 2 Wet Zone (Q_{tn} - B_q plot)

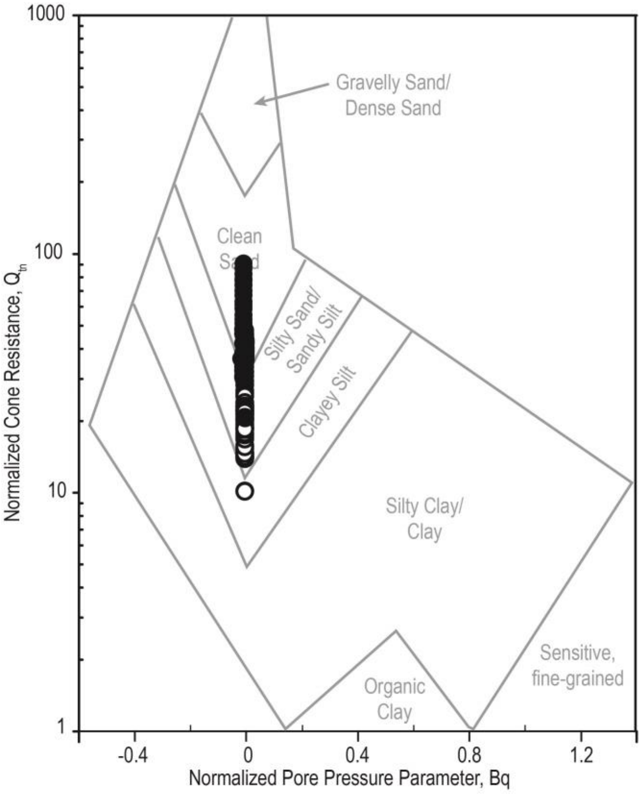

Test 3 Dry Zone (0.0 m ~ 0.8 m)

Pore Pressure Measured From	○ Tensiometer	● Pore Pressure Transducer
In-situ Pore Pressure, u_0	-24.6 kPa	+1.5 kPa
Excess Pore Pressure, u_2	-24.6 kPa	-5.10 kPa to +2.75 kPa
Depth of PPD	0.52 m	0.52 m
Gravimetric Water Content	24 %	24 %
Degree of Saturation, S	75 %	75 %
Pore Pressure Coefficient, X	0.81	0.81
Unit Weight	18 kN/m^3	18 kN/m^3
Stress Exponent, n	0.78	0.66
Soil Behaviour Type Index, I_c	2.41	2.12

Figure 4B- 11: SBT of Test 3 Dry Zone (Q_{tn} - B_q plot)

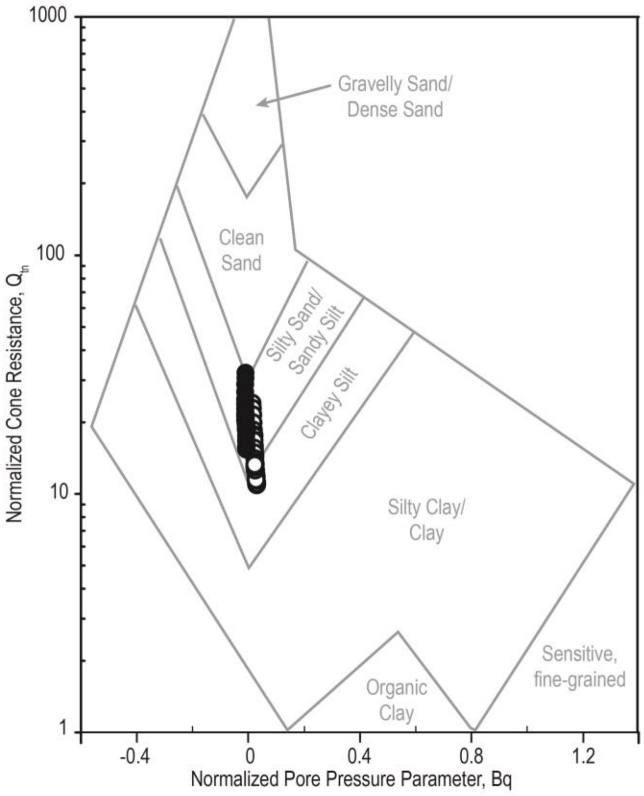

Test 3 Wet Zone (0.81 m ~ 1.23 m)

Pore Pressure Measured From	○ Tensiometer	● Pore Pressure Transducer
In-situ Pore Pressure, u_0	-16 kPa	-0.5 kPa
Excess Pore Pressure, u_2	-1.0 kPa	-4.62 kPa to -0.50 kPa
Depth of PPD	1.23 m	1.23 m
Gravimetric Water Content	27 %	27 %
Degree of Saturation, S	85 %	85 %
Pore Pressure Coefficient, X	0.92	0.92
Unit Weight	18.5 kN/m^3	18.5 kN/m^3
Stress Exponent, n	0.89	0.84
Soil Behaviour Type Index, I_c	2.70	2.58

Figure 4B- 12: SBT of Test 3 Wet Zone (Q_{tn} - B_q plot)

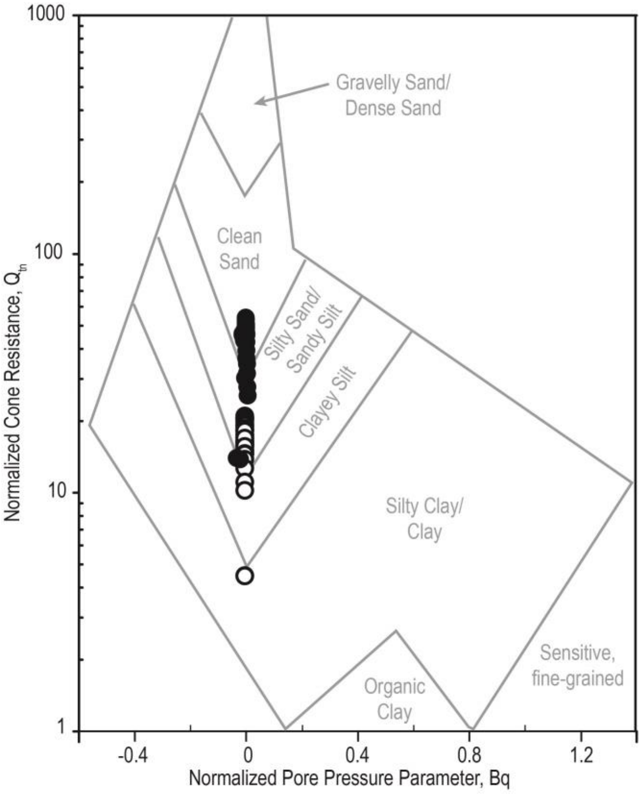

Test 4 Dry Zone (0.0 m ~ 0.68 m)

Pore Pressure Measured From	○ Tensiometer	● Pore Pressure Transducer
In-situ Pore Pressure, u_0	-48.1 kPa	+2.0 kPa
Excess Pore Pressure, u_2	-48.1 kPa	-2.32 kPa to +4.35 kPa
Depth of PPD	0.44 m	0.44 m
Gravimetric Water Content	17 %	17 %
Degree of Saturation, S	36.4 %	36.4 %
Pore Pressure Coefficient, X	0.50	0.50
Unit Weight	14 kN/m^3	14 kN/m^3
Stress Exponent, n	0.76	0.59
Soil Behaviour Type Index, I_c	2.35	1.94

Figure 4B- 13: SBT of Test 4 Dry Zone (Q_{tn} - B_q plot)

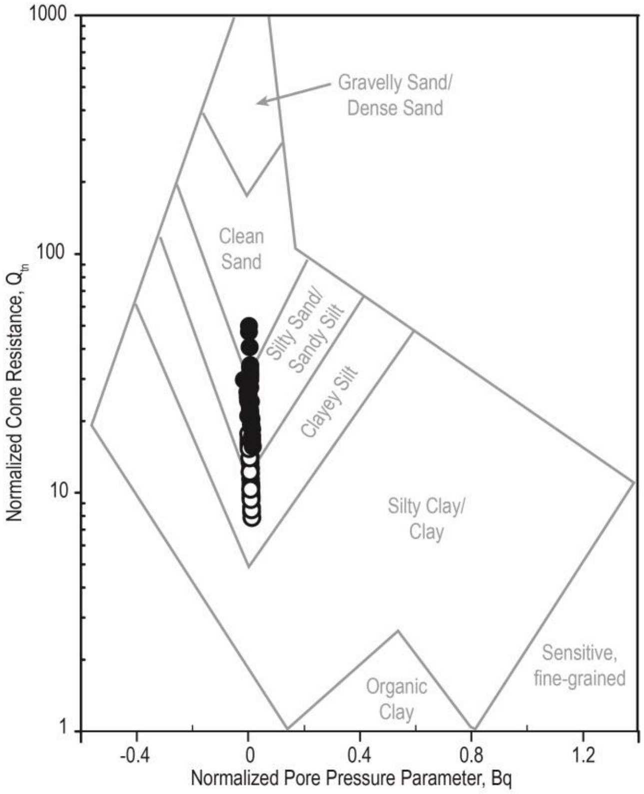

Test 4 Wet Zone (0.69 m ~ 1.19 m)

Pore Pressure Measured From	○ Tensiometer	● Pore Pressure Transducer
In-situ Pore Pressure, u_0	-14.1 kPa	+8 kPa
Excess Pore Pressure, u_2	-9.3 kPa	+3.1 kPa to +8.0 kPa
Depth of PPD	1.19 m	1.19 m
Gravimetric Water Content	33 %	33 %
Degree of Saturation, S	89.2 %	89.2 %
Pore Pressure Coefficient, X	0.96	0.96
Unit Weight	18 kN/m^3	18 kN/m^3
Stress Exponent, n	0.83	0.71
Soil Behaviour Type Index, I_c	2.52	2.24

Figure 4B- 14: SBT of Test 4 Wet Zone (Q_{tn} - B_q plot)

Appendix 4C - PPD curves

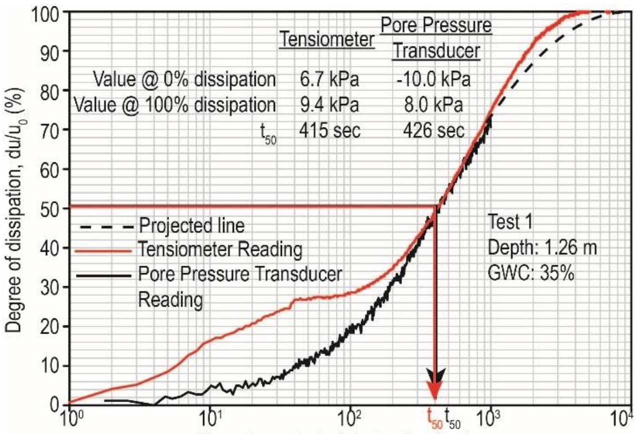

NOTE:
Tensiometer Reading = Matric Suction (kPa)
Pore Pressure Transducer Reading = Pore-water Pressure (kPa)

Figure 4C- 1: PPD curves of Test 1

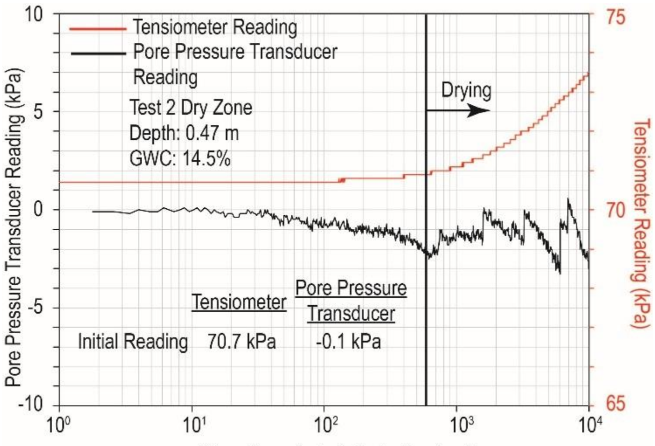

NOTE:
Tensiometer Reading = Matric Suction (kPa)
Pore Pressure Transducer Reading = Pore-water Pressure (kPa)

Figure 4C- 2: PPD curves of Test 2 (Dry Zone)

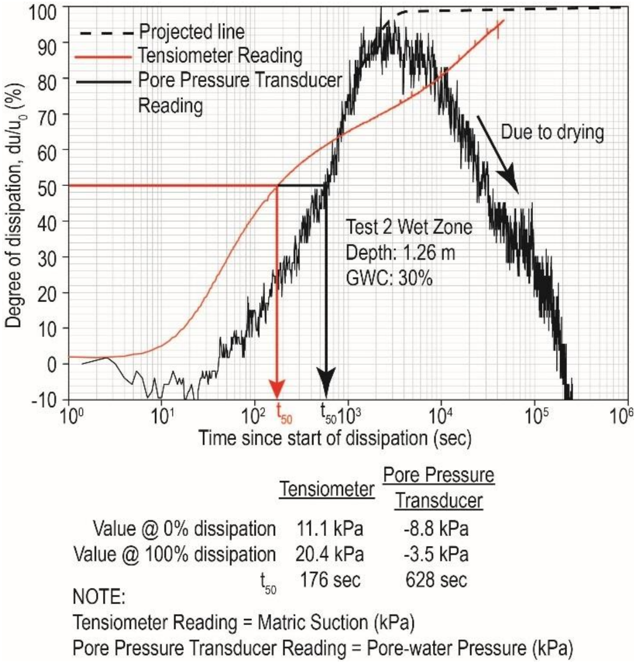

	Tensiometer	Pore Pressure Transducer
Value @ 0% dissipation	11.1 kPa	-8.8 kPa
Value @ 100% dissipation	20.4 kPa	-3.5 kPa
t_{50}	176 sec	628 sec

NOTE:
Tensiometer Reading = Matric Suction (kPa)
Pore Pressure Transducer Reading = Pore-water Pressure (kPa)

Figure 4C- 3: PPD curves of Test 2 (Wet Zone)

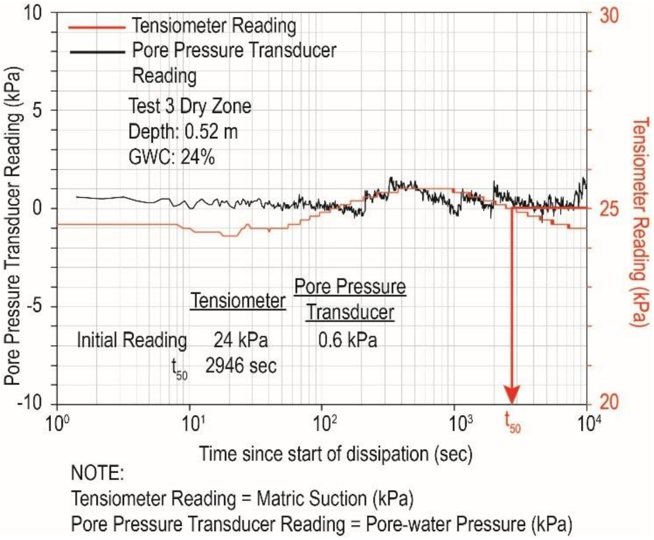

	Tensiometer	Pore Pressure Transducer
Initial Reading	24 kPa	0.6 kPa
t_{50}	2946 sec	

NOTE:
Tensiometer Reading = Matric Suction (kPa)
Pore Pressure Transducer Reading = Pore-water Pressure (kPa)

Figure 4C- 4: PPD curves of Test 3 (Dry Zone)

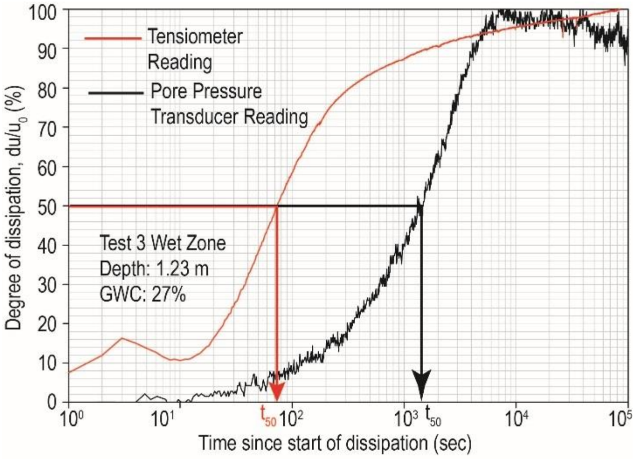

	Tensiometer	Pore Pressure Transducer
Value @ 0% dissipation	-1.0 kPa	-14.4 kPa
Value @ 100% dissipation	16.0 kPa	-0.5 kPa
t_{50}	73 sec	1305 sec

NOTE:
Tensiometer Reading = Matric Suction (kPa)
Pore Pressure Transducer Reading = Pore-water Pressure (kPa)

Figure 4C- 5: PPD curves of Test 3 (Wet Zone)

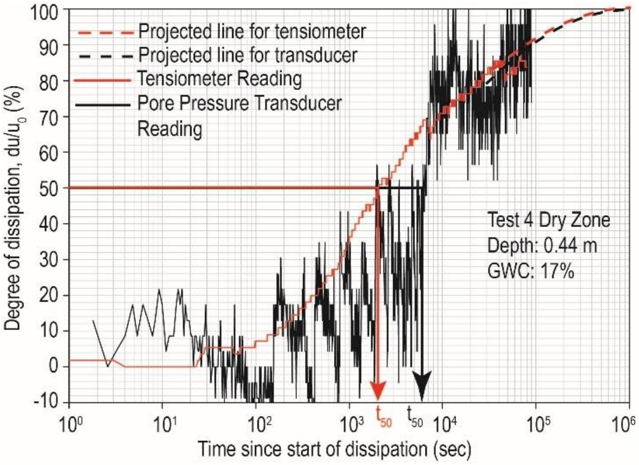

	Tensiometer	Pore Pressure Transducer
Value @ 0% dissipation	48.0 kPa	0.2 kPa
Value @ 100% dissipation	53.5 kPa	2.5 kPa
t_{50}	2088 sec	6654 sec

NOTE:
Tensiometer Reading = Matric Suction (kPa)
Pore Pressure Transducer Reading = Pore-water Pressure (kPa)

Figure 4C- 6: PPD curves of Test 4 (Dry Zone)

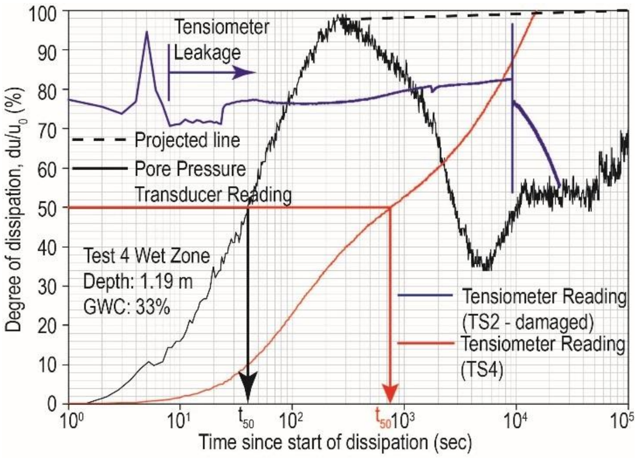

	Tensiometer	Pore Pressure Transducer
Value @ 0% dissipation	9.3 kPa	8.0 kPa
Value @ 100% dissipation	14.1 kPa	-3.2 kPa
t_{50}	752 sec	40 sec

NOTE:
Tensiometer Reading = Matric Suction (kPa)
Pore Pressure Transducer Reading = Pore-water Pressure (kPa)

Figure 4C- 7: PPD curves of Test 4 (Wet Zone)

Appendix 4D - Tensiometer Readings

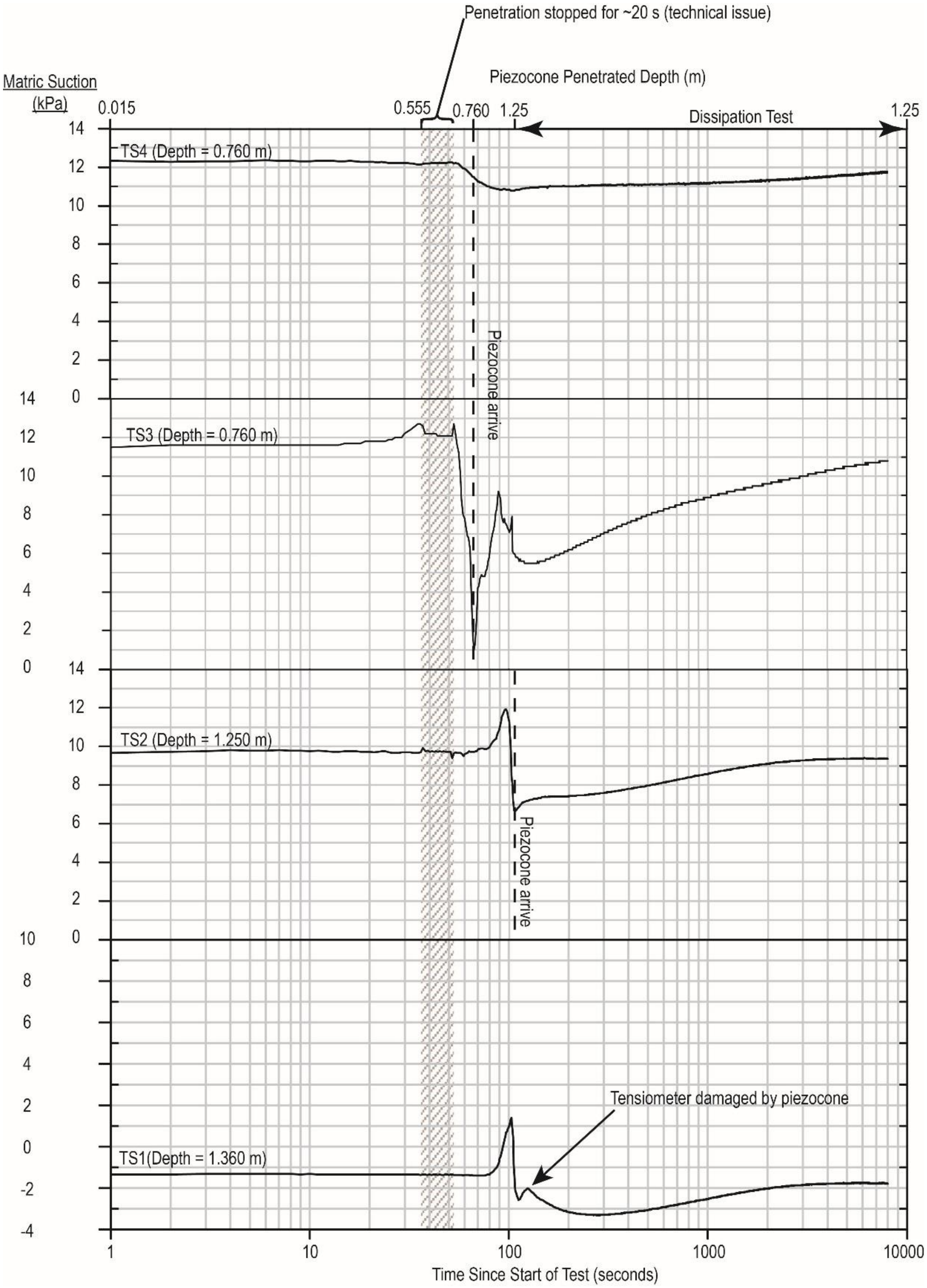

Figure 4D- 1: Tensiometer Readings of Test 1

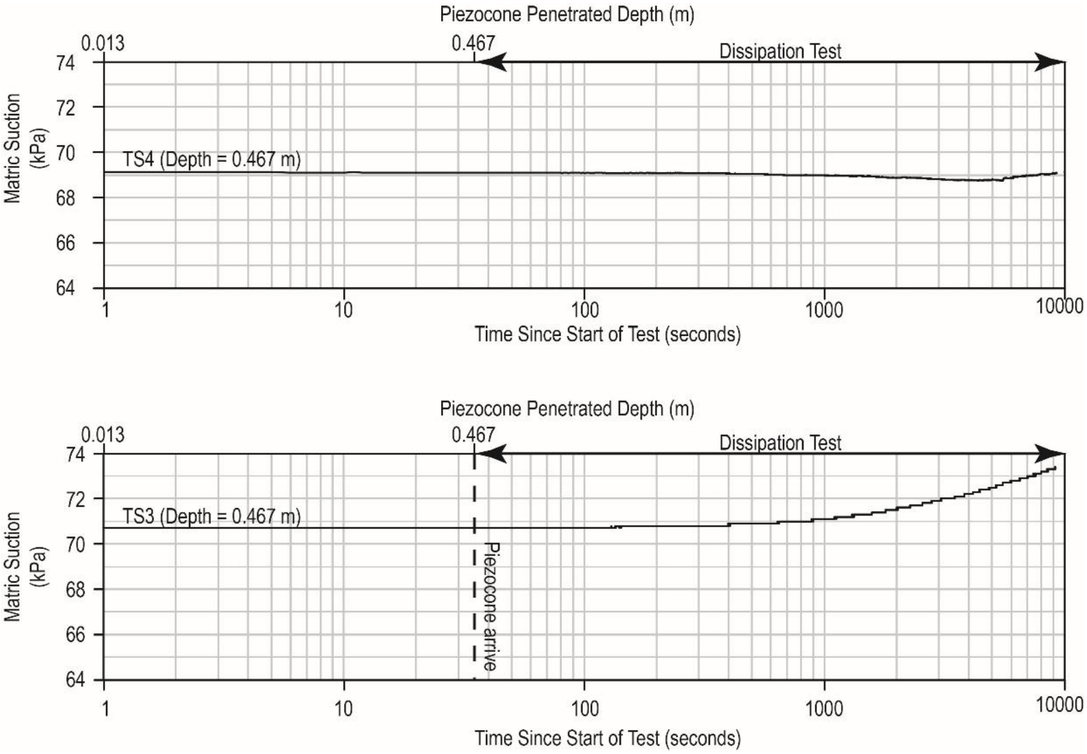

Figure 4D- 2: Tensiometer Readings of Test 2 (Dry Zone)

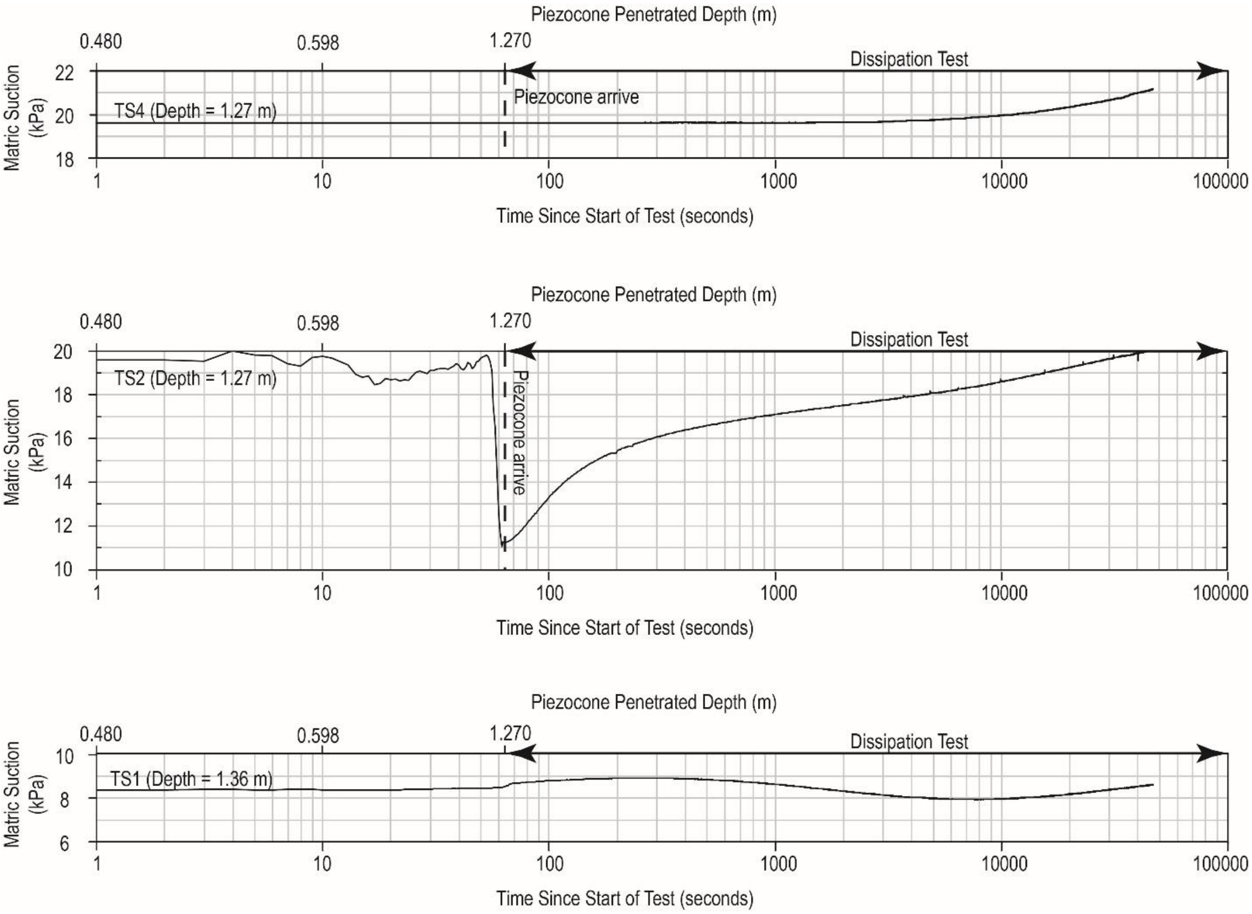

Figure 4D- 3: Tensiometer Readings of Test 2 (Wet Zone)

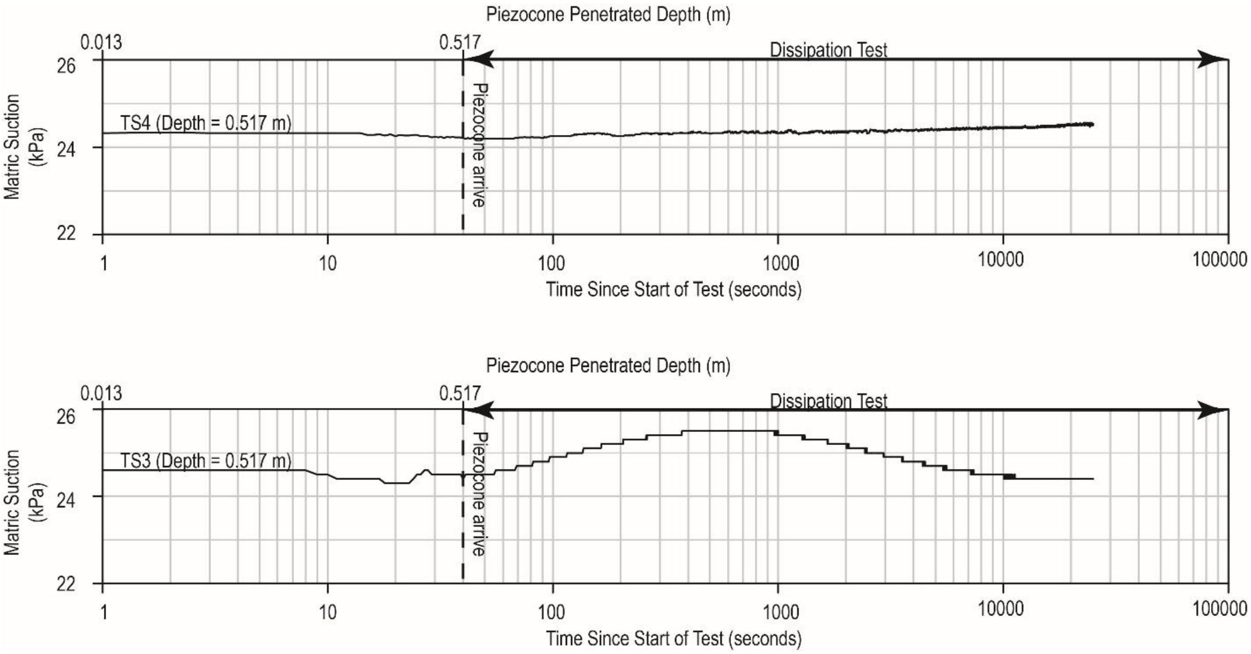

Figure 4D- 4: Tensiometer Readings of Test 3 (Dry Zone)

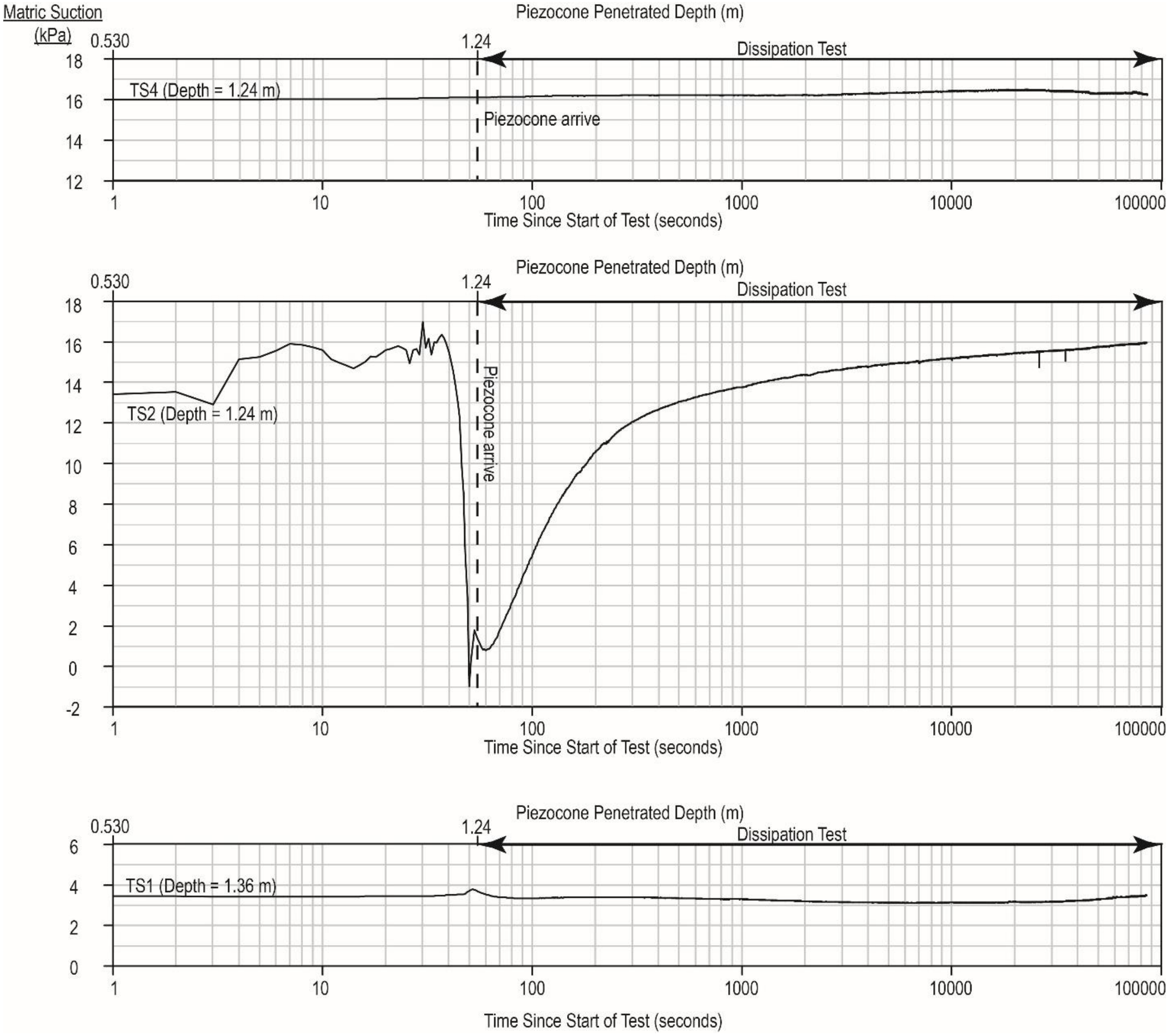

Figure 4D- 5: Tensiometer Readings of Test 3 (Wet Zone)

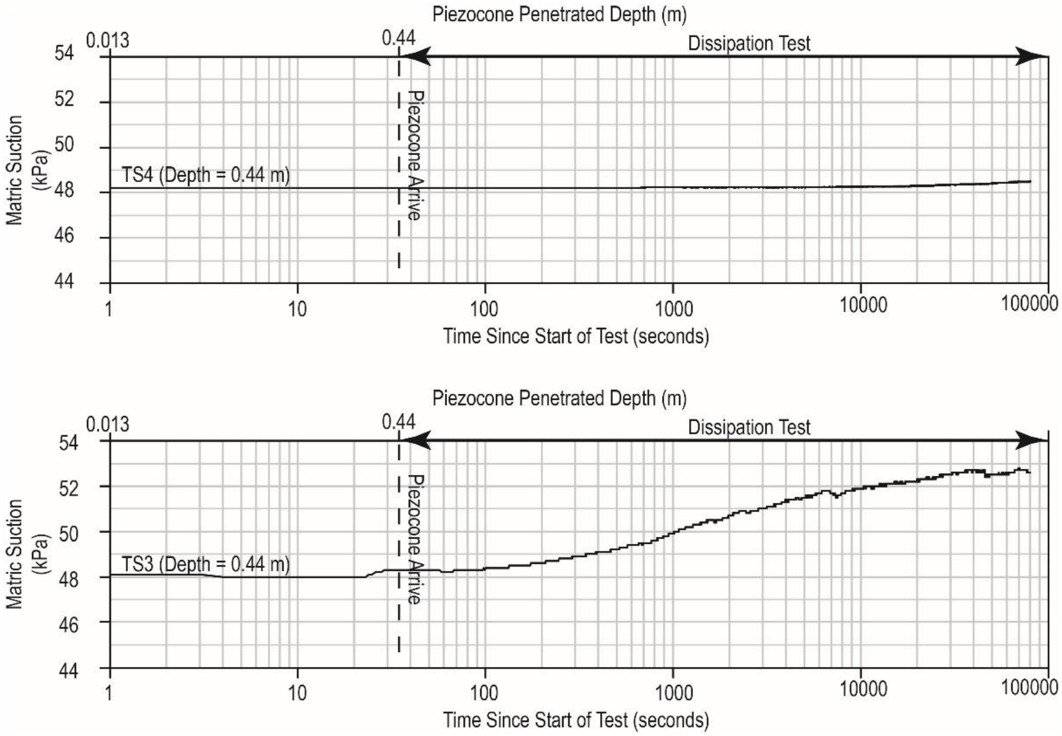

Figure 4D- 6: Tensiometer Readings of Test 4 (Dry Zone)

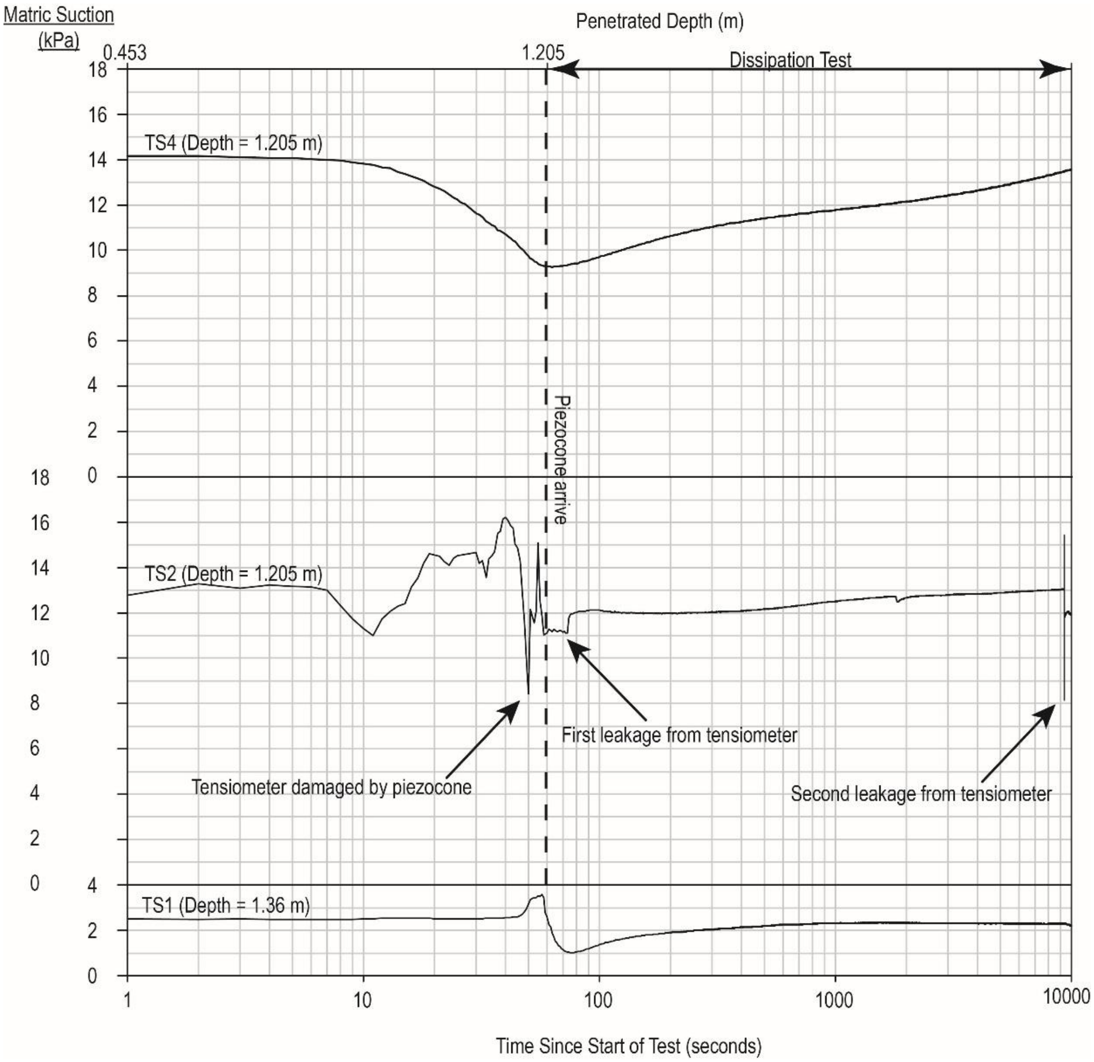

Figure 4D- 7: Tensiometer Readings of Test 4 (Wet Zone)

Chapter 5. Closing Remarks

5.1 Conclusions

Three major studies constituted this research: The first part is devoted to developing an alternate method for shrinkage limit tests; and to completing our understanding to all the parameters in the shrinkage curve model developed by Fredlund et al. (2002). Results of this study are presented in Chapter 2. The second part is devoted to characterizing the physical properties of the silt material (red silt) which is the specimen to be tested in the third part of the research. Characterized properties of the red silt are presented in Chapter 3. In the third part of the study, four cone penetration tests (CPT) were conducted in a chamber filled with unsaturated red silt which was also instrumented with rapid-response tensiometers. Results of the chamber tests were used to assess the performance of a piezocone in unsaturated soils and to evaluate if measurements of pore pressures in unsaturated soils could be aided with the use of tensiometers. The results and interpretations of this study are presented in Chapter 4.

In Chapter 2, a 3D scanner was used to help characterize the shrinkage properties of a given soil. A 3D scanner utilizes both computer imagery and LiDAR (Light Detection and Ranging) technology to digitize a real-life object into a set of 3D coordinates, which is also known as a point cloud. The accuracy and consistency of the results produced by a 3D scanner was tested by repeatedly scanning a metal puck of known volume. Out of the 15 scans, the percent difference between the results fall within 2% of each other and an average 9% error from the actual volume. Thus, it can be concluded that the 3D scanner produces consistent but inaccurate measurements. However, the accuracy of the 3D scanner can be significantly enhanced with suitable calibrations. A procedure on using the 3D scanner to conduct a shrinkage limit test was also proposed.

Following this procedure, shrinkage data of nine soils were obtained. In addition, shrinkage data of eighteen soils of various plasticity were also obtained from literatures. Using a linear regression analysis, an empirical correlation was developed to reasonably relate parameter c_{sh} from the shrinkage model developed by Fredlund et al. (2002) to the ratio of the plastic and liquid limits.

In Chapter 3, a series of lab tests was conducted to fully characterize the physical properties of the silt specimen (red silt). Grain size distribution indicates that the silt material consists around 80% silt to clay-sized particles by mass with the rest being very fine sand. Atterberg limit tests showed that the silt material is classified as a medium- to low-plasticity silt, or “MI” with reference to USCS. Soil-Water Characteristic Curve (SWCC) tests were conducted using a “U of S Pressure Plate Cell” also known as a Tempe cell. The air-entry value, residual suction and residual degree of saturation were obtained and equal to 9.5 kPa, 75 kPa and 20% respectively. Consolidated undrained triaxial tests were conducted on the red silt to obtain its shear strength profile under saturated and unsaturated conditions. Sixteen triaxial tests (nine saturated samples, and seven unsaturated samples) resulted in an effective cohesion (c'); effective friction angle (f'); and unsaturated friction angle (f^b) of 0 kPa, 29.9 degrees and 24.2 degrees respectively.

In Chapter 4, the methodology and the results of the calibrated chamber tests are presented. The calibrated chamber tests were conducted by advancing a piezocone at a fixed rate (20 millimeters/min ± 5 millimeters/min) into a chamber filled with an unsaturated silt of specified gravimetric water content. In each test, the chamber was filled with two layers of unsaturated material at two different water contents. In each case, the dryer soil overlaid the wetter one. Two rapid response tensiometers were installed within each layer of deposit for a total of 4 per test.

During and after CPT advancement, cone resistance, sleeve friction, pore water-pressure and matric suction were monitored and recorded. Upon reaching the target depth of each layer, a Pore Pressure Dissipation (PPD) test was conducted. The chamber test was repeated for four times at a total of seven different water contents. Results confirmed that the pore pressure transducer equipped on the piezocone was incapable of accurately measuring the negative pore-water pressure of the soil. The negative pore-water pressures around the CPT in the unsaturated soils were measured with tensiometers. Empirical correlations for Soil Behaviour Type (SBT), shear strength and hydraulic conductivity were used to analyze its applicability in unsaturated soils. It was found that that the empirical relationship for SBT is still applicable if the effective stress is corrected for the associated negative pore-water pressure; a typical value for cone factor (N_{kt}) (around 10 to 15) is still applicable to estimate the shear strength of the unsaturated soil; empirical correlations to estimate hydraulic conductivity and coefficient of consolidation from PPD results are also applicable to unsaturated silt as long as the in-situ suction is lower than the air-entry value.

5.2 Research contribution

The two major studies in this research contributes to the literature in unsaturated soil mechanics and in-situ testing methods.

In the field of unsaturated soil mechanics, since Fredlund & Houston (2013) pointed out the need to couple a SWCC with a shrinkage curve to account for soil shrinkage, shrinkage limit tests became a prerequisite to most unsaturated soil tests. The traditional method of conducting shrinkage limit tests requires the use of mercury and was therefore abandoned by ASTM in 2008 due to health and safety concerns. The proposed procedure to conducting shrinkage limit tests using a 3D scanner (Chapter 2) could potentially provide an alternative approach to obtaining a shrinkage curve in an accurate and user-friendly manner. The parameter c_{sh} of the shrinkage model developed by Fredlund et al. (2002) was also quantified in this research with respect to a soils given plasticity. The empirical equation, which relates c_{sh} to the Atterberg limits of a soil, can further streamline the process to obtaining a shrinkage curve and could potentially replace the entire procedure of measuring the complete shrinkage curve with simply measuring the Atterberg limits and the shrinkage limit of a soil.

In the literature of in-situ testing methods, unsaturated soils have been a limitation to cone penetration testing (CPT) because of two major reasons: Firstly, the porous stone of a piezocone tends to desaturate in unsaturated soils due to soil suction. Pore-water pressure measurements made by a desaturated porous stone are inaccurate (Campanella & Robertson, 1988). Secondly, no research has been conducted to document the accuracy of existing empirical equations for unsaturated soils.

For low- to medium-budgeted projects, CPT could be the major site investigation tool used to help geotechnical engineers characterize a construction site. If a major portion of the subsurface of the site is unsaturated (above water-table), interpretation based on CPT soundings could be far from the actual condition. Foundation designs based on CPT results that are uncorrected for unsaturated soils are often overly-conservative.

As presented in this research, the incorporation of tensiometers significantly enhances the accuracy of CPT interpretation in terms of Soil Behavior Type (SBT), hydraulic conductivity, in-situ pore pressures and effective stress, etc. Correction factors for existing empirical correlations are also proposed to account for the soil suction in unsaturated soils. With this research, the application of CPT could potentially be extended to unsaturated soils and opened the doorway to site investigations within the vadose zone.

5.3 Limitations of research

For the sake of practicality, CPTs in laboratory setting are usually conducted in a chamber of limited size (Yu & Mitchell, 1998). The limitation of chamber size is often the major cause for the different results obtained between field and lab condition as it imposes a different boundary effect to the CPT test. Parkin & Lunne (1982) reported that the boundary effect is negligible if the ratio of chamber width to the diameter of the cone penetrometer (R_d) is 50 times or higher for dense sand (relative density = 90%); whereas, the boundary effect can be neglected if R_d is larger than 20 for loose sand (relative density = 30%). In the chamber tests of this research, the diameter of the cone is ~38 mm and the width of the chamber is ~910 mm, hence, the resulting R_d is ~24. If the result of Parkin & Lunne (1982) are applicable to this scenario (unsaturated soils), then the obtained cone resistance values are higher than that obtained in the field, though side wall treatments designed to reduce friction may help to reduce this discrepancy.

There was no conclusion arrived in this research to quantify the boundary effect, as not only was there a lack of literature illustrating the problem under similar scenarios (cavity expansion in unsaturated soils); there was no intention to produce new empirical correlations based on the experimental results, other than suggesting correction factor for unsaturated soils. While all the dimensions of test apparatuses, densities of the test subject (the red silt) during the experiments were documented, any future referencing of this thesis should note that no correction factor has been applied during the analysis to account for the boundary effect. Therefore, cautions should be exercised when referencing the results of this thesis. Seemingly, numerical modelling and field testing using a tensiometer prototype module are required to further quantify the effect of the chamber walls in this research.

5.4 Possible extension to the research

In the first part of the research (quantification of the shrinkage curve parameter), an empirical relationship between parameter c_{sh} and Atterberg's limits was developed based on shrinkage limit tests of the twenty-seven soils. The proposed empirical equation effectively streamlines the process associated with obtaining a shrinkage limit test. Shrinkage limit tests usually require 24 to 48 hours of repetitive scanning and weighing. With the proposed empirical equation, the repetitive scanning and weighing cycles might be replaced by using the Atterberg limits and a single 3D scanning to obtain the minimum void ratio of a dried soil sample. Once the specific gravity of the soil is obtained, parameters a_{sh}, b_{sh}, and c_{sh} (and, thus, the entire shrinkage curve) can be estimated. This procedure considerably reduces the time required to obtain a shrinkage curve. Should a shrinkage limit test ought to be conducted inevitably, the method of using a 3D scanner outlined in the section can be followed to produce a shrinkage curve. With the rapid technological advancement of remote sensing in terms of hard-wares and software algorithms, shrinkage limit tests could potentially be completed in a quicker and more accurate manner.

In the second half of the research, CPT tests were conducted within a chamber of unsaturated silt with the use of tensiometers to monitor changes of suction during piezocone penetration. The results confirmed that the pore pressure measurements made by the piezocone in unsaturated soils are flawed and tensiometers or some other matric suction device ought to be used. In the chamber tests, each of the tensiometers were installed at fixed depths to measure the matric suctions with approach and passage of the CPT probe. Therefore, to obtain suction values continuously with depth, tensiometers are needed in larger quantities or built as an on-board module. Continuous logging of matric suction with depth can be made possible by equipping piezocones with tensiometer tips. Further research is required to assemble a device of such.

Solutions to the cavity expansion problem have been of great value to developing empirical correlations for CPT in saturated soils (Vesić, 1972; Baligh & Levadoux, 1986; Cao et al., 2001; Yu, 2000). Solutions for cavity expansion of unsaturated soils have been proposed by Russell & Khalili (2003), but has yet been used to develop theoretical correlations in CPT. Similarly, creation of numerical models for in-situ testing in unsaturated soils are rare. Developments in these areas could not only benefits the application of CPTs in unsaturated soils but also other in-situ testing methods in unsaturated medium.

References

Baligh, M., & Levadoux, J.-N. (1986). Consolidation after undrained piezocone penetration. II: interpreatation. *Journal of Geotechnical Engineering, 112*(7), 727-745.

Campanella, R., & Robertson, P. (1988). Current status of the piezocone test. *In Proc. 1st Int. Symp. on Penetration Testing, 1,* 93-116.

Cao, L., Teh, C., & Chang, M. (2001). Undrained cavity expansion in modified Cam clay. *Geotechnique, 51*(4), 323-350.

Costa, S., Kodikara, J., & Thusyanthan, N. (2008). Modelling of desiccation crack development in clay soils. *Proc. 12th International Conference of IACMAG,* (pp. 1099-1107). Goa, India.

Daniel, D., & Wu, Y. (1993). Compacted Clay Liners and Covers for Arid Sites. *Journal of Geotechnical Engineering, 2*(119), 223-237.

Fredlund, D., & Houston, S. (2013). Interpretation of soil-water characteristic curves when volume change occurs as soil suction is changed. *Proceedings, 1st Pan-American conference on unsaturated soils., 1,* pp. 15-31. Cartagena de Indias, Columbia.

Fredlund, M.D.; Wilson, G.W.; Fredlund, D.G. (2002). Representation and estimation of the shrinkage curve. *Thrid International Conference on Unsaturated Soils*, 145-149.

Ghafoori, E., & Motavalli, M. (2011). Analytical calculation of stress intensity factor of cracked steel I-beams with experimental analysis and 3D digital image correlation measurements. *Engineering Fracture Mechanics, 78*(18), 3226-3242.

Hild, F., & Roux, S. (2006). Measuring stress intensity factors with a camera: Integrated digital image correlation (I-DIC). *Comptes Rendus Mecanique*, *334*(1), 8-12.

Park, J., Chang, K., & Kim, C. (2001). Numerical simulations of the moisture movement in unsaturated bentonite under a thermal gradient. *Journal of Korean Nuclear Society, 1*(33), 62-72.

Russell, A., & Khalili, N. (2003). On the problem of cavity expansion in unsaturated soils. *Computational mechanics, 37*(4), 311-330.

Vesić, A. (1972). Expansion of cavities in infinite soil mass. *Journal of the Soil Mechanics and Foundations Division*, *98*, 265-290.

Yu, H., & Mitchell, J. (1998). Analysis of cone resistance: review of methods. *Journal of geotechnical and geoenvironmental engineering, 124*(2), 140-149.

Yu, H.-s. (2000). *Cavity Expansion Methods in Geomechanics.* Springer Science and Business Media.

Zhou, Y., & Rowe, R. (2003). Development of a technique for modelling clay liner desiccation. *Int. J. Numer. Anal. Math. Geomech.*(27), 473-493.